Diplomarbeit

Evaluation and improvement of the performance of an adaptive optics scanning laser ophthalmoscope

Ausgeführt am
Institut für Angewandte Physik
der Technischen Universität Wien

unter der Anleitung von
Ao.Univ.Prof. Dipl.-Ing. Dr.techn. Martin Gröschl

in Zusammenarbeit mit
Assoc. Prof. Priv.-Doz. Dipl.-Ing. Dr. Michael Pircher

Zentrum für Medizinische Physik und Biomedizinische Technik
der Medizinischen Universität Wien

durch
Ana Rita Simões Gonçalves de Carvalho BSc
Gasgasse 2, 5050//B
1150 Wien

September 2014

Abstract

Adaptive optics in visual science is of enormous research and clinical interest. The combination of adaptive optics with scanning laser ophthalmoscopy (AO-SLO) provides high resolution real-time images of the human retina, enabling an in vivo visualization of retinal cells such as photoreceptors and blood cells. Thereby this new technology enables completely new opportunities for an improved diagnosis and therapy control.

The underlying goal of this thesis is the characterization and optimization of a confocal AO-SLO which at the start of the thesis could not provide images with sufficient quality. AO-SLO systems occupy in general a large space and provide only images with a very small field of view. One key characteristic of the used AO-SLO system is a compact foot-print and an implemented line scanning SLO channel that provides overview images of the retina.

A number of modifications and new features were implemented within this thesis that included not only the experimental setup but also software development in order to improve adaptive optics control. In addition software for off-line processing of the AO-SLO images was developed and implemented. After implementation of these modifications the AO-SLO system was used to image healthy volunteers. Images of the cone and rod mosaic as well as of retinal vasculature are presented. Finally, the feasibility of using a multimode fiber for light collection to enhance image contrast was tested.

Kurzfassung

Die adaptive Optik (AO) am Auge ist von bedeutendem wissenschaftlichem und klinischem Interesse. Die Kombination von adaptiver Optik mit einem Rasterabtast Laser Ophthalmoskop (engl. Scanning Laser Ophthalmoscope (SLO)) ermöglicht die Aufnahme von hochaufgelösten Bildern der menschlichen Netzhaut in vivo und erreicht dabei die Visualisierung von einzelnen Zellen wie etwa Lichtrezeptoren oder Blutzellen. Diese Technologie ebnet den Weg für komplett neue Ansätze in der Diagnostik und Therapieverlaufskontrolle.

Das Ziel dieser Diplomarbeit ist die Charakterisierung und Verbesserung eines konfokalen AO-SLOs welches zu Beginn der Arbeit keine Bilder mit zufriedenstellender Qualität liefern konnte. Im Allgemeinen benötigen die AO-SLOs viel Platz und können nur Bilder mit einem kleinen Gesichtsfeld aufnehmen. Das in dieser Arbeit verwendete AO-SLO System zeichnet sich durch ein kompaktes Design aus und besitzt zusätzlich einen Linienraster SLO Kanal welcher Übersichtsbilder der Netzhaut liefert.

Durch diese vorliegende Arbeit wurde eine Vielzahl von Modifikationen am AO-SLO durchgeführt. Diese beinhalteten sowohl experimentelle Änderungen als auch Software Entwicklungen für die Verbesserung der AO-Kontrolle. Zusätzlich wurde Software für die Datenerfassung und Datenauswertung entwickelt. Nach der Implementierung dieser Modifikationen wurde das Gerät verwendet um gesunde Probanden zu untersuchen. AO-SLO Bilder vom Zapfen- und Stäbchenmosaik als auch von Kapillaren der Netzhaut werden präsentiert. Im letzten Teil wurde die Möglichkeit untersucht, den Bildkontrast mit Hilfe einer Multimoden Faser in der Detektionseinheit zu verbessern.

Acknowledgements

First and foremost, I would like to express my heartfelt gratitude to my advisor Professor Michael Pircher for his immense support of my Master Project, for his patience and encouragement during the last 8 months. His immense knowledge and passion for research have motivated and helped me throughout the research and writing of this thesis. I could not have been more lucky regarding my mentor and advisor.

I would also like to express my gratitude to all Professors who have supported me. From Professor Patrícia Figueiredo, who made it possible for me to pursue my studies in Vienna, to Professor Martin Gröschl who introduced me to the research team at the Medical University, and to Professor João Mendanha Dias, who was always available for me and who was interested in my work.

I also wish to express thanks to all my family who, despite the physical distance, have made me feel supported all the way through and have stood behind me in all the moments of skinned knees and shaken confidence.

Last but not least, thanks to Guilherme, who reminded me that there is life outside the lab and never failed to call when my studies overwhelmed me. He gave me the ground I could stand on whenever the path ahead seemed dim.

This work was supported by the Austrian Science Fund (FWF project P22329-N20).

Contents

List of Tables

List of Figures

List of Abbreviations

ACF	Autocorrelation function
AMD	Age-related macular degeneration
AO	Adaptive optics
AO-cSLO	Adaptive optics confocal scanning laser ophthalmoscope
APD	Avalanche photodiode
CCD	Charged-coupled device
COG	Center of gravity
CRB	Corneal reflections blocker
cSLO	confocal Scanning laser ophthalmoscope
DiM	Dichroic mirror
DIT	Data integration time
DM	Deformable mirror
DR	Diabetic retinopathy
EC	Entrance collimator
EL	Eye lens
FOV	Field of view
FPGA	Field-programmable gate array
FPS	Frames per second
FWC	Full well capacity
FWHM	Full width at half maximum
GS	Galvo scanner
LSLO	Line-scanning laser ophthalmoscope
LS	Light source
M	Mirror
MMF	Multimode fiber
NA	Numerical aperture
NND	Next neighbour distance
NPBS	Non polarizing beam splitter

PBS	Polarizing beam splitter
PC	Pinhole detection configuration
PSF	Point spread function
PQS	Peak quantum efficiency
QWP	Quarter wave plate
RMS	Root mean square
RNFL	Retina nerve fiber layer
ROI	Region of interest
RPE	Retinal pigment epithelium
SH	Shack-Hartmann
SLO	Scanning laser ophthalmoscope
SMF	Single-mode fiber
SNR	Signal-to-noise ratio

Chapter 1

Introduction

1.1 Context and Motivation

"Vision is our most dominant sense, from which we derive most of our information about the world" [1].

Vision plays a fundamental role in human perception, cognition and learning tasks. It reveals itself as a complex and fascinating process, triggered by the light that reaches the retina cells in the eye.

In 1851 the ophthalmoscope was invented by Helmholtz, which allowed for the first time the investigation of the posterior segment[1] *in vivo* [3].

Many ocular pathologies arrive from retina related diseases, such as retinal dystrophies which lead to retina degeneration and eventually partial or total blindness. An impressive progress in the study of these diseases has been achieved since 1857, when shortly after Helmholtz's invention, the German physician Donders published the foremost findings on retina degenerations [4].

In the following years several experiments were conducted which intended to improve the image quality in order to resolve even individual cells in the living retina. This was not possible until 1996 when Miller and his co-workers designed a new fundus camera specifically for this purpose, that was equipped with adaptive optics (AO) [5]. Fundus cameras normally provide color photographs of the human eye fundus with a typical transverse resolution of about $\sim$50 μm and field of view of 60°. However, this resolution is insufficient to resolve individual cells, whose size is smaller than 10 μm [3, 5].

Those images were just the first glimpse of what could be done, serving as

[1]The posterior segment is the back two-thirds of the eye, consisting of the vitreous, posterior sclera, choroid, and retina [2]

stimulus for many researchers to improve the living eye microscopic imaging modality.

In 1980 the first scanning laser ophthalmoscope (SLO) was invented by Webb et al. [6]. This device illuminates the retina with a flying laser beam spot and detects the backscattered light with a detector that proved to be much more sensitive than the film used by fundus cameras at that time. Seven years later the same group introduced a confocal scanning laser ophthalmoscope (cSLO), whose key feature is its ability to acquire in-focus images from selected depths using a pinhole. This improved version of the SLO was able to deliver images with higher contrast and better resolution [6, 7].

The cSLO ability to optically section was nonetheless limited by eye aberrations, introduced by the optics of the eye, keeping axial resolution limited to over 200 μm. A solution based on adaptive optics (AO) technology was reported by Roorda et al. [8], where an adaptive optics element was for the first time successfully implemented in a cSLO.

This successful combination of AO technology with cSLO systems allowed the numerical aperture to be maximized, increasing light collection and improving both lateral and axial resolution. For the AO-cSLO, it was reported a resolution of $\sim$2.5 μm lateral and $\sim$100 μm axial, improving the typical cSLO resolution of 5 μm lateral and 300 μm axial [8].

With this deployment of adaptive optics technology in SLOs emerged the possibility to non invasively examine single cells in the living human retina, including rod and cone photoreceptor cells, retinal pigment epithelial (RPE) cells and white blood cells [3, 7–9].

Despite being unquestionably a powerful research tool, adaptive optics imaging systems are as of yet expensive and complex. Therefore, until quite recently, the viability of its clinic application was controversial among clinicians. However, since some commercial devices were launched in the market the interest from ophthalmologists and optometrists in AO imaging has been increasing. Some applications worth mentioning include not only investigation but also diagnosis and follow-up of several diseases: retinal degenerations, inherited color vision deficiencies, albinism and glaucoma [10].

This master thesis is focused on the improvement and optimization of an existing Adaptive-Optics SLO and Line-Scanning SLO setup [11, 12], which was initially designed as a more compact version of a system built in 2012 by

F.Felberer et al. [13].

All the methods and modifications developed in the initial setup are here extensively described, as well as the argumentation behind them.

An additional detection approach with a tilted multimode fiber was tested in order to complement the high quality images of the individual retina cells with images from the smaller blood vessels, inspired by an approach proposed by Chui et al. [14] with an off-set pinhole configuration.

The results discuss all the improvements achieved through the modifications that were implemented, attesting for the success of these optimization steps in obtaining high quality *in vivo* images.

1.2 Thesis Outline

This diploma thesis starts with a background chapter where a description of some essential concepts regarding the human eye are covered, followed by two sections where explanations on the principles behind the Adaptive Optics and the Scanning Laser Ophthalmoscopes are provided. In addition some considerations on the current state-of-the-art are made.

In chapter 3 and 4 the Adaptive Optics system is described thoroughly, starting with the experimental setup in chapter 3 and then focusing on the software characteristics in chapter 4.

The new features and alterations are evaluated and the instrument is used to image healthy volunteers, in order to assess whether or not they have contributed positively for the final image quality. The images obtained from the different experiments are presented and further analysed in chapter 5.

Thesis conclusions and final thoughts on future work are presented in chapter 6.

Chapter 2

Background

2.1 The Human Eye

2.1.1 Structure of the Eye

The eye can be seen as sphere enclosed by three layers (Fig.2.1). The retina is the innermost layer, containing a light-sensitive layer and neuronal structures, which are capable of transmitting visual signals to the brain. The second layer is the uveal tract which is composed of several structures, namely the choroid, ciliary body and the iris. The iris contains a set of muscles capable of adjusting the size of the pupil (which appears as a black central circle). The outermost tissue layer named sclera connects at a junction known as limbus to the cornea, a specialized transparent tissue at the front of the eye that allows light rays to enter the eye [15].

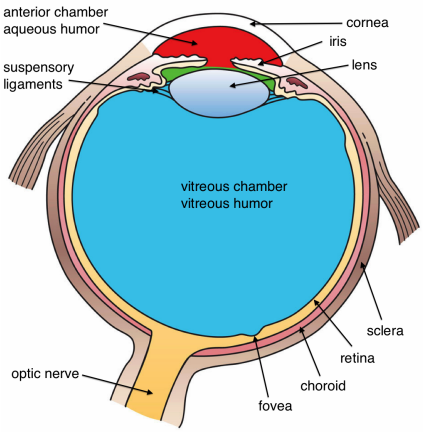

Figure 2.1: Horizontal cross-section through the human eye [16].

Being one of the most important structures of the eye, the retina is in fact part of the central nervous system. The retina consists of several layers,

such as the photoreceptors layer, that contains light sensitive cells that can be subdivided in two main types, the rods and the cones. These two types can be distinguished rather easily in histology due to their differences in size and shape. In addition, cell density varies across the retina, as shown in Figure 2.2. The Fovea is a small central region of the retina densely packed with cones, being in its most central region (foveola) totally rod-free. In the healthy eye, the fovea represents the location with the highest visual acuity. However, the foveal region is not located along the optical axis of the eye but typically lies 2.5 mm temporal of this axis. Among the several layers of the retina besides the photoreceptor layer, the retinal pigment epithelium (RPE) layer should also be here highlighted since it plays a fundamental role for the metabolism of the photoreceptors and is affected by many diseases such as age-related macular degeneration AMD [15, 17].

Nerve fibers and blood vessels enter the eye at a point known as the blind spot or optic disc (see Figure 2.2), situated about 12-15° nasal from the fovea. In this region, because of the lack of photoreceptors, light can not be detected. The maximum field of view (FOV) of the eye is around 108° whereas the fovea FOV accounts for 5° [15, 17].

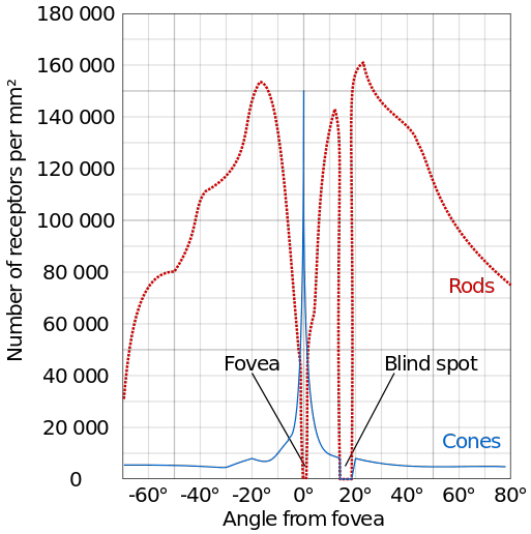

Figure 2.2: Distribution of rods and cones in the human eye. The central location of the fovea is used as a reference for the field angle [18].

Eye motion is essential for the vision process, enabling fixation and tracking of a targeted object. However, it also results in time-variations of eye aberrations (further explained in one of the next sections) as well as in image

motion artifacts[1], which sets high demands on imaging systems.

Micro-saccades, tremors and smooth pursuit movements (drifts), despite being to small to be seen with the naked eye, represent the main source of motion artifacts present in ophthalmologic imaging modalities. These are collectively referred to as involuntary fixational eye movements. Their role in counteracting neural adaptation [2] avoids our visual perception to fade completely [19, 20].

Saccades are fast (10 – 100 deg/s) and highly dynamic movements of the eye, whose amplitude ranges between 2' and 50' [3]. These are the largest and fastest of the fixational eye movements. Drifts are much slower eye movements, that occur between microsaccades, with magnitudes of around 2'. Tremors can be described as a wavelike motion superimposed on drifts with a very small amplitude and a frequency of 40 Hz to 100 Hz [19, 20].

2.1.2 Optical properties of the Eye

The human eye can be seen as an optical instrument whose characteristics can be described as a compound lens system consisting of the three main components: the cornea, the pupil and the crystalline lens.

The first layer light encounters when reaching the eye is the cornea (namely, the first corneal surface: epithelium including the tear film) which acts as a refractive element, being in fact the main refractive element of the eye. The cornea together with the eye lens is responsible for focusing an optical image on the retina. With a mean refractive index of n = 1.377 (difference of 0.377 against air) the cornea accounts for the greater part of the refractive power of the eye. It is also the main contributor to ocular aberrations in the eye [14, 21].

The term pupil refers usually to the hole of the iris (iris aperture). The iris is actually an aperture stop, limiting the angle of acceptance of the imaging system and influencing the amount of light that reaches the retina [21, 22].

Eye accommodation mechanisms are mostly related with controlled changes in the shape and thickness of the crystalline lens and in distances between the posterior corneal and anterior lens surface. This process is responsible for a

[1] Anomalies found during visual representation in any imaging modality.

[2] The adaptive neural mechanisms normalize responses across neurons when there is a unchanging/uniform visual stimulus.

[3] One degree (1°) corresponds to sixty minutes (60').

focused image on the retina even in the case of near objects [21].

The optical phenomena and human eye properties described in this section are important in the context of the adaptive optics scanning laser ophthalmoscope developed in this thesis work, since they affect in different ways the performance of the imaging system.

Reflection, Absorption and Scattering

Light may be lost in any of the optical media anterior to the retina by spectrally varying reflection, scattering, and absorption [23].

The light losses that occur in the optical media due to reflection are relatively small and the reflectance losses are mainly due to the cornea-air interface. About 3% of the incident illumination is reflected here due to the substantial difference in the refractive indices of air and cornea. Nevertheless the cornea reveals itself as a remarkably transparent material across the visible spectrum, absorbing less than 10% of the incident light at 800 nm [22, 23].

In order to image the retina and nearby structures it is crucial to detect the light which is backscattered from the posterior segment. However, the amount of light backscattered is only around 1/100000 depending on the wavelength. Another limiting factor for the amount of light leaving the eye is the pupil size. The two mentioned factors can reduce the amount of reflected light by a factor between $10^{-5} - 10^{-6}$ [24].

Most of the ophthalmologic instruments use near infrared or red light sources to reduce absorption and scattering by retinal and choroidal tissues [25].

The phenomenon of light scattering results from localized (particle-like) irregularities of the refractive index within the ocular media leading to the spread of the light at larger angles over the retina. The main sources of scattered light in the eye are (1) forward scatter from the cornea, the lens and the retina,(2) back scatter from the fundus [22, 23].

One of the reasons to perform retinal imaging through the narrow pupil of the eye is to avoid the strong scattering effect produced at the outermost layer of the eye - sclera [24].

In adaptive optics systems backscattered light is detected via a confocal aperture to obtain images of several retinal structures. However, in 2012 Chui et al. [14] used for the first time forward scattered light in an adaptive optics

ophthalmoscope in order to improve image contrast of the small vessel networks in the living retina, without being corrupted by a strong signal from directly backscattered light from the in-focus plane. This multiple scattered light may not only result from light-tissue interactions following forward scatter, but also from backscatter from out of focus planes and lateral scatter off tissues that are poor absorbers [25].

Diffraction and Aberrations

Retinal images in the human eye are affected by optical aberrations, which play a major role in image quality degradation. They can be split into two main groups: chromatic aberrations and monochromatic aberrations.

Chromatic aberrations (dispersion) are caused by the dependence of the ocular components' refractive index on the wavelength. Despite being also present in the human eye, chromatic aberrations are not so relevant in the scope of scanning laser ophthalmoscopes, since these systems typically use light sources with narrow bandwidth for imaging [24].

Monochromatic aberrations vary significantly between individuals, depending on surface asymmetries and surface tilts between the optical components of the particular eye and their relative locations with respect to the pupil. A smaller pupil minimizes the effects of higher-order aberrations, since it reduces the number of rays contributing to the illumination spot on the retina. However, as explained later on in this section, smaller pupils provide less resolution [21].

High order aberrations are unstable over time. Microfluctuations during accommodation by the lens, local changes in tear-film as well as head and fixational eye movements are among the largest contributors for temporal short-term (seconds/minutes) instabilities. These rapid changes with respect to the wavefront sensor represent a major barrier to an accurate real-time measurement of high order aberrations [21, 26].

Without these monochromatic aberrations the eye would be ideal. Plane waves incident on an ideal perfect eye should be converted to perfectly spherical waves that converge to a small spot on the retina, as represented in Figure 2.3. However, the eye is far from a perfect optical system, which means that at least some of the incident parallel rays fail to converge perfectly. Aberrations are the errors introduced by the optics of the eye that cause the perfectly spherical

converging wavefronts to distort from their ideal shape [23].

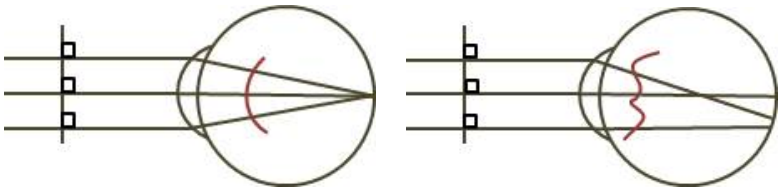

(a) (b)

Figure 2.3: The path of rays in an ideal eye (a) and in an aberrated eye (b), adapted from [23].

Lower-order aberrations of the eye, such as myopia (negative defocus), hyperopia (positive defocus) and astigmatism, can be easily corrected with spectacles or contact lenses and account for approximately 90% of the overall wave aberration. The same does not hold for high order aberrations, such as coma or trefoil, which are more complex and irregular. These are usually related with the shape and position of the lens and the surface of the cornea. Despite not severely affecting visual function, higher order aberrations interfere with high-resolution retinal imaging [21, 26].

Several wavefront sensors are nowadays available to measure the monochromatic high order aberrations of the complete eye. These include, the spatially resolved refractometer, the laser ray tracing technique and the Shack-Hartmann (SH) wavefront sensor. In this thesis, a SH sensor was used, whose working principle will be further explained later on. The SH-sensor measures light that scatters off the retina, which in an aberration-free case means that plane waves emerge from the eye. After reconstructing the wavefront shape (also defined as wave aberration function), explained in a later section, the way how eye aberrations vary across the pupil is usually represented in a two-dimensional surface map at the pupil plane. This aberration map plots, for each spot on the pupil, the difference between the actual wavefront and a reference wave, usually a plane wave [24, 27].

Diffraction is a phenomenon related with the wave nature of light when it passes through an aperture. In the case of the eye, diffraction occurs due to the interaction between light passing through the optics of the eye and the edge of the iris. Even in an aberrations-free eye, an infinitesimal small point cannot be formed on the retina due to diffraction.

The point spread function (PSF) of the eye corresponds to the retinal image

produced by an infinitely distant point light source. It provides a complete description of image quality at that retinal location. The PSF resulting from an ideal eye is only broadened due to the diffraction phenomenon.

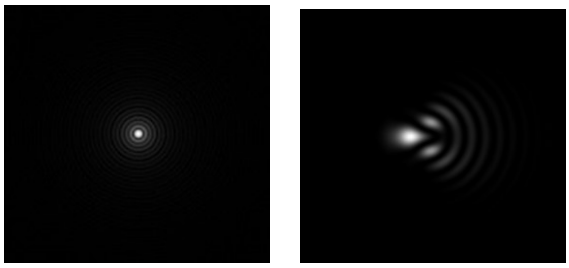

(a) (b)

Figure 2.4: Point spread function of a perfect eye (a) and an aberrated eye (b). Adapted from [28].

As can be seen in Figure 2.4a, the PSF of an aberration free eye appears as a bright central disc surrounded by dimmer rings, the so called Airy disk. These rings are a consequence of light spreading in different directions when an initial planar wave passes trough the eye's pupil aperture. For this reason, the fundamental maximum achievable resolution of any optical system is limited by diffraction. The amount of diffraction depends on the aperture size and wavelength of light, being greater for smaller pupils and shorter wavelengths. [23].

Polarization characteristics and waveguide properties

Light's polarization state in the ocular media can be changed by several mechanisms, that have already been studied resorting to techniques such as polarization sensitive Optical Coherence Tomography (OCT)[4]. These changes occur mostly through birefringence, diattenuation, and by polarization scrambling effects [24].

In recent publications the polarization properties of some structures of the eye have been extensively described. In the retina it is known that both the retina nerve fiber layer (RNFL) and the Henle fibers have birefringent properties as well as the cornea and sclera [30, 31].

The photoreceptor layer has shown to preserve light polarization. The

[4]OCT is an imaging technique that performs high-resolution, cross-sectional tomographic imaging of the internal microstructure in biologic tissues [29].

waveguide nature of the photoreceptors (Stiles–Crawford I effect)[5] in the context of imaging techniques contributes for an increase of contrast between this layer and surrounding matrix and tissues [24].

The influence of the polarization state of the light on wavefront measurements has been studied by a few research groups several years ago, who, through different experiments, have shown that there is no meaningful impact [24].

2.2 Principles of Adaptive Optics

"Adaptive Optics is one of the most exciting advances in optical imaging in the past twenty years" in Principles of adaptive optics [32].

The adaptive optics concept has first emerged in the astronomy field in 1953 with Horace Babcock. At that time he proposed the use of an optical element which could correct for time-varying aberrations arising from the atmosphere turbulences in stars imaging systems [33]. Generally, it can be described as a method that improves the optical signal quality in an imaging modality by acting actively on the optical beam wavefront, after passing through a media. [24, 32].

A standard AO system is comprised of three key components illustrated in Figure 2.5: (1) a wavefront sensor, (2) wavefront corrector, typically a deformable mirror (DM) and (3) real-time feedback control software.

Light exiting the eye reflects off the deformable mirror and is directed by a beamsplitter into the wavefront sensor, which measures wavefront distortions, and the imaging device. The software uses the data collected in the sensor to calculate the most appropriate drive voltages to be applied to the DM. These voltages cause the necessary changes in the DM's shape so that it compensates correctly for the distorted wavefront. Afterwards, an improvement in the image quality of the imaging device should be detected. The entire procedure is continually being repeated in a closed-loop. In real-time AO systems the process described above runs fast enough to follow the temporal changes in the ocular aberrations, caused by the fixational movements of the eye. [24].

[5]Effect that refers to the directional sensitivity of the human photoreceptors, more pronounced the cones [24]

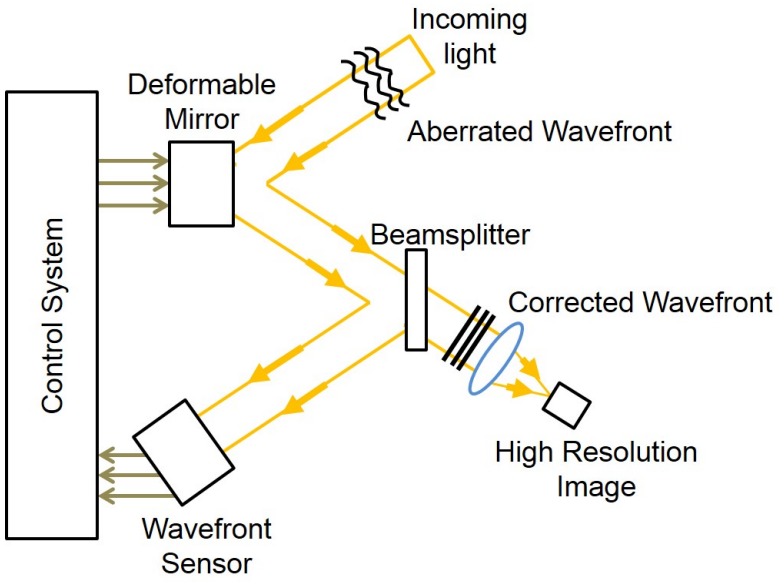

Figure 2.5: Basic schematic of an AO system. Adapted from [34].

2.2.1 Wavefront sensing

Wavefront sensing is one of the most critical steps when using AO imaging systems. From several sensing methods that have been developed, the sensor used in this thesis, as well as in many other groups working with similar systems, was the Shack–Hartmann (SH) wavefront sensor [8, 35].

The sensor is able to dynamically measure the aberrations generated by the cornea and the crystalline lens, while the eye's pupil is regarded as the optical limiting aperture.

Typically, a Shack-Hartmann wavefront sensor consists of a two-dimensional array of micro lenses (lenslets), all with the same diameter and focal length, and a CCD[6] camera. The wavefront is spatially sampled by the lenslet array that splits light into a number of small beams, which are then focused onto a spotfield on the camera. Each spot's intensity and location are analysed in order to calculate their displacement from the center.

Light reflected from the retina of an aberration-free eye results in a regularly spaced grid of spots in the focal plane of the lenslet array, whereas the spots of an aberrated eye are displaced from the optical axis of each lenslet (cf. Fig. 2.6).

[6]CCD stands for charged couple device.

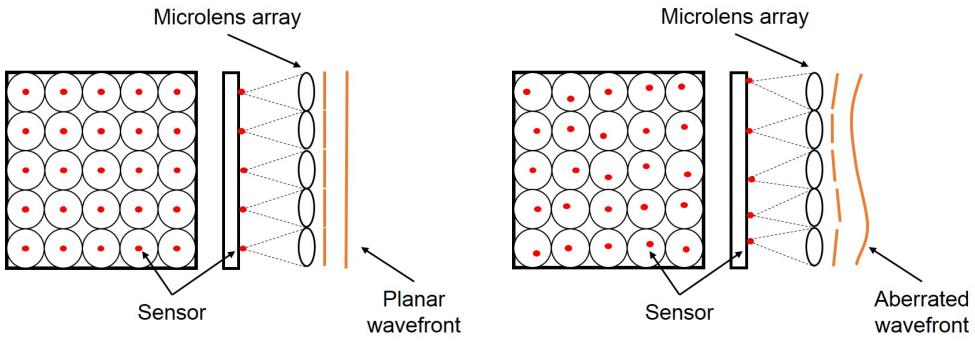

(a) (b)

Figure 2.6: Shack–Hartmann wavefront sensor operation principle. Schematic of a mircrolens array focusing a plane wavefront (a) and a distorted wavefront (b). Adapted from [36].

To determine the displaced position $\underline{\sigma}$ of each wavefront sensor spot a centroid (center-of-mass) algorithm is used. In this thesis the wavefront sensor used a simple centroid algorithm which measures the first moment of the focal-plane intensity distribution of each sub aperture and returns the center of gravity $\underline{s}$ [37].

$$\underline{s} = \frac{\sum_{ij} \underline{r}_{ij}.I_{ij}}{\sum_{ij} I_{ij}} \tag{2.1}$$

The displacement is given by $\underline{\sigma} = \underline{s} - \underline{r}$ where $\underline{r}$ is the reference position. I_{ij} is the focal plane intensity at the position r_{ij}.

By knowing the spots' displacements in both X (Δx_s) and Y (Δy_s) directions and the focal length F of the focusing optics, the local wavefront slopes (wavefront's first derivative) can be calculated using equations (2.2)(2.3).

$$\frac{\partial W(x,y)}{\partial x} = \frac{\Delta x_s}{F} \tag{2.2}$$

$$\frac{\partial W(x,y)}{\partial y} = \frac{\Delta y_s}{F} \tag{2.3}$$

The posterior reconstruction of the wavefront is performed by integrating these slopes.

Reconstruction Algorithms

Typically, wavefront reconstruction methods are split between zonal and modal. The zonal reconstruction is a direct numerical integration, as a contrast to the

modal approach which is a polynomial fitting where any complete set of basis functions can be used [38].

There is not much literature covering the advantages and disadvantages of each approach in specific conditions, such as large/small pupils or circular/irregular shaped pupils. However, since both algorithms were available in the software provided for the SH-sensor used, in this thesis the two of them were tested in order to investigate which algorithm yielded the best image quality *in-vivo*.

In the zonal approach, slope measurements are made over discrete zones according to a specific sampling geometry. The grid configuration used by the software provider is depicted in figure 2.7, known as Hudgin geometry. Horizontal and vertical dashes correspond to x and y slope sampling positions. The dots are the estimated phase points, each representing an equal subregion of area P^2. This configurations yields N^2 phase points and 2N(N-1) slope measurement points [39].

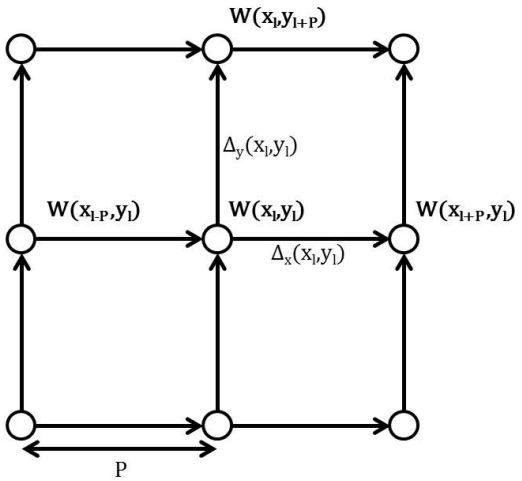

Figure 2.7: Hudgin sampling geometry adapted from [40].

The phase value at the position (X_l, Y_l) can be calculated as follows:

$$W(x_{l+P}, y_l) =: W(x_l, y_l) + \Delta_x(x_l, y_l) \tag{2.4}$$

$$W(x_l, y_{l+P}) =: W(x_l, y_l) + \Delta_y(x_l, y_l) \tag{2.5}$$

Where $\Delta_x(x_l, y_l)$ and $\Delta_y(x_l, y_l)$ are the measured slope values.

Based on equations 2.4 and 2.5 the problem can be written in the matricial form:

$$\mathbf{\Delta} = \mathbf{AW} \Leftrightarrow (\mathbf{A}^\dagger\mathbf{A})\mathbf{W} = \mathbf{A}^\dagger\mathbf{\Delta} \tag{2.6}$$

Where $\mathbf{\Delta}$ is a column vector containing all the slope measurements and $\mathbf{W}$ is the N^2 length vector of the unknown phase values. $\mathbf{A}$ and its transpose $\mathbf{A}^\dagger$ are sparse rectangular matrices. The standard Least Squares solution can not be used since the product $\mathbf{A}^\dagger\mathbf{A}$ is singular[7].

A matrix iterative approach, described thoroughly in [40], is used instead to compute the wavefront at each node, until the values settle to within a given tolerance. According to the software provider manual, the number of iterations required for a satisfactory convergence is around 2N, being N the number of phase points estimated [40].

When using the modal method the wavefront surface is described in terms of a set of Zernike polynomials, which are very common in the optics context due to their close relationship with the aberrations introduced in optical systems. As such, single polynomials can be associated to specific optical aberrations, such as tip, tilt, defocus, astigmatisms as well as higher order aberrations [38, 41].

In the modal approach the wavefront may be generally defined as:

$$W(x,y) = \sum_n a_k Z_k(x,y) \tag{2.7}$$

Each a_k value represents the coefficient for a different Zernike mode $Z_k(x,y)$, assuming a linearly independent set of modes. Zernike modes $Z_k(x,y)$ are continuous and analytic through the first derivative which allows the computation of the wavefront gradient to be expressed as [41, 42]:

$$\frac{\partial W(x,y)}{\partial x} = \sum_n a_k \frac{\partial Z_k(x,y)}{\partial x} \tag{2.8}$$

$$\frac{\partial W(x,y)}{\partial y} = \sum_n a_k \frac{\partial Z_k(x,y)}{\partial y} \tag{2.9}$$

The appropriate set of coefficients a_k can be computed using both equations 2.8 and 2.9 as well as the measured local wavefront slopes, typically through a method such as the Least Squares fitting.

[7] A singular matrix is a square matrix that does not have a matrix inverse.

2.2.2 Control system and wavefront correction

In any adaptive optics system the control system represents the most important link between the wavefront sensor and the wavefront corrector. In this thesis work a deformable mirror (DM) was used as wavefront corrector. The control system converts the reconstructed wavefront into a set of commands that are applied to the DM in order to minimize the residual wavefront error in real time, as shown in Figure 2.8.

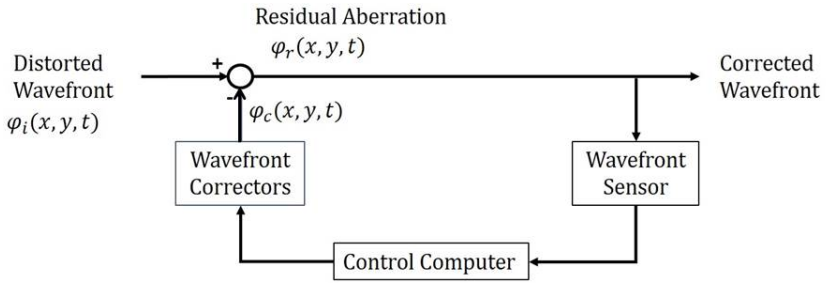

Figure 2.8: Closed-loop control system of an Adaptive Optics setup. Adapted from [24].

The surface deformations on the DM are produced by individual voltages applied at each actuator. The deformation caused by each actuator can be described by its influence function. The measurement of the influence matrix **IM** containing the individual influence function for each DM actuator is a general procedure when calibrating the system. The influence matrix has N columns corresponding to the number of actuators and N rows where N=2K (bi dimensional domain of the wavefront: x and y axis), where K is the number of lenslets of the wavefront sensor. To obtain the influence matrix each actuator is individually activated (pushed and pulled) and its corresponding wavefront effect is measured. Any mirror deformation can therefore be written as a linear combination of these influence functions.

The influence matrix **IM** defines the sensitivity of the wavefront sensor to the DM deformations. Therefore, the actuator command vector **v**, containing the voltage values to be applied in order to produce a desired correcting deformation, can be computed as follows:

$$\mathbf{v} = \mathbf{IM}^{\dagger}\mathbf{s} \tag{2.10}$$

Where **s** is the measurement vector from the wavefront sensor and $\mathbf{IM}^{\dagger}$ the pseudo-inverse of the influence matrix **IM**.

Typically, to evaluate the progress of the wavefront correction and the performance of the feedback loop the root-mean-square (RMS) value of the residual wavefront error is monitored frame by frame. Essentially it measures how much the wavefront deviates from the perfect plane wave [24]. The RMS value can be calculated as the standard deviation of the wavefront. Alternatively, when using the Zernike polynomials expansion to describe the wavefront, the RMS is simply the square root of the sum of the squared Zernike coefficients. Tip and tilt errors are usually removed from this calculation since they do not affect image quality [38].

2.3 Adaptive Optics Confocal Scanning Laser Ophthalmoscope (AO-cSLO)

2.3.1 cSLO

The working principle of scanning laser ophthalmoscopes is very similar with the one of scanning laser microscopes. In the case of an ophthalmoscope the eye's optics work as the objective and the retina is in general the sample.

Usually, illumination in the SLO is made through a small central portion of the pupil, while back reflected light collection is performed over the entire remaining pupil. This method avoids strong artificial reflections from the cornea, that would otherwise degrade image quality.

An image is produced by continuously recording scattered light from a focused spot as it is raster scanned across the region of interest to be imaged. A scanning laser ophthalmoscope has two scanners that synchronously deflect light in 2 dimensions, a resonant scanner (x-direction) and a galvo scanner (y-direction). Sampling consists of a rapidly repetitive horizontal sweep (X-axis) that is punctuated by incremental, vertical displacements of the horizontal sweeps (Y-axis), as represented in Figure 2.9.

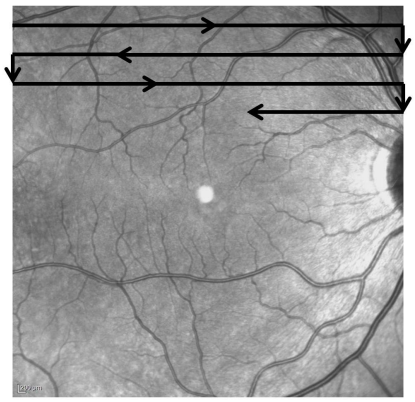

Figure 2.9: Sampling pattern of a scanning laser ophthalmoscope. The camera image was adapted from [11] with permission.

Despite being well-focused onto a specific plane in the retina, the illuminating light scatters throughout its thickness. Traditionally, in confocal imaging a pinhole is placed before the detector, in an imaging plane that is conjugated to the retina plane, in order to reject all out-of-focus backscattered light (cf. Figure 2.10). The optical sectioning property of confocal imaging improves considerably the resolution in both axial and lateral directions, being the equivalent PSFs about 30% narrower than in the case of conventional wide-field illumination systems. The larger this small aperture the greater the proportion of scattered light detected, therefore resulting in a trade-off between resolution and intensity of the obtained images [24, 43].

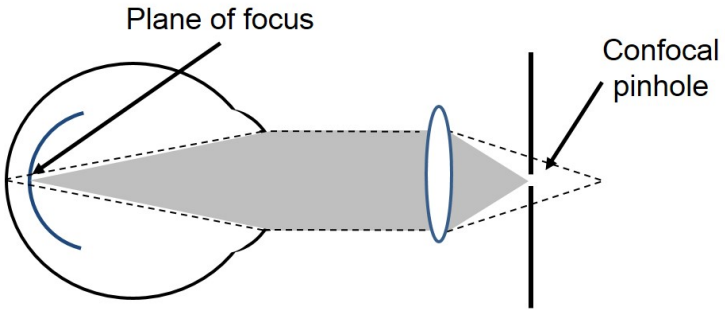

Figure 2.10: Basic concept of optical sectioning (confocality). The optics are designed so that light scattered from the plane of focus can pass through the confocal pinhole. Light coming from planes above or below the focal plane is out of focus when it hits the pinhole (dashed lines), being most of it rejected and therefore not contributing to forming the image.

The combination of the raster scanning method with the confocal approach,

and resultant minimization of optical cross talk [8], yields high contrast images.

2.3.2 The role of adaptive optics

The first ones who tried to use adaptive optics with the purpose of improving retinal image quality from a scanning laser ophthalmoscope were Andreas Dreher and colleagues in 1989. In the case of eye imaging modalities, by extracting information about the eye wavefront monochromatic aberrations, these aberrations can be compensated for in order to improve image quality [24].

With AO technology, the ability to visualize with high resolution distinct layers of the retina (e.g. nerve fibers, blood vessels, and photoreceptors) provided by the confocal nature of the cSLO is further enhanced. The high contrast images delivered by AO-cSLO systems arise from two main reasons: (1) smaller illuminated spot on the retina, which stems from the aberrations-corrected ingoing beam and (2) less interference from out of focus light, which is rejected by the confocal aperture [44, 45].

2.3.3 Resolution of the AO-cSLO

The resolution of the confocal SLO is given by:

$$PSF_{AO-cSLO} = PSF_{in} \times (PSF_{out} \otimes D(x, y)) \tag{2.11}$$

Where PSF_{in} and PSF_{out} are the point spread functions in and out of the eye respectively. Theoretically, in this case the PSF will be below diffraction limit [9]. $D(x, y)$ represents the two-dimensional spatial function of the pinhole. Large pinholes can be ignored, making the PSF equal to the product of both ingoing and outgoing PSF. [45]

Assuming then a well designed diffraction-limited ophthalmoscope, the lateral resolution is only limited by the width of the diffraction-limited point

[8] Optical cross talk is defined as the unwanted light that is back scattered from retinal planes other than the plane of interest

[9] An optical system with the ability to produce images with resolution as good as the instrument's theoretical limit is said to be diffraction limited.

spread function (PSF), which can be calculated as follows:

$$\delta = \frac{1.22\lambda_0 F}{nd} \tag{2.12}$$

where δ is the Airy disk radius, λ_0 is the central wavelength of light being used, n the refractive index of the medium, F the focal length of the eye lens and d the eye's pupil diameter. However, the above equation can only be considered as an approximation since the SLO employs the human eye as its objective lens [10], whose optical quality is not good enough to assume a diffraction limited state. The real PSF turns out to be a complex speckle pattern, which is different for each individual [24].

By making the confocal aperture small both lateral and axial resolution are improved. It is generally accepted that a pinhole size with half of the size of the airy disk of the detection optics yields the best lateral resolution [46], which was recently demonstrated in a study by LaRocca et al. [44]. However, this will only be effective if the double pass PSF that is re-imaged onto the confocal pinhole plane is compact. If not, an insufficient amount of light will reach the detector. The role of the adaptive optics elements is not only to make the focused light on the retina more compact but also to re-image the returning light back onto the confocal pinhole. The resolution will be improved to a greater extent with larger pupils or shorter wavelengths, due to the resultant decrease in the amount of diffraction [45].

2.3.4 Confocality through a single-mode fiber

Confocal imaging can also be achieved through an optical fiber, as shown by [47, 48], though presenting some significant differences.

An optical fiber acts as a coherent detector in contrast with a pinhole. The size of the pinhole affects the confocality and the signal level. Likewise, in the fiber case the signal intensity also depends on its core size, yet adding to this, the mode of the incoming signal and the numerical aperture of the coupling lens will also influence the overall performance [43].

Acting as an ideal pinhole, in both shape and size, the core of an optical fiber makes optical fiber detection more advantageous since smaller cores (of about microns) are easier to produce than conventional pinholes. Another major advantage when using an optical fiber is the flexibility it provides as well

[10] In microscopy, the objective lens of a microscope is the one at the bottom near the sample.

as the resultant more compact system, where the detector can be physically isolated from the confocal head. Adding to these advantages, it is also known that it is less likely for the core of a fiber to become occluded by dust, which then results in undesirable aberrations and decrease in intensity. Nonetheless, one major disadvantage is the difficulty associated with an efficient coupling of light into the optical fiber [43, 48].

In this thesis the preferred choice for confocal detection was a single-mode fiber. However, a pinhole detection configuration was deployed and tested for comparative purposes.

2.3.5 Offset Pinhole - Adaptive Optics SLO

In 2012, Stephen Burns and his team came up with a novel approach in combination with the traditional AO-cSLO that exploits multiple scattered light instead of direct backscattered light from the human retina [14].

When using multiple scattered light smaller structures such as microvascular network or erythrocytes have a much more pronounced presence in the acquired images. When using a centred confocal pinhole the microvasculature appearance is masked by the highly specular light coming from structures in the same focused plane like the retinal nerve fiber layer (RNFL) [14].

The technique mainly consists of collecting backscattered light through a displaced larger pinhole (10× Airy disk diameter), instead of using a centred aperture, as illustrated in Figure 2.11.

In a very recent study by Chui et al. [49], the offset-pinhole AO-SLO, proved not only to provide structural images of the retina microvascular network but also perfusion images if combined with motion correction techniques in post-processing steps. As such, the offset-pinhole approach reveals itself as a brilliant alternative to oral fluorescein angiography, the gold standard technique for visualization of the retinal capillary circulation. A major drawback inherent to this traditional technique stems from its invasive nature since it depends on the use of exogenous contrast agents, which is not the case of AO-SLO systems.

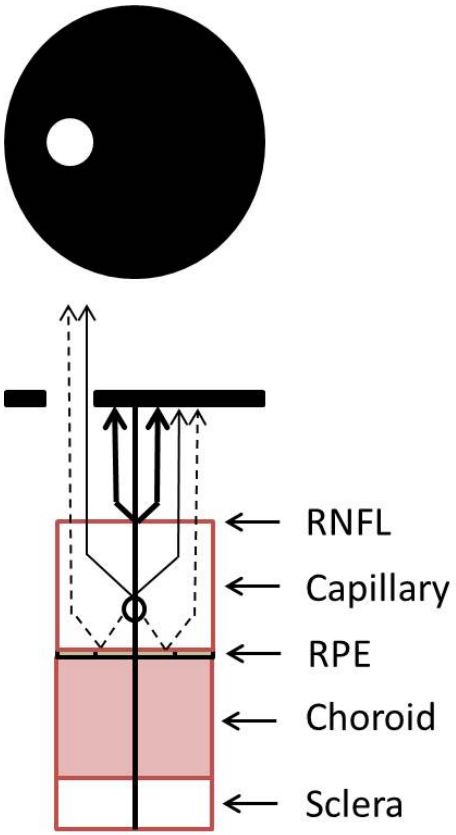

Figure 2.11: Schematic diagram illustrating the effect of a lateral displaced confocal aperture on the visibility of the capillaries. Specular reflection from the RNFL (heavy arrows) is blocked by the offset aperture, allowing more multiple scattered light (dashed arrows) to return back to the detector. Adapted from Chui et al. [14].

Instead of using a larger pinhole, as suggested by Chui et al. [14], in this diploma thesis the use of a larger multimode optical fiber for light detection is proposed. The use of this fiber with an intentional tilting aspires to achieve images of the retinal microvasculature similar to the ones obtained by the above mentioned research group.

2.4 State of the Art of AO-cSLO

The potential of adaptive optics SLO systems has been explored in the last few years by some groups worldwide, who were able to improve in many ways the performance of these devices.

Some improvements aimed to minimize the influence of instrument aberrations by implementing new designs. Reported enhancements on image quality arose from the use of smaller confocal pinholes and also from novel registration and processing algorithms [3].

With AO-SLO imaging opportunities emerge to study the etiology of retinal diseases on a cellular level as well as improved non-invasive tools not only to identify the best candidates for given therapies but also to follow-up those therapies. Without the purpose of extensively review all the potential applications and capabilities of state of the art AO-cSLO, some examples are mentioned here to enhance the importance and utility of systems as the one optimized in this diploma thesis.

Aiming to study blood velocity profiles for different cardiac phases in retinal vessels, in a recent study by Zhong et al. [50], the motion of individual blood cells in the smallest retina capillaries was recorded. This evidence clearly illustrates the ability of AO-SLO systems to provide microscopic resolution with a real-time view of the retina.

Not less impressive were the results achieved by Alfredo Dubra's group at the University of Rochester [9], who was able to resolve not only the cones in the central fovea but also the rod photoreceptors at more eccentric regions in the living human eye. There is, however, a certain difficulty associated with rod imaging due to their small diameter (around 2 microns) and broad angular tuning, which results in a smaller amount of light being collected through the pupil. Nevertheless, these kind of images provide a valuable assessment of the retinal degeneration progression, which often starts by affecting the rods.

Several more clinical applications have been explored for AO-SLOs in the last years. For instance, a very recent study by Burns et al. [51] has reported the applicability of an AO-SLO system to investigate the damage and abnormal changes caused by non-proliferative diabetic retinopathy (NPDR).

For AO-SLO systems image distortions resulting from the eye movements can be assessed at a finer spatial scale. As a result, the warping that occurs in individual frames and between frames can be used to accurately correct for the eye motions artifacts [20]. Several approaches had been exploited in order

to get a better tracking method of the eye retina. These new methods allow for a real-time tracking of the retina, either by computing in real time the in-frame warping or by coupling a separate eye tracking system to an AO-SLO, as proposed by Dan Ferguson and Dan Hammer at Physical Sciences Corporation and Steve Burns at Indiana University [52]. These kind of solutions are especially attractive for microsurgery, where it is essential to achieve a real-time stabilization of the retinal image [3].

Nowadays, the opportunities provided by such systems are immense, allowing a non-invasive microscopic scale monitoring of the human retina. It is also a valuable tool to monitor the progression of diseases or to follow up the efficacy of therapies and drugs for retinal diseases [10].

Retinal imaging based on adaptive optics sounds therefore very promising in the foreseeable future due to the advances that were witnessed so far just in the last couple of decades.

Chapter 3

Adaptive Optics SLO: Experimental Setup

A lens-based adaptive optics SLO has been formerly developed by G.Aschinger [12], where the main purpose was to combine a more compact design (compared with a system introduced by F.Felberer et al. [13]) with a new deformable mirror and a high resolution wavefront sensor. This setup was later combined with an overview line scan laser ophthalmoscope by P.Vetschera [11].

At the start of this thesis the AO-SLO was not able to successfully deliver high-resolution images of the living human retina, mainly because the AO-loop was not stable and therefore not able to accurately correct for the eye aberrations. The reasons why the system was unstable for *in vivo* measurements were unknown. However, it worked when imaging the model-eye, which consists of an achromatic lens(f=30 mm. d=2.54 mm) and a sheet of paper.

As such, the first section of this chapter starts by briefly reviewing what has been previously done, followed by a description of the AO-SLO system and work that has been performed to improve the setup. It intends to explain all the flaws found in the system as well as to detail the whole set of modifications that were deployed and resultant improvements. A complete characterization of the system is done in the third section. The fourth section aims to describe the two alternative signal detection configurations tested: confocal pinhole and multimode fiber. The fifth and last section intends to provide a brief explanation of the wide-field retinal overview, provided by the line-scanning laser ophthalmoscope, and to describe the improvements that were made in this system.

3.1 The AO-SLO Instrument

The lens based cSLO design is shown in Figure 3.1, which includes both the optical pathway for illumination and collection.

As explained by Aschinger [12] one of the main purposes of using lenses instead of spherical mirrors (as are used in standard AO-cSLO systems) is to decrease the aberrations introduced by the system itself. All lenses used are coated for near-infrared applications to minimize chromatic aberrations. More advantages of this lens based approach can be found in [12].

To avoid back reflections from the lenses into the SH-sensor polarization optics are used. To do so, a polarizing beam splitter (PBS) was placed after the light source (cf. 3.1). After traversing it, the incident light beam will be linear polarized. After the last lens f_8 the light transverses the quarter wave plate (QWP) twice, the first when entering the eye and a second time when back reflected from the retina. The back-reflected light is therefore in a linear state, that is orthogonal to the incident polarization state.

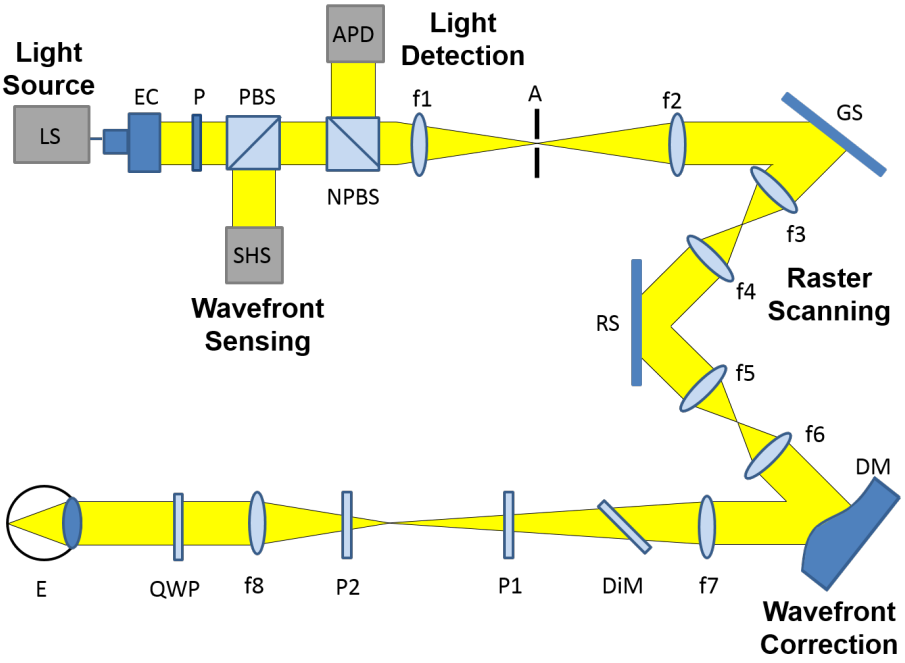

Figure 3.1: Scheme of the AO-cSLO experimental setup. LS: Laser source, EC: Entrance collimator, P: Polarizer, PBS: Polarizing beam splitter, NPBS: Non polarizing beam splitter (50% splitting ratio), $f_1 - f_8$: achromatic lenses, A: Aperture, GS: Galvo scanner, RS: Resonant scanner, DM: Deformable mirror, DiM: Dichroic mirror, P1-P2: Prisms, QWP: Quarter wave plate, E: Eye, SHS: Shack-Hartmann sensor, APD: Avalanche photo diode.

The main elements comprising the AO-SLO can be split into: light source, wavefront sensing, wavefront correction, raster scanning and light detection, identified in figure 3.1.

Light Source: The light source used for both imaging and wavefront sensing is a superluminescent diode (Superlum SLD-371) operating at 842.8 nm with a spectral width of 50.8 nm (full width at half maximum). Usually, light sources in AO-SLO systems are highly incoherent in order to reduce speckle effects on the final images, which arise from the interference of light backscattered from the complex microstructure of the retina [24]. Despite being scanned in a raster on the retina, the light is descanned on the return path, resulting in a stationary beam. This makes it possible to use the same light for both wavefront sensing and imaging. Since the wavefront sensor sees the backscattered light as if it was coming from a single spot, it is possible to measure aberrations [53]. One advantage of using the same light for both purposes is the reduction of non-common aberrations between the wave aberration and imaging light that might reduce AO-correction performance [8].

Wavefront sensing: The Shack-Hartmann (SH)-sensor used for this adaptive optics setup is fabricated by Optocraft and it is supplied with the software SHSWorks. The software, which can be driven in a Matlab or a Labview (National Instruments, Austin, TX) interface, allows the user to measure the wavefront and to compute different wavefront specifications, such as the RMS. Note that in this setup the wavefront sensing is polarization sensitive, in order to avoid interferences from reflexes within the system, making use of polarization optics as explained above.

Wavefront correction: The deformable mirror consists of a membrane that can be deformed by 97 actuators (Alpao HI-SPEED DM97-15), placed at a plane conjugate to the entrance pupil of the eye. Aberrations are corrected on both the ingoing and outgoing light paths, which contributes in two ways for the optical quality in the confocal AO-SLO. (1) By correcting aberrations on the ingoing path, light is focused to a more compact spot on the retina; (2) By correcting aberrations on the outgoing path, backscattered light from the retina is refocused to a compact spot at the confocal aperture [45]. The DM was driven in a LabView (National Instruments, Austin, TX) interface.

Raster scanning: To get a two dimensional image of the retina a resonant scanner (GSI-Lumonics) with a natural frequency of ∼4 kHz is responsible for scanning the rows (x-direction) and whenever a row is finished a galvo scanner (model 6230H from Cambridge Technology) is responsible to adjust its angle to the next line (y-direction). Since each line of the sample is scanned in both directions by the resonant scanner, the line scanning rate is ∼8 kHz. The resonant scanner signal works as the master clock for a Field Programmable Gate Array (FPGA) unit. This unit provides not only the driving signal for the Galvo scanner but also the start trigger for the data acquisition [12].

Light detection: When light enters the eye it is transmitted through birefringent materials, such as the cornea, which modify its polarization characteristics. Therefore, when it is backreflected from the retina (retinal photoreceptor layer is known to preserve light polarization) and crosses the QWP its polarization state is not exactly in a linear orthogonal state to the incident light polarization state. As such, and in order to maximize light collection at the APD, this set-up's light detection is polarization insensitive (cf. Fig.3.1).

Laser safety considerations: The international laser safety standards (EN-60825-1) provide the safety limits for the light power values. A power reaching the eye below 700 μW is regarded as safe for the used laser wavelength region (840 nm), even in the case of single point illumination (without scanning).

Beam diameter: The beam diameter can be measured using a WinCam with Data Ray software, by considering a diameter where light intensity drops to $1/e^2$ ($\approx 86\%$) of its maximum value. Before the collection optics a beam diameter of 8 mm was measured, which corresponds well with the size of the SH-sensor. At the eye a beam diameter of 6.9 mm was measured.

3.1.1 Avalanche Photo Diode

The selection of a detector in an AO-cSLO is critical, since the amount of light that can be used to expose the retina is limited to ∼700 μW according to the laser safety standards. Adding to this, only a small amount of light, about 1/10000 of the total power reaching the eye, will be reflected from the

retina. This reflected light is posteriorly sampled in a fine scale (less than 1 μm per pixel), which results in a very low number of photons per pixel. If we consider the quantum efficiency[1] of the detector, the electron number will be even smaller.

In this thesis two different APD modules were tested: the Si-APD-Modul LCSA500-10SMA from Laser Components and the C10508 model from Hamamatsu. Table 3.1 shows the characteristics of both APDs [54, 55].

Table 3.1: Characteristics of the different APD-modules.

	Laser Components APD	Hamamatsu APD
Photoelectric sensitivity (V/W)	$5.00 \times 10^{+6}$	$1.25 \times 10^{+7}$
Spectral response range (nm)	$400 - 1100$	$400 - 1000$
Peak sensitivity λ (nm)	905	800
Bandwidth-DC (MHz)	10	10
Noise equivalent power (pW.Hz$^{-1/2}$)[2]	0.03 at 905 nm	0.04 at 800 nm
Active area diameter (mm)	0.5	1

Tests and Discussion

In order to compare the quality of the images provided by each of the above mentioned APD-modules the ratio of signal power to the noise power corrupting the signal was calculated using a model-eye.

To prevent inaccurate conclusions resulting from a potential saturation of the detectors, the measurements were performed with a lower power at the eye, around ≈ 87.7 μW.

Signal-to-noise ratio (SNR) is calculated as follows:

$$SNR = 10\ log_{10}\frac{\sigma_{image}}{\sigma_{noise}}\ [dB] \tag{3.1}$$

where σ_{image} is the standard deviation of the image overall intensity and σ_{noise} is the noise standard deviation.

[1] Quantum efficiency is defined as the ratio of the number of electron-holes pairs generated in the photo detector to the number of incident photons. It is expressed as a percentage (%) [54].

[2] The noise equivalent power is the level of signal power required to obtain a signal-to-noise ratio of unity [54].

The σ_{noise} was measured by blocking the light path so that no light was sent to the detector yielding a value of $\approx$ 39 a.u. for the Hamamatsu APD and $\approx$153 a.u. for the Laser Components APD.

The Hamamatsu APD proved to perform better, with a SNR of 16 dB against the 13 dB calculated for the Laser Components APD, using the above mentioned measurement conditions. Therefore in the following the Hamamatsu APD was used.

3.1.2 Shack-Hartmann wavefront sensor

In previous work a low sensitivity of the SH-sensor CCD camera has been reported. It was concluded that the amount of collected electrons, resulting from the light returning from the retina, was below quantization noise[3] [12]. This prevented *in vivo* imaging.

To overcome this limitation several independent steps were taken. First of all, the maximum data integration time (DIT)[4] was increased by overwriting the value imposed by the Matlab ALPAO Core Engine (AO-loop software provided by the deformable mirror manufacturer) script using the PFRemote 2.34 software (software provided by the CCD camera manufacturer). With a DIT value higher than the previously imposed maximum of 24000 μs it was possible to ensure a resultant increase in the number of collected photons.

The former light power reaching the eye was around 200 μW, which when reflected back, due to losses within the system, reached the SH-sensor with not enough intensity for an efficient wavefront measurement. The solution was to couple more light from the light source, which provides an output power of about 20 mW. The input signal is coupled into a 90:10 coupler[5], which means that at the end of it, one fiber will have 10% of the input power while the other fiber will have 90% of the power. The use of the 90% fiber-port, rather than the 10% fiber-port, and polarization controller afterwards allowed an increase up to 400 μW at the eye while keeping it well below the 700 μW value regarded as safe. Note that the system is operated simultaneously with a line scanning laser ophthalmoscope which therefore limits the allowed maximum power of

[3]Quantization noise is the quantization error produced by an imperfect transformation of analogue signals to digital signals [56]

[4]The integration time of a CCD array is defined as the amount of time that charge is allowed to accumulate [56].

[5]Additional note: The system was initially intended to be used in combination with OCT.

the AO-SLO.

In addition, a pellicle that was used in the old setup configuration to split imaging light from the wavefront sensing light of the SH-sensor, described in Aschinger [12], was replaced by a 50/50 beam splitter (PBS). As a result, 50% of the light power is now being directed to the SH-sensor. This further improves the SNR of the SH-sensor.

A realignment of the whole AO-cSLO system was performed in order to eliminate a shadow that was visible at the top of the SH-sensor during model-eye measurements. This shadow originated from a partly beam blocking at one of the scanners. Finally, to avoid noise caused by stray light, a cover was built for the HS-sensor.

All together these procedures improved significantly the quality of the wave-front sensing and corresponding wavefront reconstruction, which in turn yielded not only a more accurate correction of the eye aberrations but also a more stable AO-loop.

Tests and Discussion

Taking all these modifications into account the number of electrons being collected can be re-calculated and compared with the quantization noise.

The power at the eye (P_{eye}) was modified to a value around 400 μW (without scanning). The amount of photons being back reflected from the retina (γ_{eye}) was assumed to be 1/10000 [46] and losses within the setup (γ_{setup}) were measured to be 0.5. With the PBS (γ_{PBS}) 50% of the light is diverted for wavefront measurement. The maximum possible DIT (t_{DIT}) can now be set to a value around 175 ms. The energy exposing the SH-sensor (E_s) can then be calculated as follows:

$$E_s = P_{eye} t_{DIT} \gamma_{eye} \gamma_{setup} \gamma_{PBS} \tag{3.2}$$

Using equation 3.2 an energy of 1.75×10^{-7} J was found. Afterwards, the energy per pixel can be calculated knowing that the number of spots N_{spots} in the SH-sensor is 1960 and that each of them extends to about 50 pixel N_{pix}. The division of the total amount of energy E_s by $N_{spots} \times N_{pix}$ yields an energy per pixel E_p of 1.79×10^{-12} J. This energy can be converted into the number of quantums per pixel after having calculated the energy of one quantum using

equation 3.3.

$$E_{840nm} = \frac{hc}{\lambda} = 2.4 \times 10^{-19} J \tag{3.3}$$

The number of quantums per pixel is therefore:

$$N_{quant} = \frac{E_p}{E_{840nm}} \approx 744048 \tag{3.4}$$

The sensor has a quantum efficiency η of 0.5 which means that the approximate number of collected electrons is ≈ 372024. The detector's full well capacity (FWC)[6] is 500000 e^- for 8 bits(256) per pixel. Thus, quantization noise can be calculated as follows [56]:

$$\delta_{ADC} = \frac{FWC}{256 \times \sqrt{12}} \approx 564e^- \tag{3.5}$$

The total number of collected electrons is now well above the quantization noise, being therefore possible to perform AO enhanced *in vivo* measurements.

Although the amount of light reaching the APD is now less, because the PBS redirects only 50% of the total backscattered beam power, this did not show to severely decrease the images' SNR.

3.2 AO-SLO system characterization

This section presents the assessment of the field of view (FOV) and resolution provided by the AO-cSLO instrument.

3.2.1 Field of view

To evaluate the field of view of the AO-cSLO a U.S Air Force 1951 resolution positive test target (RTT) from Melles Griot was used. It consists of a series of several bar patterns, which have a similar shape but different gradually smaller sizes.

An artificial-eye, consisting of a lens with a focal length of 30 mm and the RTT representing the retina, was built and images were recorded using the AO-SLO system (cf. Fig.3.2).

[6]Full well capacity is defined as the amount of charge a pixel can hold in routine operation [56].

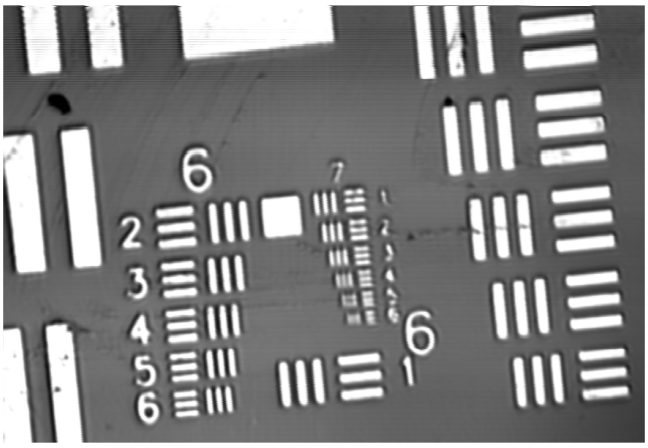

Figure 3.2: Resolution test target imaged with the AO-SLO system using the single-mode fiber configuration in the detection arm.

These images were processed (as described later on) and different patterns with known physical extension were selected. The size of each pattern was determined within the AO-SLO image by counting the number of pixels in order to determine the average pixel size (cf. Table 3.2).

Table 3.2: Calibration data for determining the field of view of the AO-SLO system.

	Average Pixel Size [μm]	Total number of pixels	FOV [μm]
x-direction	0.22	2537	558
y-direction	0.48	1096	570

Knowing that the focal length, f, of the lens used is 30 mm the scanning angle can be calculated as follows:

$$ScanningAngle(^\circ) = \arctan\left(\frac{FOV}{2 \times f}\right) \times \frac{360}{\pi} \tag{3.6}$$

Using equation 3.6 the resulting scanning area is $\sim 1^\circ \times 1^\circ$.

3.2.2 Resolution

Different approaches were used to evaluate the system resolution. A calculation of the lateral resolution provided by the AO-cSLO was first performed, after which an analysis based on acquired images was made.

Diffraction limit

Considering the equation for a diffraction-limited ophthalmoscope (2.10), an estimation of the lateral resolution of the AO-cSLO can be calculated as follows:

$$\delta = \frac{1.22 \times 0.840 \times f}{n \times 6900} \tag{3.7}$$

In the above equation the constant variables are the beam diameter at the eye (6.9 mm), which was measured as described in section 3.1, and the beam wavelength (840 nm).

Considering the optics of the eye, and assuming a refractive index (n) of 1.33 and a focal length (f) of the eye lens of 22.22 mm, a lateral resolution of 2.5 μm can be calculated [23].

For the artificial-eye the same calculation can be performed assuming f=30 mm and n=1, which yields a value of 4.46 μm for the lateral resolution.

In this calculation the improvement in the resolution resulting from the confocal configuration of the AO-SLO is not taken into account. Instead, a large pinhole (larger than one airy disk diameter) is assumed. The use of a small confocal pinhole combined with adaptive optics yields a resolution under the theoretical diffraction limit.

Resolution test target

The resolution limit of the AO-cSLO was evaluated using the single-mode fiber for light collection. The same artificial-eye, consisting of a 30 mm lens and the resolution test target, as introduced in section 3.2.1, was used.

The smallest element of the test target in the AO-cSLO image that can be seen defines the lateral resolution, that is typically expressed as the reciprocal of the spatial frequency of this element pattern. By observing the resulting image (cf. Fig. 3.2), one can conclude that the smallest resolved element is No. 4 group 7 for both x and y directions. This was further investigated by analysing the intensity profiles for the pixels along the red lines, marked as red lines in Figure 3.3, which confirmed that the system was able to resolve this element in both directions by showing three well defined peaks.

For this group the manufacturer of the RTT provides values of 181 line pairs per millimetre which corresponds to a lateral resolution of ~ 2.76 μm in both directions. Taking into account the improvement of resolution using a

small confocal pinhole this value corresponds to the theoretical limit.

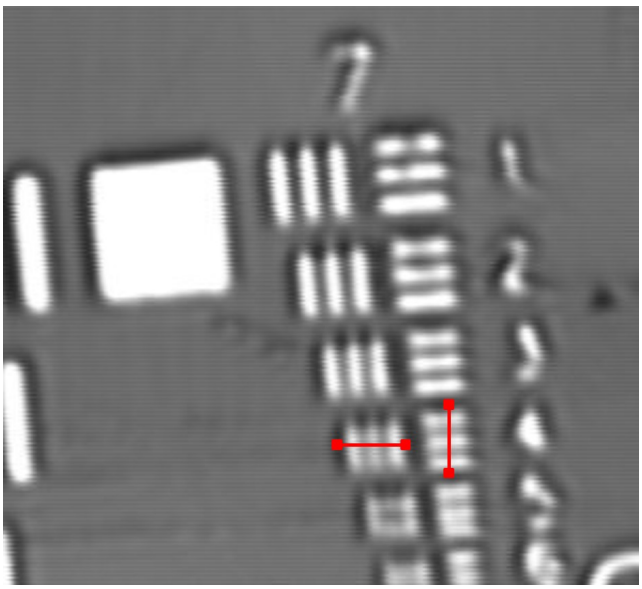

Figure 3.3: Zoomed region of interest of the resolution test target (cf. Fig.3.2) imaged with single-mode fiber configuration. The red lines mark the lines whose intensity profile was analysed in order to confirm the system resolution capabilities.

Assuming that the ratio between the resolution with the eye and with an artificial eye is approximately constant, one can estimate the resolution capabilities of the system when imaging the eye using the measured value with the RTT. As such, the estimated resolution is $\sim$1.55 μm. Note that this resolution is better than the diffraction limit without using a pinhole.

Measurements on a model eye: 2D autocorrelation function

In order to compare the different light collection alternatives explored in this thesis, images of a model-eye were recorded with the AO-SLO system and their ACF was calculated. As a sample, the RTT used before was replaced with a sheet of paper, which represents a scattering sample.

Mathematically, the autocorrelation function (ACF) of an image is the convolution of the image with itself and, like the original brightness function that defines the image, is a two-dimensional function. The ACF describes how well an image correlates with a shifted copy of itself, as a function of shift magnitude, retrieving information on the present periodic patterns and structures.

For an image I, of size M×N, it can be calculated as follows:

$$R_{xx}(a,b) = \sum_{x}^{M}\sum_{y}^{N} i(x,y) \times i(x-a, y-b), \tag{3.8}$$

where $R_{xx}(a,b)$ is the ACF, i(x,y) is the image intensity at position (x,y), and a and b represent the lag from the corresponding x and y position [57, 58].

We propose the use of the autocorrelation function as a tool for resolution assessment when comparing two different methods for acquiring the same image in the same experimental conditions.

The ACF has a peak in the centre, whose full width at half maximum (FWHM) will depend on the ability of the method to resolve small structures. A larger FWHM will therefore correspond to a method that provides images with lower resolution.

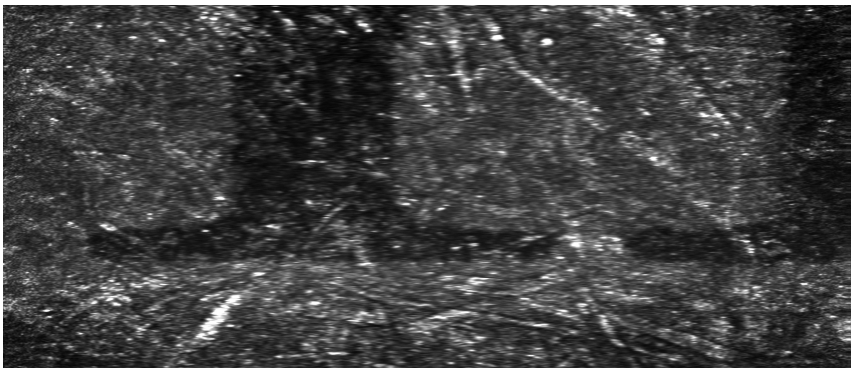

Figure 3.4: AO-cSLO image of the model-eye acquired with the single-mode fiber.

Figure 3.4 shows the model eye AO-cSLO image acquired when using the single-mode fiber as confocal gating in the detection arm.

Since the AO-cSLO images are 2569 × 1096 its 2D ACF will be of size $(2 \times 2569 - 1) \times (2 \times 1096 - 1)$, reaching its maximum in the centre.

The left plot on Figure 3.5 is a three-dimensional normalized representation of the ACF with the same size of the original image. The right plot depicts a zoomed two-dimensional representation of the same function.

For further assessment of the FWHM of the ACF lateral and axial profiles, the central line in both x and y directions was selected.

Using the single-mode fiber for light collection, it was found a $\text{FWHM}_x = 37$ pixel and $\text{FWHM}_y = 15$ pixel for the plots depicted in 3.6a and 3.6b respec-

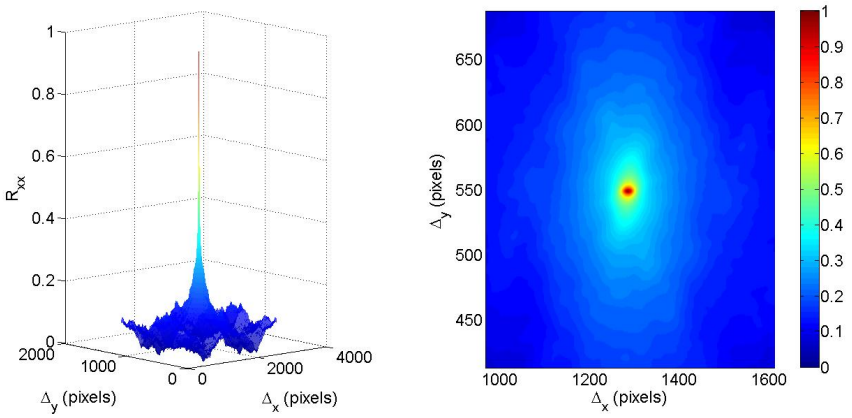

Figure 3.5: 3D and 2D (zoomed) representation of the autocorrelation function of the AO-cSLO image of the model eye (cf. 3.4), acquired with the single-mode-fiber.

tively.

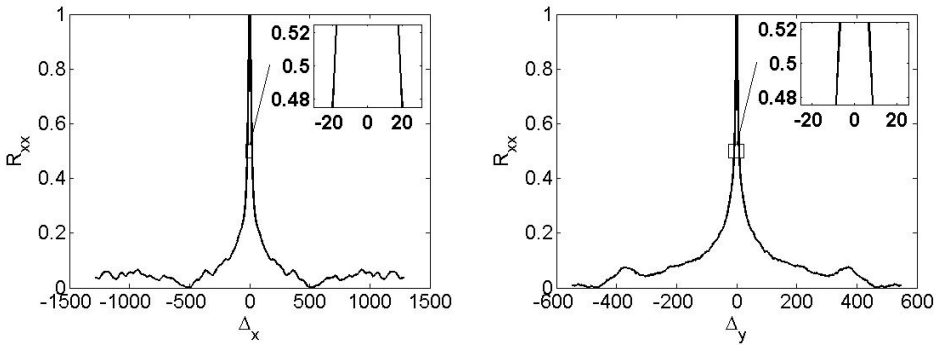

(a) (b)

Figure 3.6: Intensity plots of the lateral ACF peaks, in both x and y directions.

Knowing that, when imaging an object with a lens with f = 30 mm, one pixel corresponds to 0.22 μm in the x direction and 0.48 μm in the y direction (cf. Table 3.2), the FWHM can also be expressed in μm as $\text{FWHM}_x = 8.14$ μm and $\text{FWHM}_y = 7.2$ μm. Because of the auto correlation these values are twice the FWHM of the point spread function, which corresponds to a lateral image resolution of 4 μm and 3.5 μm, respectively. The resolution obtained in scattering media is therefore slightly lower than that obtained with the resolution test target.

3.3 Detection Optics Alternatives

3.3.1 Description

The light collection of this AO-SLO system is done using a single-mode fiber instead of a standard pinhole configuration. In this thesis work the implementation and further assessment of two different confocal pinhole detection configurations was tested. Image resolution and SNR were used as metrics to compare the images resulting from each approach. Furthermore, the possibility of imaging smaller retinal vessels by collecting scattered light using a multi-mode fiber for light collection was also tested.

A convenient way to define the size of the pinhole/aperture is in coordinates normalized to the diffraction-limited point spread function, or Airy disk (AU[7]). One reason for choosing this scale is that a comparison between instruments is simplified.

To calculate the Airy disk diameter size for each of the detection experimental designs the following formula was used:

$$\emptyset_{AiryDisk} = \frac{1.22 \times \lambda \times f_1}{r_{beam}} \tag{3.9}$$

Where $\lambda = 840$ nm, f_1 is the focal length of the collimator lens and $r_{beam} = 4000$ μm is the beam radius ($1/e^2$ of the maximum intensity) at this location of the setup.

Table 3.3 summarizes the Airy disk size and the aperture size for each of the detection optics configurations previously mentioned.

Table 3.3: Characteristics of the different detection optics configurations. PC-Pinhole Configuration.

	PC A	PC B	Single-mode fiber	Multimode fiber
Aperture size (μm)	30	30	5.6	62.5
f1 (mm)	20	50	40	40
Airy Disk Diameter (μm)	12.85	5.14	10.28	10.28
Aperture size (AU)	5.84	2.33	0.54	6.08

[7]Airy Disk Units

3.3.2 Pinhole: Implementation

Figure 3.7 shows a scheme of the detection configuration using a pinhole, which consists of one mirror, two achromatic lenses and one pinhole.

The alignment of the detection telescope with the pinhole starts by aligning the mirror (M). In order to align this mirror a second mirror is placed at the location of the eye, to maximize the light intensity being reflected at this location so that the beam position can be monitored using an infrared sensor card.

First, the height of mirror M has to be set so that the beam coming from the PBS (cf. Figure 3.1 which shows the whole AO-SLO setup) hits its centre. In addition the mirror angle has to be 45°in respect to the incoming light beam. To confirm if there is any deviation from the ideal position, either in height or angle, the easiest way is to observe the position of the light beam over a long distance with an infrared sensor card. The lateral position and height of the light beam should stay constant over the distance.

In a next step, the first lens (f_1) is inserted so that the beam transverses the lens centrally. The pinhole must then be placed at the focal distance of the lens. To ensure a precise alignment the pinhole is placed in a pinhole-mount that can be adjusted with two micrometer screws, that allow to change the height and lateral displacement of the pinhole. For an easier alignment the lens holder and the pinhole mount were connected, to ensure they were roughly centrally aligned with each other.

After traversing the pinhole the beam is focused into the small active area of the APD $Ø_{APD}$=1 mm with an (30 mm focal length) achromatic lens (cf. Figure 3.7).

Since the pinhole and the detector are located each at twice the focal length of the lens, the pinhole will be imaged onto the detector with a magnification of one.

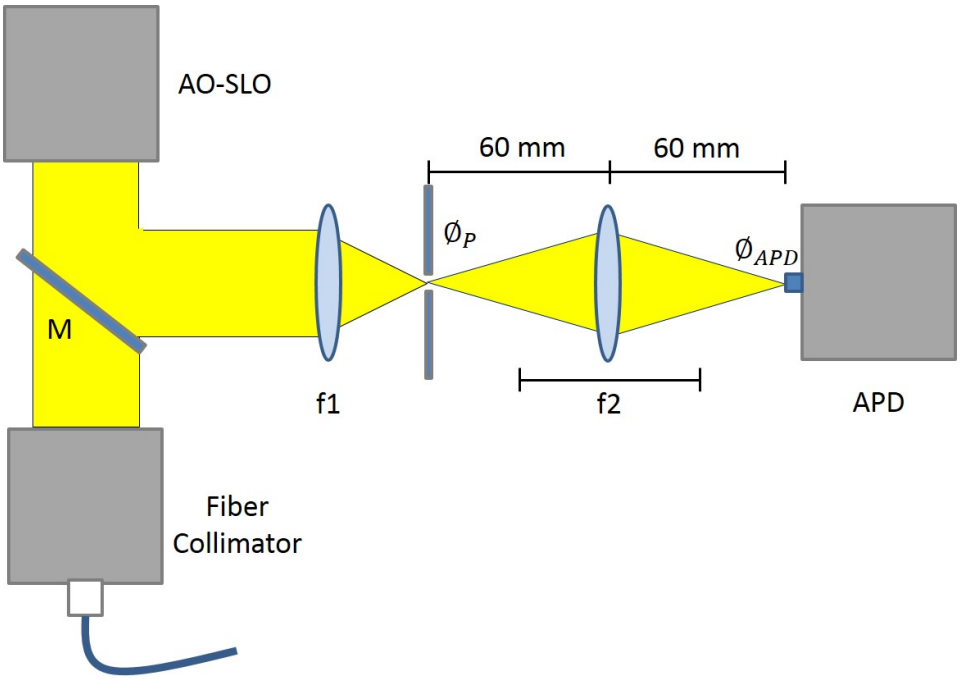

Figure 3.7: Scheme of the pinhole detection configuration. M: Mirror, f_1: Lens 1, f_2: Lens 2, APD: Avalanche photo diode, $\emptyset_P$: Pinhole diameter, $\emptyset_{APD}$: Diameter of the light sensitive area of the APD, AO-SLO: Adaptive Optics Scanning Laser Ophthalmoscope.

In order to check the losses introduced by both confocal detection configurations (pinhole and single-mode fiber respectively), the light power was measured with a powermeter (Thorlabs PM100D) before and after the pinhole in the configuration B. The emerging power from the 30 μm pinhole corresponded to 80% of the input light power (20% loss). A power loss of around 50% was measured for the SM-fiber. It is therefore expected that a higher signal to noise ratio can achieved when using the pinhole as confocal aperture instead of the SM-fiber.

3.3.3 Pinhole: Evaluation

In this subsection the evaluation of the resolution and SNR provided by the pinhole detection configuration is presented and discussed.

A 30 μm pinhole size was used along with two different designs, considering the available lenses for the collimator, which had a focal length of 20 mm and 50 mm (described in 3.3), corresponded to $\approx$ 6 AU and $\approx$ 2 AU respectively.

The assessment of the differences between the SMF detection and the pinhole detection was based on the resolution and SNR provided by both approaches.

Firstly, in order to evaluate the resolution the same resolution test target previously referred to was used. Since only the pinhole configuration B (aperture size equivalent to 2 AU) yielded images with a resolution comparable with the one provided by the SMF a comparison between both is illustrated here (cf. Fig. 3.8).

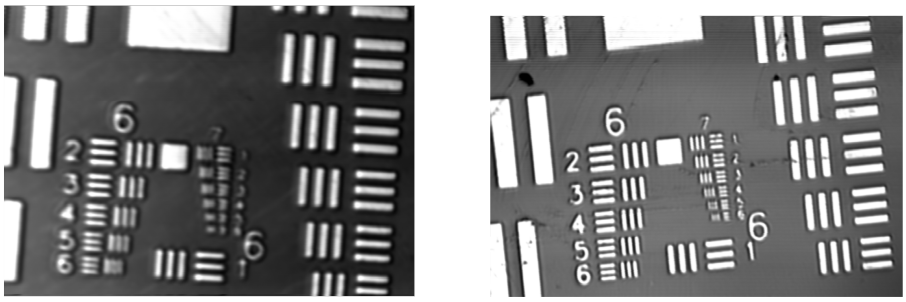

(a) (b)

Figure 3.8: Resolution test target imaged with (a) pinhole configuration B (aperture size equivalent to $\sim$2 AU) and (b) single-mode fiber configuration (aperture size equivalent to $\sim$0.5 AU).

It can be concluded from Figure 3.8a that the smallest resolvable element in the x direction is No. 5 of group 6 and in the y direction is No. 6 of group 6, which can be calculated to correspond to a resolution of 4.90 μm and 4.39 μm respectively.

In order to assess the resolution capabilities of the different confocal detection configurations in a scattering sample, images of a model eye (with a sheet of paper corresponding to the retina) were recorded and the autocorrelation function of the obtained images was calculated. The computation of the ACF

and its further analysis was done as previously described in section 3.2.2.

The calculated FWHM values for each of the configurations are summarized in table 3.4.

Table 3.4: Measured lateral FWHM for the ACF of the model-eye images acquired with the single-mode fiber, A and B confocal pinhole configurations.

	$FWHM_x$ (pixel)	$FWHM_y$ (pixel)	$FWHM_x$ (μm)	$FWHM_y$ (μm)
SMF	37	15	8.14	7.2
PC A	89	38	19.58	18.24
PC B	42	20	9.24	9.6

Note that the lateral resolution calculated via the auto-correlation corresponds to half the values given in the table which results in a lateral resolution of 3.6 μm for the SMF configuration, 9 μm for PC A and 4.8 μm for the PC B configuration, respectively. The numbers show a higher resolution provided by the single-mode fiber configuration, as expected because of the smaller confocal size ($\sim$0.5 AU vs. $\sim$6 AU and $\sim$2 AU). In this thesis only two different pinhole configurations were tested. However, it should be noted that the confocal pinhole is widely used in groups doing similar adaptive optics SLO research [9, 14].

The SNR of the model-eye images obtained when using the pinhole design B (PC B) and the SMF were measured for comparison. The precise values were 21.70 dB and 21.53 dB. The SNR for the image obtained with the pinhole was only slightly higher than the one measured with the fiber. This result might be explained with a non-perfect alignment of the detection system with the pinhole, such that the pinhole was not exactly located at the focal plane of the first lens (cf. Fig 3.7).

3.3.4 Multimode fiber: Implementation

With the purpose to mimic the performance of a large pinhole, the single-mode fiber was replaced by a multimode fiber.

The optics design when using fibers includes a detection collimator to couple light efficiently. Each collimator consists of two cylinders that can be

telescoped. One cylinder holds the lens (focal length is 30 mm), while the other holds the end tip of the fiber, as illustrated in Figure 3.9.

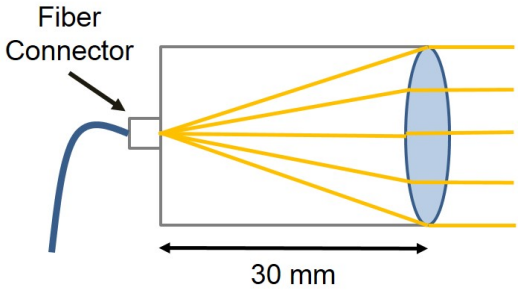

Figure 3.9: Beam geometry in the case of a well adjusted collimator.

This collimator is mounted on a two-axis stage, allowing its height to be adapted as well as its position perpendicular to the light propagation direction.

The possibility to adjust tip and tilt of the fiber is also provided, as shown in the scheme 3.10. This configuration enables to maximize the light power that is coupled into the fiber.

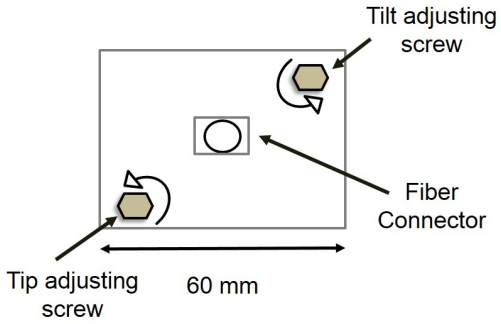

Figure 3.10: Scheme of the fiber holder mounted at the back of the collimator stage. The screws can be rotated in both directions, allowing fine adjustment of tip/tilt.

Multimode fibers have a larger fiber core size and corresponding numerical aperture (NA), which makes the alignment procedure straightforward. Moreover, the larger NA makes them well suited for collecting multiple scattered light. The numerical aperture is defined in equation 3.10, being the full acceptance angle 2α.

$$NA = \sin(\alpha) \tag{3.10}$$

In this thesis a multimode fiber from OZ optics with an operating wavelength range of 400 nm - 2000 nm was connected to the collimator holder. The

NA value calculated in the data sheet for this fiber was 0.275, yielding a full acceptance angle of about 31.92°. This angle is considerably larger compared with the single-mode fiber full acceptance angle of 14.94°. The equivalent pinhole size of the multimode fiber was calculated to be 6.08 AU.

The mount holding the fiber is equipped with two fine-adjustment screws with 0.25 mm pitch (cf. Figure 3.10). The effect of changing the fiber tilt for a value that corresponds to a 45° rotation of the screw was studied.

Knowing the pitch value the corresponding distance to a 45° rotation can be calculated as $\frac{1}{4}0.25 = 0.0625$ mm. Since the mount lateral size accounts for 60 mm, the total tilt angle can be calculated as follows.

$$\theta_{tilt} = \arctan \frac{0.0625}{30} = 0.12^{\circ} \tag{3.11}$$

3.4 The Line-Scanning Laser Ophthalmoscope

3.4.1 Description

A line-scanning laser ophthalmoscope (LSLO) has been formerly built by P.Vetschera [11]. In this work the main objective was to implement the LSLO into the existing AO-cSLO developed by G.Aschinger [12]. The LSLO aims to provide a larger FOV image for global orientation of the small FOV image recorded by the AO-SLO and the possibility to select specific regions of interest for high resolution imaging. For these reasons, the support of the LSLO overview image allows a less time consuming alignment of the eye.

This section's first part describes the LSLO experimental setup that was implemented before this master thesis work followed by a description of the modifications and improvements performed within this thesis.

The design scheme of the previous implemented LSLO in the horizontal plane is depicted in Figure 3.11. Note that the beam propagation in the vertical plane is different because the symmetry is broken by the cylindrical lens which is placed right after the entrance collimator.

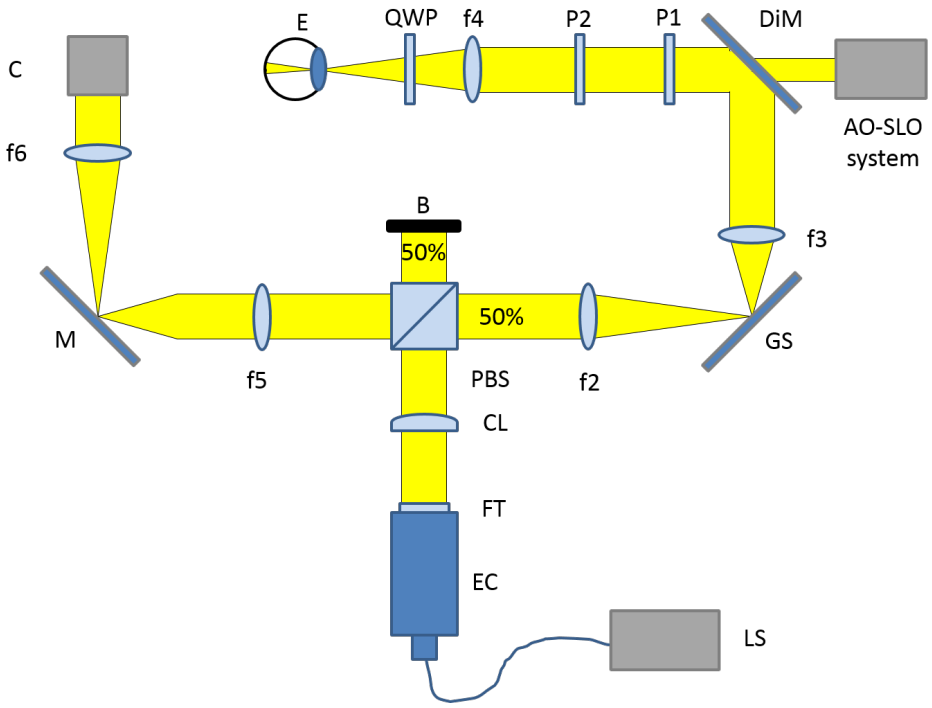

Figure 3.11: Scheme of the previous experimental setup of the LSLO in the horizontal plane. LS: Light source, EC: Entrance collimator, FT: Neutral density filter, PBS: Polarizing beam splitter, B: Beamstop, CL: Cylindrical lens, $f_2 - f_6$: achromatic lenses, GS: Galvo Scanner, DiM: Dichroic mirror, P1-P2: Prisms, QWP: Quarter wave plate, E: Eye, M: Mirror, C: Line-scan camera. Adapted from [11].

The LSLO is operated at a central wavelength of 1050 nm with a spectral width of 65 nm, whose maximum allowed power at the eye according to the safety standards accounts for 8.1 mW. This value was calculated assuming that the AO-cSLO is measuring simultaneously with a power that can go up to 0.7 mW, as stated in section 3.1.

No aberrations are corrected for the LSLO beam as a higher resolution would not provide any extra benefit considering the main purpose of this LSLO setup. Both beams, the 840 nm and the 1050 nm, are combined through a dichroic mirror (DiM)(cf. Figure 3.11).

In contrast to a typical SLO, where a laser spot is moved over the retina, in the case of a LSLO a laser line is projected to the retina. Therefore only one scanner is needed and a line-scan camera is used to detect backscattered light from the retina.

For raster scanning a galvo scanner is used to change the position of the illuminating horizontal line in the orthogonal direction (y direction). The

synchronization with the AO-cSLO is established through the clock master of the resonant scanner.

A polarizing beam splitter (PBS) was introduced in the LSLO in order to avoid back-reflections from the lenses within the setup, using the same principle as in the AO-cSLO (described in section 3.1).

The exposure time of the LSLO camera is set to 125.2 μs which yields 550 line scans at a frame rate of 7 Hz. The number of desired lines scanned by the galvo scanner can be changed using the program ScannerControllerfor2.vi which will be described in section 4.3.

The FOV provided by the LSLO corresponds to a 7.20° scanning angle in the x-direction and 5.16° in the y-direction, with a corresponding lateral resolution of 55 μm by 44 μm in the x and y directions respectively. More on this system design was described in detail elsewhere [11].

3.4.2 Modifications and Improvements

The LSLO system was successfully working as a stand-alone system at the time this thesis work began. However, the combined operation with the AO-cSLO was not optimal because light from the LSLO influenced the SH-wavefront measurements.

As it can be seen in Figure 3.12 , the dichroic mirror transmission for wavelengths longer than 1000 nm is not equal to zero, which was the reason why some of the light coming from the LSLO was being transmitted into the AO-cSLO system. This influence had been overseen in the initial system design, therefore the detected polarization state of the SH-sensor and the emission polarization state of the LSLO were, merely by coincidence, identical which did not improve the situation. Therefore part of the 1050 nm light beam has been detected by the SH-sensor which influenced the wavefront measurement and degraded simultaneous LSLO and AO-SLO measurements.

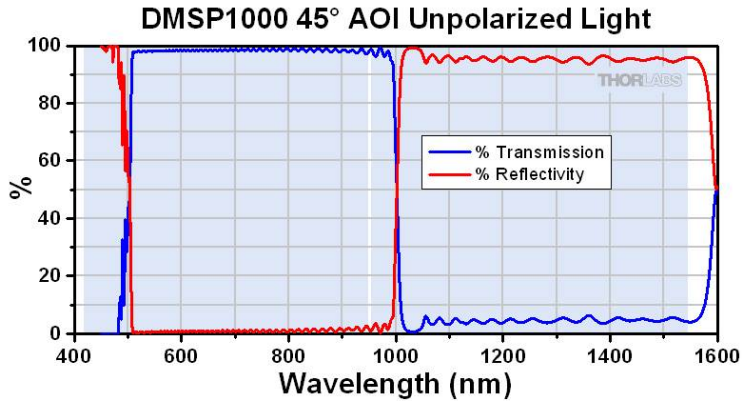

Figure 3.12: Transmission and reflectivity spectra for the DiM. Adapted from [11].

Apart from this problem, undesirable corneal reflections were being detected in the LSLO camera which compromised the quality of the overview image of the retina.

To address both situations the configuration of the LSLO was modified (cf. Figure 3.13).

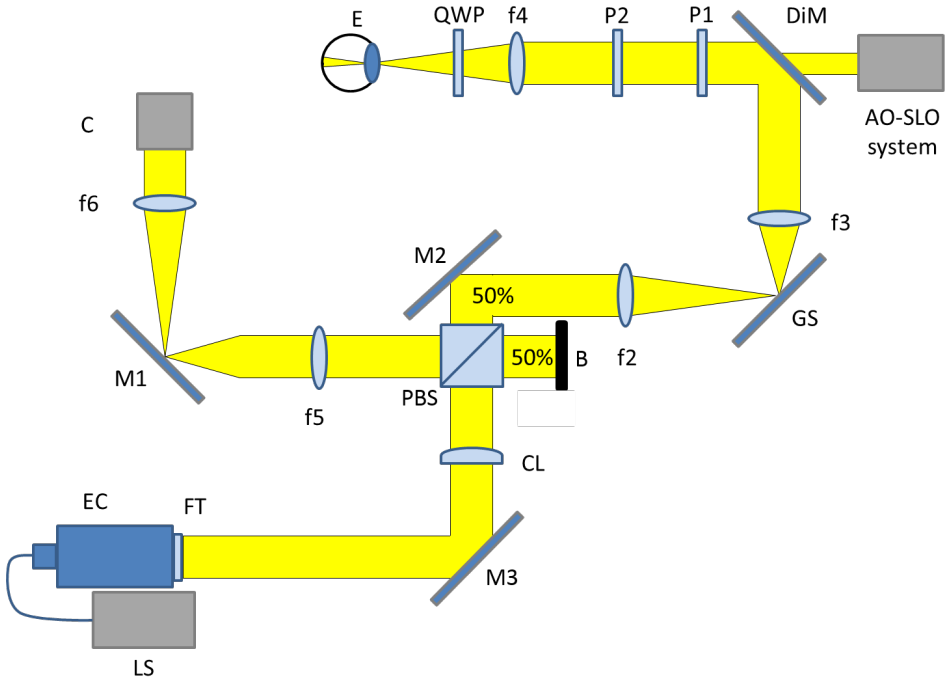

Figure 3.13: Scheme of the redesigned experimental setup of the LSLO in the horizontal plane. LS: Light source, EC: Entrance collimator, FT: Neutral density filter, PBS: Polarizing beam splitter, B: Beamstop, CL: Cylindrical lens, $f_2 - f_6$: achromatic lenses, GS: Galvo Scanner, DiM: Dichroic mirror, P1-P2: Prisms, QWP: Quarter wave plate, E: Eye, M1-M3: Mirror, C: Line-scan camera.

By changing the beam propagation path through the PBS the polarization state of the LSLO incident on the AO-SLO system was changed to a state orthogonal to the one that was being used before. With this modified configuration the influence of the 1050 nm light beam on the SH-sensor could be eliminated.

By intentionally creating an offset between the illumination and the detection path of the light corneal reflections are suppressed. Instead of going centrally through the pupil, the illuminating beam has now an offset which avoids the detection of the corneal reflex. However, sufficient backscattered light from the retina is still detected.

Chapter 4

Adaptive Optics SLO: Software

This chapter provides an insight into the software used not only to control the AO-cSLO loop components but also for image acquisition and offline data processing.

Both the deformable mirror and SH-sensor were provided by ALPAO which also supplies the ALPAO Core Engine (ACE), that can be further customized to the particular needs of the customers. The ACE is implemented in object oriented Matlab code enabling the user to derive classes from supplied classes and overwrite different class methods [40]. Briefly, this software allows monitoring of the SH-sensor's CCD camera raw image, monitoring of the reconstructed wavefront and RMS value and control of the DM.

However, the software's base modules can not be changed and are not designed for ophthalmic applications. Due to this it was not possible before this thesis to record images of the living retina with the AO-cSLO setup with satisfactory quality. Within this thesis several software adaptations in the AO-loop related software have been performed to enable retinal imaging as presented in the first section of this chapter. Each sub-section starts by briefly describing the possibilities provided by the original AO-loop software and the problems associated with these parts, followed by a description of the implemented solutions to each of these problems.

The following section describes the additional software features that were implemented to improve the control of the deformable mirror.

The last section explains in more detail the implemented image acquisition software and post-processing steps.

4.1 Adaptive Optics Loop

To initialize the DM and the wavefront sensor the userStartup.m (see A.1) Matlab script must be executed. In this script, besides initializing both the DM and the SH-sensor, a circular mask which is used for spot detection in the SH-sensor is defined. The user can also decide whether to set the wavefront reconstruction to modal or zonal.

The class that controls the SH-sensor and retrieves the spots position for posterior reconstruction was overwritten (see A.2) which is further explained in the next sub-section.

After setting the above mentioned definitions the AO-loop control is performed using a Labview interface, where the user can see in real time the raw image from the SH-sensor as well as the wavefront reconstruction and respective RMS value. Apart from that, the Labview interface enables recording of the reference raw image for the SH-sensor to be subtracted in Matlab. In addition a new feature was implemented that allows the recording of the raw SH-sensor image, the corresponding wavefront reconstruction and the RMS-wavefront error. This enabled monitoring of the AO-loop efficiency and residual wavefront error for both the model eye and *in vivo* measurements.

4.1.1 Loop Stability

One major problem of the original adaptive optics loop software was an instability of the loop in the case of *in vivo* measurements, which turned out to be mostly due to an inefficient computation of the spots' center of gravity (COG) in the SH-sensor.

The center of gravity computation of each spot of the SH-sensor is a key process for the adaptive optics loop. To eliminate noise from the spot detection a threshold level is predefined. Pixels that show values below this threshold are set to zero and are excluded from the centroid calculation. In addition, centroids are only calculated within a circular mask that corresponds to the maximum pupil size. Unfortunately, this threshold is implement as a fixed parameter in the software and can not be changed.

While there is sufficient signal in the case of the model-eye to detect every centroid within the pupil mask, only few were detected in the case of *in vivo* measurements (cf. Fig 4.1a). Due to the low signal to noise ratio, many of the

detected COGs are erroneous. The software automatically extrapolates the wavefront based on the found centroids over the full mask and the AO-loop tries to correct for this erroneous wavefront. This leads to arbitrary shapes of the DM, a completely blurred AO-SLO image and finally to a saturation of the elements of the DM, stopping the AO-loop since the elements are frozen and can not be moved.

In order to overcome this problem, the class for the SH-sensor was replaced (see A.2). The new overwritten class allows for a subtraction of a reference image to the raw image of the SH-sensor, in order to eliminate of any external undesirable influences such as reflections within the system or stray light that can be detected by the sensor. In this new class it is now possible to set a gain. Since the threshold could not be changed, this gain allowed an amplification of the signal such that the majority of the signal pixels lay above the threshold, allowing a correct centroid calculation.

This gain was set as 2.5, which proved to be a value that enhanced the COG calculation in all situations, regardless of the type of measurement being performed (*in vivo*/model eye). The enhancement in the COG computation after this software change is depicted in Figures 4.1b and 4.1c. In this script, tip and tilt are also excluded from wavefront reconstruction and correction.

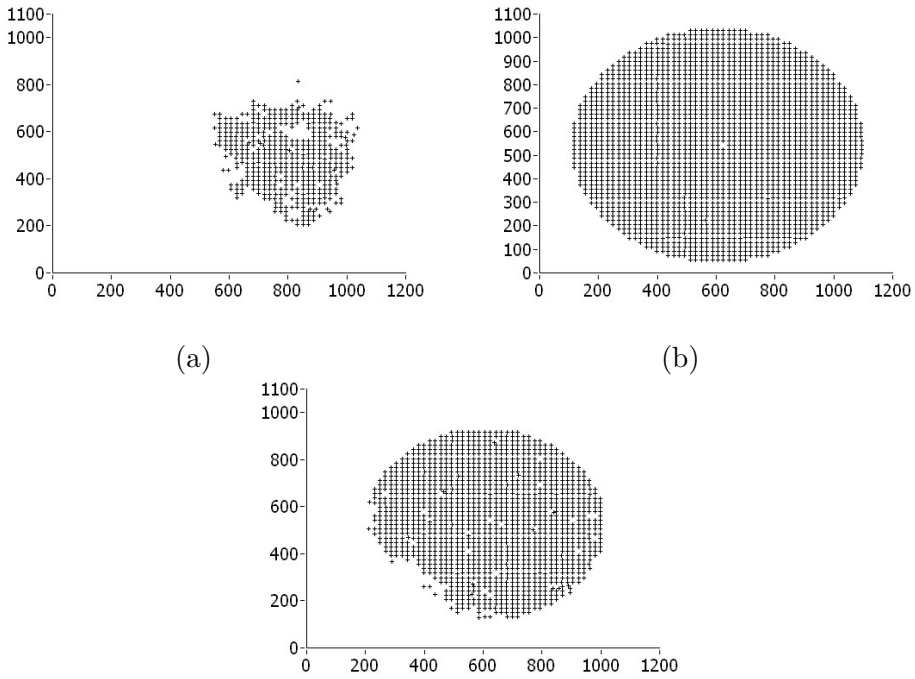

Figure 4.1: Spots computation in the SH-sensor in three different situations. (a) illustrates the few spots being calculated before applying the gain correction during an *in vivo* measurement. (b) and (c) show the enhancement in the number of spots being calculated after the software changes when imaging the model-eye and during an *in vivo* measurement respectively.

As stated before, the first step to initialize the AO-loop settings is to execute the userStartup.m script (cf. Appendix A.1). In this script it is possible to choose the type of wavefront reconstruction algorithm and to define the mask size, which defines the area of the SH-sensor where data will be taken into account for the wavefront reconstruction. More details on this mask are explained in the following.

Originally, the reconstruction of the wavefront was based on the modal reconstruction algorithm (further explained in the background section 2.2.1), which extrapolates values in regions of the full mask even in the case where the sensor does not find centroids. For instance, when performing *in vivo* measurements the eye pupil varies between individuals, which means that in some cases (where the pupil is smaller) not all lenslets within the mask are illuminated. Hence, the wavefront is extrapolated to provide values within the full mask. This extrapolation is sensitive to errors and causes wrong displacement of the corresponding elements of the DM. These lead to an incorrect wavefront

correction, image blurring and finally to an unstable AO-loop which will result in saturated DM elements and a stopping of the AO-loop. To avoid this error there are two possibilities.

The first possible approach is changing the reconstruction algorithm from "modal" to "zonal". The zonal reconstruction is based on an iterative process, whose tolerable error can be changed. Figure 4.2 illustrates the difference between zonal and modal reconstruction for a pupil that is smaller than the mask.

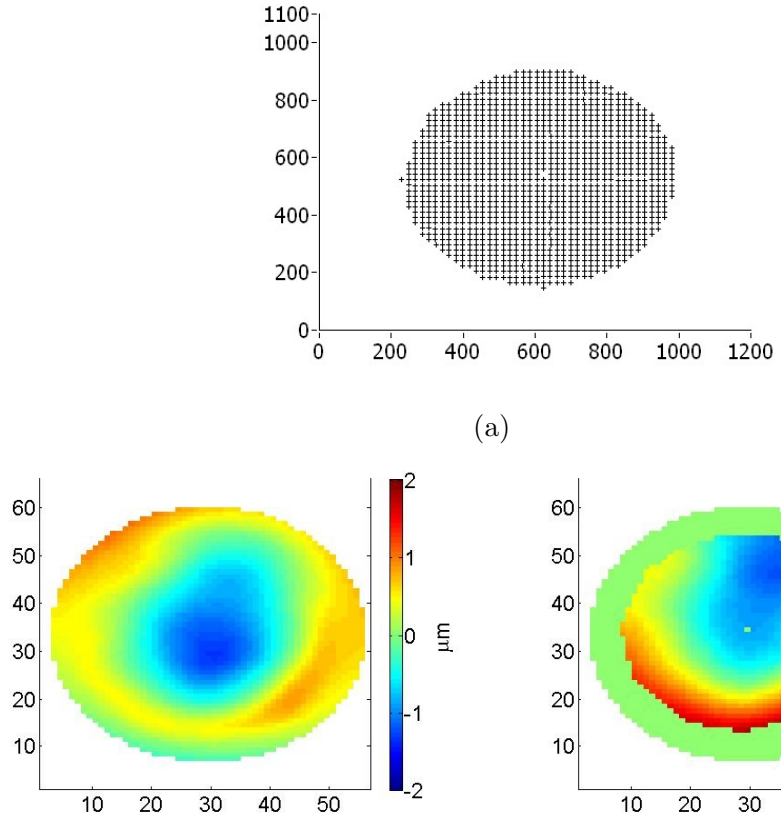

(a)

(b) Modal algorithm.

(c) Zonal algorithm.

Figure 4.2: Wavefront measurements in the model eye in a case where the pupil of the model-eye is smaller than the predefined mask. (a) Centroids that have been found in the HS sensor image. Wavefront reconstruction based on the modal (b) and the zonal (c) algorithm. Severe differences in the wavefront can be observed between zonal and modal reconstruction.

The second solution is the definition of a new mask corresponding to the size of the pupil of the eye.

Only the data retrieved by the lenslets that lie within this mask will be taken into account for the centroid computation and wavefront reconstruction. However, in the current software this mask can only be changed before the

starting of the program which generally limits this option. Figure 4.3 shows three masks that were implemented in order to account for a variable pupil size. The largest mask corresponds to the default mask, whose size covers the maximum pupil size which corresponds to an 8 mm pupil diameter.

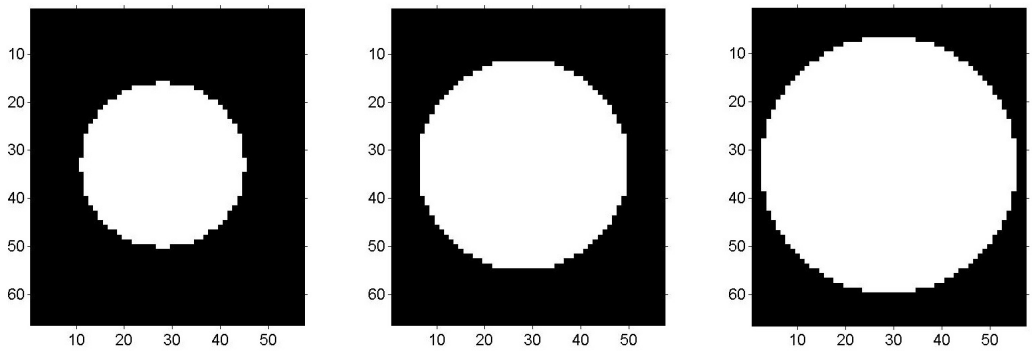

Figure 4.3: Different mask sizes used for the wavefront reconstruction. The default size corresponds to the largest mask illustrated.

This mask can only be used for subjects with fully dilated pupil. With the purpose of having a mask whose size fits the pupil size of the subject being imaged without dilation, two other smaller masks were designed.

Figure 4.4a shows measurements of a subject with small pupil size. Using the small mask, both reconstruction algorithms (zonal and modal) can be used.

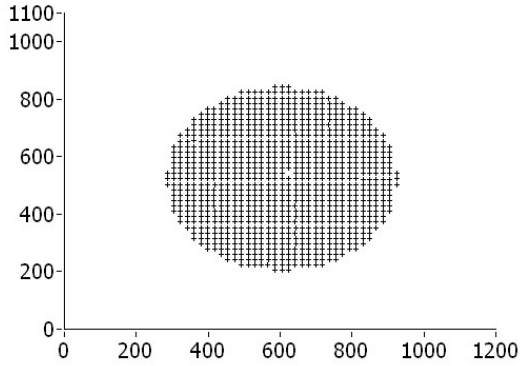

(a) COGs being calculated.

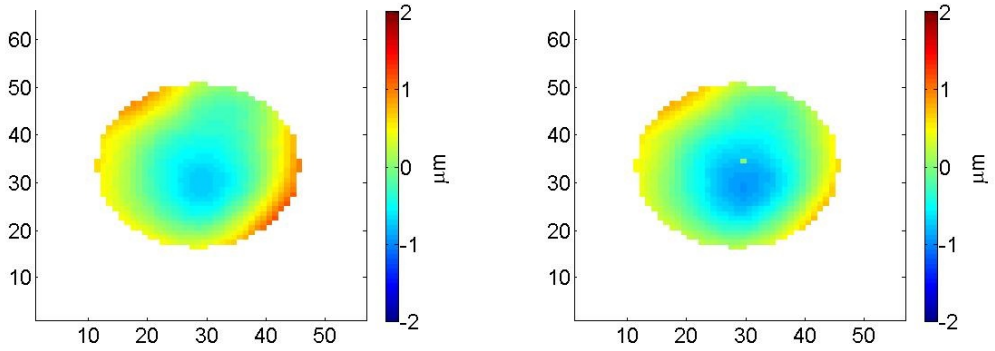

(b) (c)

Figure 4.4: Wavefront measurements in the model eye using a smaller mask size. (a) centroids found within the mask. Wavefront reconstruction based on the modal (b) and the zonal (c) algorithm. Both reconstruction algorithms yield similar results.

In order to use the different mask sizes for AO-control it is necessary to record corresponding influence matrices, containing all the individual influence functions for the DM actuators (as explained in 2.2.2). The influence matrix contains the information how each of the actuators of the DM influences the wavefront. The influence matrix has n columns (number of actuators) and k rows (number of micro lenses of the lenslet array within the defined pupil mask), as represented in equation 4.1 [40].

$$IM = \begin{bmatrix} a_{11} & \cdots & a_{1n} \\ \vdots & \ddots & \vdots \\ a_{k1} & \cdots & a_{kn} \end{bmatrix} \tag{4.1}$$

Figure 4.5 shows the wavefront shape detected at the SH-sensor when activating each of the 97 actuators independently. For the smaller masks there will

be no influence from the outer actuators and the corresponding wavefronts are set to zero.
The command matrix that drives the deformable mirror actuators is computed from the influence matrix.

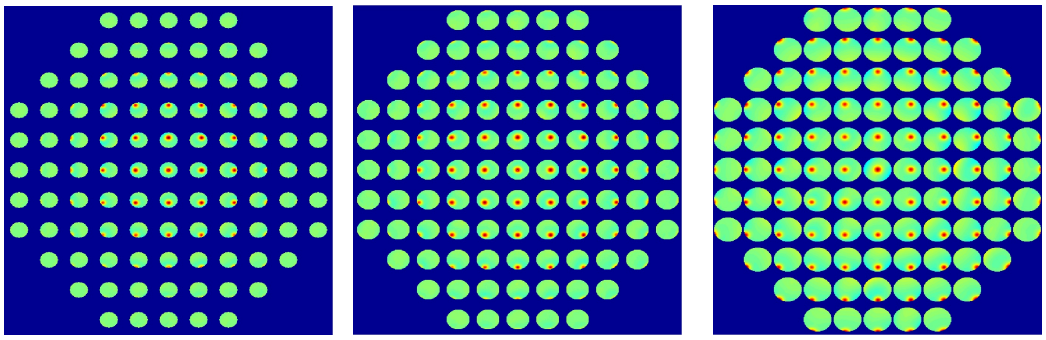

(a) (b) (c)

Figure 4.5: Influence function of the 97 actuators for three different mask sizes: (a) Small Mask (diameter = 5 mm), (b) Medium Size Mask (diameter = 6.5 mm) and (c) Full mask (diameter = 8 mm).

In order to automatically adjust the mask size to the pupil size at the beginning of every measurement a new Matlab routine was created. This script computes a new mask by determining the area where centroids are found by the algorithm (cf. Appendix A.3).

To calculate the mask using the SH-sensor data, the sensor has to be set to an online state. After that, according to the software provider, the SH-sensor has to be set to an offline state to apply this new calculated mask. However, it turns out that every time the SH-sensor is turned off it cannot be set to an online state again without reinitializing Matlab, which makes the whole process cumbersome and unsuitable for *in vivo* measurements. For this reason this script was not implemented during the measurements.

Even after overcoming this problem, it would be necessary to develop a new script to automatically compute the influence matrix corresponding to the new mask.

4.2 Deformable Mirror

4.2.1 Bias Vector

In the beginning of any measurement the voltage value being applied to each actuator of the DM is zero, therefore the shape of the mirror surface is com-

pletely arbitrary. A flat mirror shape would be the ideal initial condition prior to the start of the AO-loop. However, this random shape will cause additional computational time and stroke of the DM to correct the real eye aberrations. In order to have the mirror in a flat position when initializing the AO-loop a predefined actuator command vector is set as biasVector (see A.1). To record the pattern of the DM that corresponds approximately to a flat surface a highly reflective surface was positioned at the location of the eye and the AO-loop was turned on. The corresponding voltage values of each actuator were saved and are automatically applied to the DM every time the loop starts to run.

4.2.2 Additional Defocus

In the healthy eye the main contribution to the SH-sensor signal comes from the photoreceptor layer. Therefore, this layer will be imaged sharply when the AO-loop is turned on. In order to image other layers (e.g. anterior layers such as the nerve fibre layer) an additional defocus has to be introduced to the beam. In order to do so the following steps can be used:

- **Close the AO-loop and let it stabilize**. The loop is stable when the wavefront RMS reaches and keeps a minimum value.
- **Open the loop.** This will freeze the mirror and the actuators remain in their current position.
- **Save the actual voltages**. The voltages being applied to the elements of the DM are saved as an offset;
- **Apply defocus**. The defocus is applied on top of the offset. The control software uses the influence matrix to determine the voltage that is applied to each actuator to produce the desired defocus.

All these steps can be easily done in the LabView interface specially designed for the DM, aceguiMirror.vi.

4.3 Image Acquisition and Processing

Custom software was developed in Labview (National Instruments, Austin, Texas) for the image acquisition and for the several offline processing steps, illustrated in Figure 4.6.

The AO-cSLO records an image frame consisting of 2569×1096 pixel in $\approx$ 69 ms, yielding a frame rate of $\approx$ 14.6 frames per second (FPS).

The amplitude and number of lines scanned by the Galvo-scanner can be set in the program ScannerControllerfor2.vi whereas the amplitude of the resonant scanner is set by adjusting a potentiometer.

The resonant scanner moves the beam over the sample and image data is recorded during both scanning directions (forward and backward). As a consequence of the sinusoidal waveform of the resonant scanner, the images need to be dewarped. However, in order to obtain a full image, every second row (backward scan) has to be inverted and a residual displacement has to be corrected. Fig 4.6 shows the two images resulting from the forward and backward scan and the interwoven image.

In a next step the recorded images have to be registered to each other in order to allow for image averaging.

As stated in section 2.1.1, when imaging living human eyes, normal involuntary eye motion, even during fixation, causes the imaging raster to move continually across the retina. Eye motion consists of drift, tremor and saccades. Saccades are very fast and result in heavily distorted image frames which have to be excluded from further analysis. Although slower, drift and tremor are fast enough to cause not only displacements between the frames but also in-frame distortions. Therefore the image registration software includes two steps.

First of all, a reference frame that does not show motion artifacts is selected from the recorded images. In a first step displacements between the reference frame and the other recorded frames is determined using cross correlation between them. This information is used to correct for the lateral displacement. Since intra-frame distortion exist in all image frames, each frame is in a second step divided into subframes (stripes) along the slow scanning axis (each consisting of 40 horizontal lines). Cross correlation was then calculated between each stripe and the reference frame and the corresponding residual displacement of a stripe was determined and corrected. With this, such intra-frame distortion within the data set was eliminated. After that the cross correlation between the frames was calculated again and only frames that showed a high correlation with the reference frame were used for averaging.

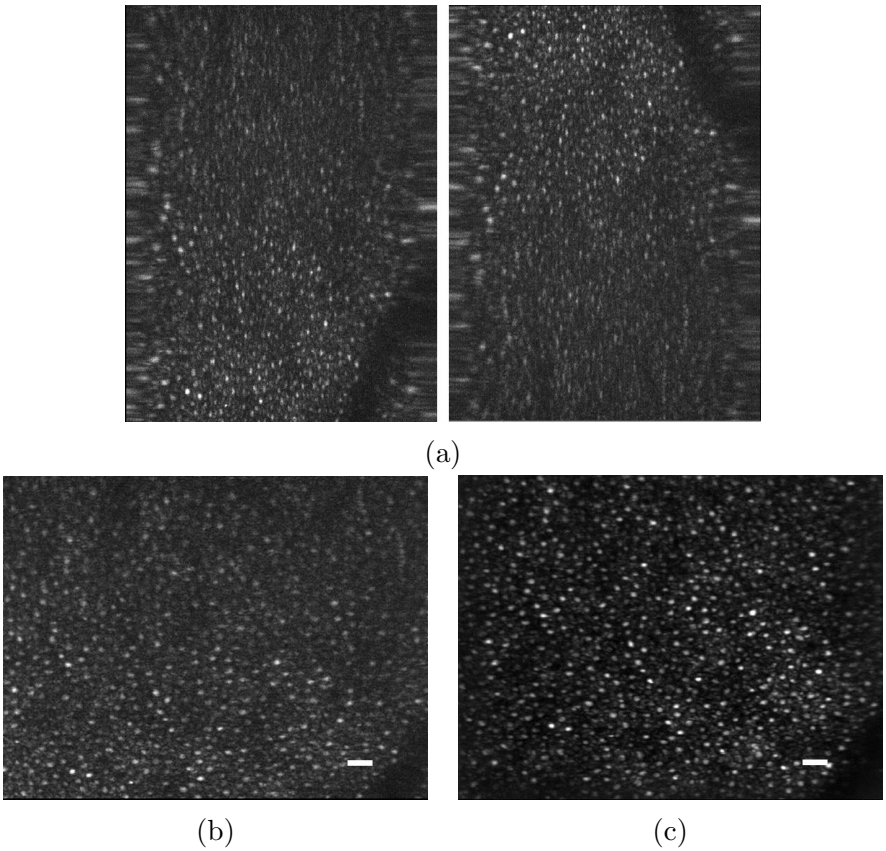

(a)

(b) (c)

Figure 4.6: Standard image processing steps for AO-cSLO images. (a) Raw image data of the forward and backward scan of the resonant scanner. (b) Single frame after dewarping and interwoven. (c) Averaged Image after applying correction to the single frames. The AO-cSLO image size is 2569 pixel×1096 pixel and covers a field of view of approximately 330 μm×330 μm. Scale bars = 20 μm. Image location is $\sim 8^{\circ}$ nasal from the fovea.

Averaging an undistorted sequence of frames is an important step to improve the signal to noise ratio while maintaining image sharpness. The number of frames contributing to an averaged image varied from 10 to more than 30. The final averaged image is shown in Figure 4.6c.

4.3.1 LSLO Software

Within this thesis the exact location of the field of view of the AO-SLO image within the LSLO image was determined. For this measurement the model-eye was used with the resolution test target (mentioned already in section 3.2.1) as sample. Using the pattern of the RTT the location of the FOV could be easily determined.

Chapter 5

Results and Discussion

The results chapter is split into four different sections. The first section presents and discusses the comparative study made between the zonal and modal wavefront reconstruction algorithms. Section 5.2 addresses the experiments realized with the tilted multimode fiber. Finally, in section 5.3 all the *in vivo* experiments are exhibit and thoroughly examined.

The subjects for all the experiments described in this thesis were volunteers, whose informed consent was obtained and to whom all possible risks of the measurement have been explained. All measurements were performed under a protocol that was approved by the local ethics committee.

5.1 Comparative study between modal and zonal wavefront reconstruction

In this section the results of the study on the wavefront reconstruction algorithms are described thoroughly. Firstly, it presents the outcomes with the model eye and then the ones obtained when performing *in vivo* measurements.

Several parameters are evaluated in order to fairly compare both methods, namely the computation time of the reconstruction, the Strehl ratio and the SNR improvement of the images after the aberrations correction.

Each type of reconstruction will provide its own wavefront phase values, according to which the appropriate driving voltages to be applied in the DM will be calculated. The changes in the DM will then correct the beam aberrations. From the several metrics that can be used to characterize the error of an AO system, the Strehl ratio (S) seems to be nowadays widely used, being

formally defined as the ratio of the maximum value of the measured PSF over the maximum value of the diffraction-limited PSF. Typically the quality of an optical system is regarded as diffraction limited for a Strehl ratio value of 0.8, which corresponds to an RMS value $\leq \frac{\lambda}{14}$. Diffraction limited means that it can be considered that the dominant effect in degrading the image quality is diffraction [24].

The Mahajan empirical estimation for the Strehl ratio provides a close approximation of the Strehl ratio value through the following equation [59]:

$$S_{Mahajan} = exp(-\sigma_{\phi}^2) \tag{5.1}$$

Where σ_{ϕ}^2 can be calculated in terms of the RMS wavefront error as $\sigma_{\phi} = 2\pi RMS_{\lambda}$ where RMS_{λ} is the RMS error in units of wavelength ($\lambda = 0.840\ \mu$m). This equation provides an approximation to the Strehl ratio with an error of less than 10% for S greater than 0.3. This limit corresponds to an RMS value $= \frac{\lambda}{5.7}$, which is equivalent to an RMS of 0.1474 in this thesis context [59].

5.1.1 Measurements in the Model eye

The evolution of the wavefront reconstruction and correction was evaluated for both the modal and the zonal reconstruction algorithms in the model eye, considering a pupil size as large as the mask being used for the wavefront reconstruction.

Figure 5.1 depicts the averaged evolution of both the RMS and the Strehl ratio value, calculated based on equation 5.1, after closing the adaptive optics loop. The modal reconstruction proved to yield a faster correction for the corresponding reconstructed wavefront. Both cases yielded residual aberrations that are well below the diffraction limit criteria used above.

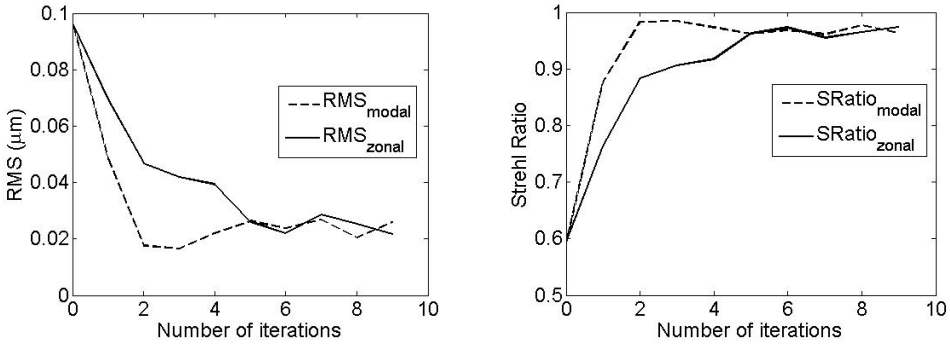

(a) (b)

Figure 5.1: Evolution of the wavefront in the model eye after closing the AO-loop. RMS (a) and Strehl ratio (b) for the zonal and modal reconstruction algorithms. The model-eye pupil size was 8 mm.

The progression of the wavefront correction is illustrated in Figures 5.2 and 5.3 for both reconstruction algorithms. The decrease in the RMS value with each iteration can be clearly observed.

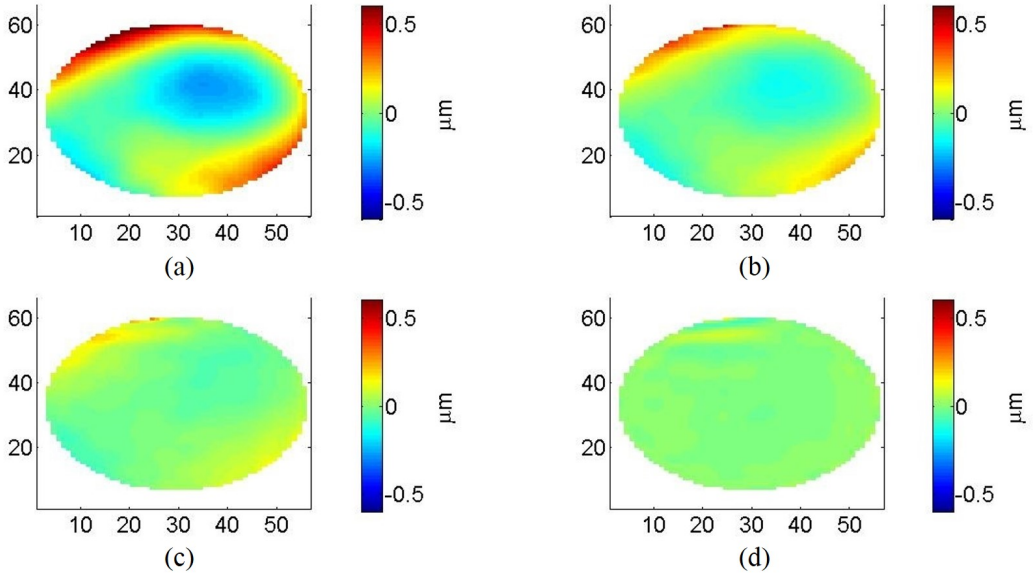

Figure 5.2: Performance of the wavefront correction using the modal reconstruction algorithm. The RMS values for each phase map are: (a) Before starting the AO-loop 0.178 μm; (b) After one iteration 0.097 μm; (c) After two iterations 0.049 μm; (d) After four iterations 0.018 μm.

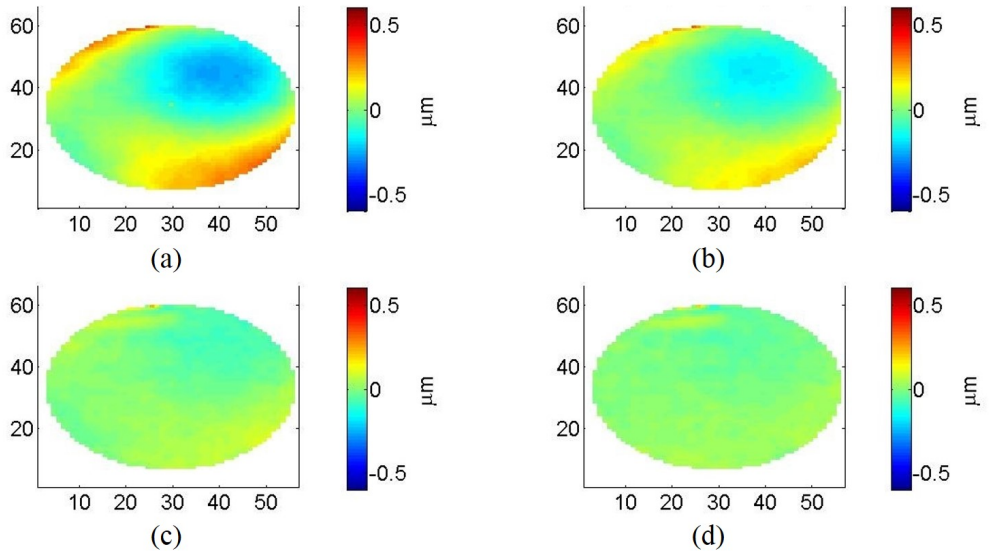

Figure 5.3: Performance of the wavefront correction using the zonal reconstruction algorithm. The RMS values for each phase map are: (a) Before starting the AO-loop 0.142 μm; (b) After one iteration 0.096 μm; (c) After three iterations 0.047 μm; (d) After eight iterations 0.026 μm.

The computation time of one iteration step, either in closed loop or open loop, for both algorithms was calculated in several situations using the model-eye (cf. Table 5.1). Both the size of the mask defined for the wavefront reconstruction and the pupil size of the model-eye were modified. In situation A the size of the pupil is the same as the mask size. In situation B the pupil is smaller than the mask, whereas in situation C the mask size was reduced to fit the small pupil.

Table 5.1: Comparison of the computation times of the reconstruction algorithms for different situations. A - Full Mask & Full Pupil; B - Full Mask & Smaller Pupil; C - Smaller Mask & Smaller Pupil

	Modal		Zonal	
	Closed Loop	Open Loop	Closed Loop	Open Loop
A	3.30 s	0.70 s	5.84 s	1.15 s
B	3.08 s	0.69 s	3.30 s	0.73 s
C	2.86 s	0.61 s	1.20 s	0.69 s

Both reconstruction algorithms yielded a faster loop cycle in the situation of a small pupil and where the mask used had a size more close to the real

pupil size being imaged into the SH-sensor. This difference was particularly significant when using the modal reconstruction.

In order to assess the differences in image quality the SNR was calculated for all configurations. The standard deviation of the noise in a single-frame image was $\sigma_{noise} = 44$, the signal to noise ratio of the image after the adaptive optics correction was calculated using equation 3.1. Table 5.2 summarizes the SNR for the different situations A, B and C.

Table 5.2: Comparison of the signal to noise ratio (SNR) of the AO-cSLO images of the model-eye after the aberrations correction for the studied reconstruction algorithms in different situations. A - Full Mask & Full Pupil; B - Full Mask & Smaller Pupil; C - Smaller Mask & Smaller Pupil

	Modal	Zonal
A	21.12 dB	21.12 dB
B	13.98 dB	13.57 dB
C	17.88 dB	17.49 dB

The first thing to note in table 5.2 is the enhancement of the SNR in the case of a small pupil size when a mask is used that corresponds to the size of the pupil. If the mask is larger than the pupil the wavefront is extrapolated (modal case) or set to zero (zonal case) in regions outside the pupil. In both cases the elements of the deformable mirror are set inaccurately and do not compensate for the wavefront aberrations. In contrast, when using a smaller mask there is no activation of the actuators in the outer regions of the deformable mirror which in the end allows for a more precise wavefront reconstruction and correction.

5.1.2 In vivo measurements

With a view to studying the performance of both reconstruction algorithms *in vivo*, several measurements were recorded and further analysed. Firstly a subject with a particularly large pupil (subject_1) was imaged and in this situation the mask was set to full size.

To evaluate the difference of implementing an adjustable size mask, a subject with a smaller pupil was imaged (subject_2) and no drugs were administrated to dilate the pupil.

All the measurements and images here compared were performed in the same experimental conditions, namely the power of the AO-cSLO at the eye was kept the same ($\sim$ 400 μW).

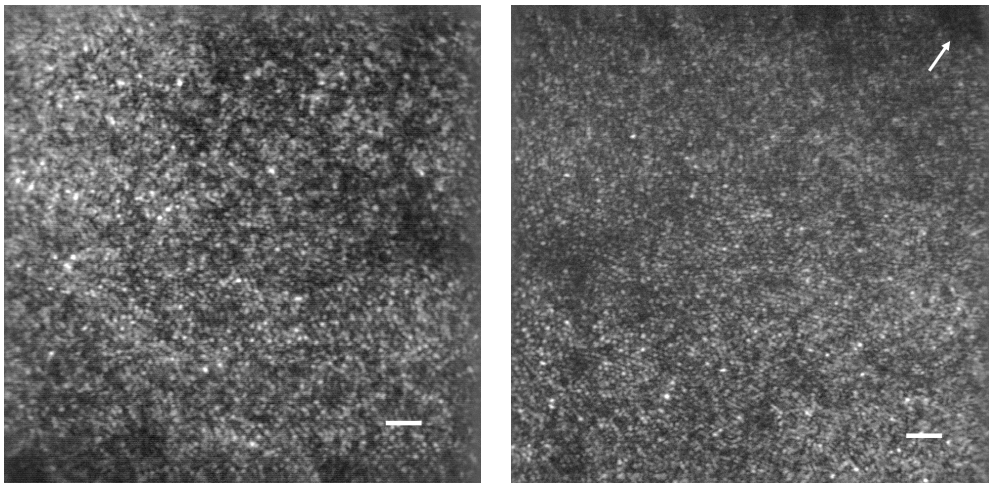

(a) (b)

Figure 5.4: *In vivo*: images of the fovea, recorded from subject$_1$. The scale bars are 20 μm across. Adaptive Optics correction based on: (a) modal wavefront reconstruction and (b) zonal wavefront reconstruction. The most likely central region of the fovea is indicated by an arrow.

Figure 5.4 shows the acquired images of the central fovea from subject$_1$, compressed for a size 1024×1024. The zonal reconstruction seems to provide a better resolution, which was confirmed by calculating the FWHM value of the normalized 2D autocorrelation, whose results are summarized in table 5.3.

It should be noted, however, that more measurements (several volunteers) are needed in order to confirm these findings.

Table 5.3: Comparison of the FWHM of the ACF of the images 5.4, acquired after the aberrations correction for the studied reconstruction algorithms.

	FWHM$_x$ (pixel)	FWHM$_y$ (pixel)	FWHM$_x$ (μm)	FWHM$_y$ (μm)
Figure 5.4a	40	16	5.2	4.8
Figure 5.4b	26	11	3.3	2.7

To test the behaviour of the different reconstruction algorithms in the case of smaller pupil sizes, a second volunteer subject was measured. Due to the small pupil size it was not possible to resolve the central foveal cones as in the

previous case, therefore all the measurements were targeting the bigger cones, present in the temporal region outside of the central fovea.

Figure 5.5 shows the wavefront reconstruction *in vivo* for the two algorithms being discussed and the corresponding calculated centres of gravity. As expected, the wavefront reconstructed by the zonal algorithm matches the pupil size of the subject, which can be seen through the COG data, shown in Fig.5.5b and Fig.5.5d.

One drawback of using the zonal reconstruction algorithm is the fact that tip/tilt are not removed from the retrieved phase map, which can be clearly seen in Figure 5.5c. Another drawback is that the subroutine of the software provided by ALPAO is password protected and not accessible. However, the adaptive optics correction, which is based on the wavefront reconstruction, does not seem to be affected although this will obviously increase the calculated RMS value. However, the tip/tilt can be easily removed in order to calculate the accurate RMS value in post processing.

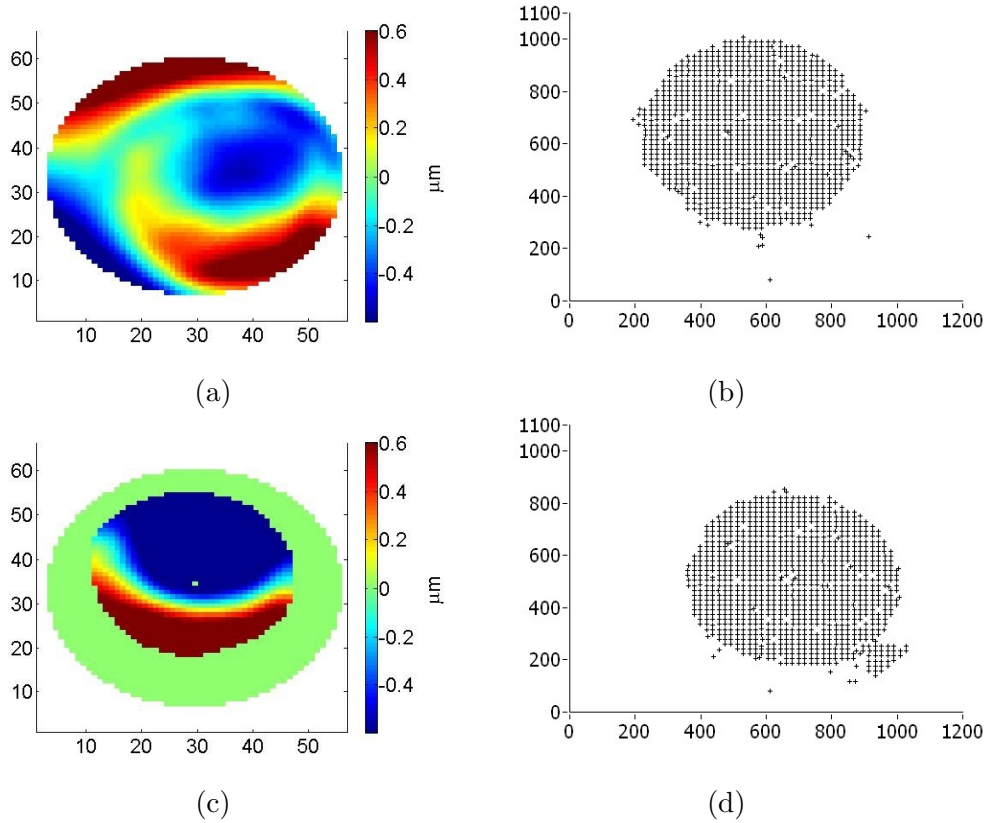

Figure 5.5: Wavefront reconstruction images recorded *in vivo* before AO-correction and respective centroids retrived from the SH-sensor. (a) Reconstructed wavefront (RMS=0.394 μm) for the modal algorithm. (b) Centers of gravity for the modal algorithm. (c) Reconstructed wavefront (RMS=0.633 μm) for the zonal algorithm. (d) Centers of gravity for the zonal algorithm.

Figures 5.6a and 5.6b show the photoreceptor layer images that were obtained in the measurements described above.

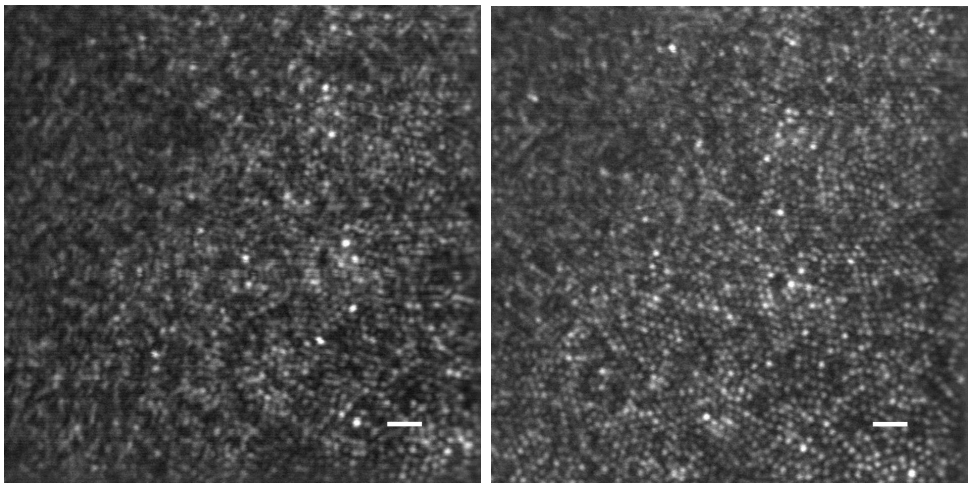

(a) (b)

Figure 5.6: AO-cSLO cone mosaic images recorded from subject$_2$. The wavefront reconstructions algorithms implemented were (a) modal and (b) zonal. The scale bars are 20 μm across.

The first thing to notice is that, once again as in Figure 5.4, when performing adaptive optics correction using the wavefront zonal reconstruction algorithm the image seem to have not a better resolution.

In order to analyse these images further the signal to noise ratio was calculated as well as the 2D auto correlation of both images (cf. Table5.4).

Table 5.4: Comparison of the FWHM of the ACF of the images 5.6, acquired after the aberrations correction for the studied reconstruction algorithms.

	FWHM$_x$ (pixel)	FWHM$_y$ (pixel)	FWHM$_x$ (μm)	FWHM$_y$ (μm)
Figure 5.6a	32	12	4.16	3.6
Figure 5.6b	28	11	3.64	3.3

A SNR of 9 was found for image 5.6b, whereas for image 5.6a the calculated SNR was 11.

Although the mask size proved to improve image quality in the model eye, it did *in vivo* not yield exactly the same results.

When using the modal reconstruction, the smaller mask size did not prove to enhance the image quality, regardless of the pupil size of the subject being imaged. In fact there was no improvement in the image resolution after AO-correction.

Nevertheless, for the zonal reconstruction implementing a mask that is adjusted to the pupil size seems to provide equivalent quality images, when compared to the condition of using the zonal wavefront reconstruction algorithm and the full mask. Further analysis of these images is outlined in the next section of this chapter.

Table 5.5 shows the averaged computation time for the two different wavefront reconstruction algorithms in two conditions. In the first one (A) the full mask size was used, whereas in second situation (B) a smaller mask was set.

Table 5.5: Comparison of the computation times of the reconstruction algorithms for *in vivo* measurements in two different situations. A - Full Mask; B - Smaller Mask

	Modal		Zonal	
	Closed Loop	Open Loop	Closed Loop	Open Loop
A	3.08 s	0.63 s	3.24 s	0.58 s
B	3.00 s	0.60 s	1.23 s	0.74 s

Looking at the numbers obtained in table 5.5, we notice firstly, that the difference between the computation time of the modal and zonal reconstruction algorithms with the closed loop is not particularly significant for the full mask. Secondly, we can see that with the zonal reconstruction algorithm and with a smaller mask the loop is 2 seconds faster when closed, which becomes specially relevant when measuring patients, because the fixation capabilities are in general poorer than in the case of healthy subjects.

In conclusion, all the measurements made in the context of this thesis support the assumption that the zonal wavefront reconstruction algorithm yields images that are sharper and have a better contrast. However, it should be mentioned that when imaging large pupils from healthy subjects the modal reconstruction yields images with similar quality.

In addition from measurements in the model eye, it was expected that the smaller mask would improve the image quality in the case of smaller pupils, regardless of the algorithm for the wavefront reconstruction. However, in the case of *in vivo* measurements it did not show any improvement. It only proved to decrease the computation time in the case of the zonal reconstruction.

For the zonal reconstruction though, the use of a smaller mask seems to

provide similar quality images. Moreover it has the advantage of reducing significantly the computation time.

From now on, all the data presented and analysed refers to measurements performed using the zonal wavefront reconstruction algorithm.

It is important to be aware that to prove accurately the conclusions drawn above further measurements need to be performed in order to provide statistically significant data.

5.2 Investigation of the influence of a tilted multimode fiber on the image quality

In order to collect more multiple scattered light and suppress contributions from directly backscattered light, thus improving contrast of retinal vasculature structure, the use of a multimode fiber (MMF) with different tilts for light collection was investigated.

First, tests were performed in a model-eye, which is highly scattering and changes caused by tip/tilt of the MMF can be investigated in a controllable manner. In Figure 5.7 two images of the sheet of paper of the model-eye are shown. The first one was recorded by applying a 0° tilt to the fiber tip, which means that the fiber was in the traditional confocal configuration. The second image was recorded by applying a 0.12° tilt to the fiber.

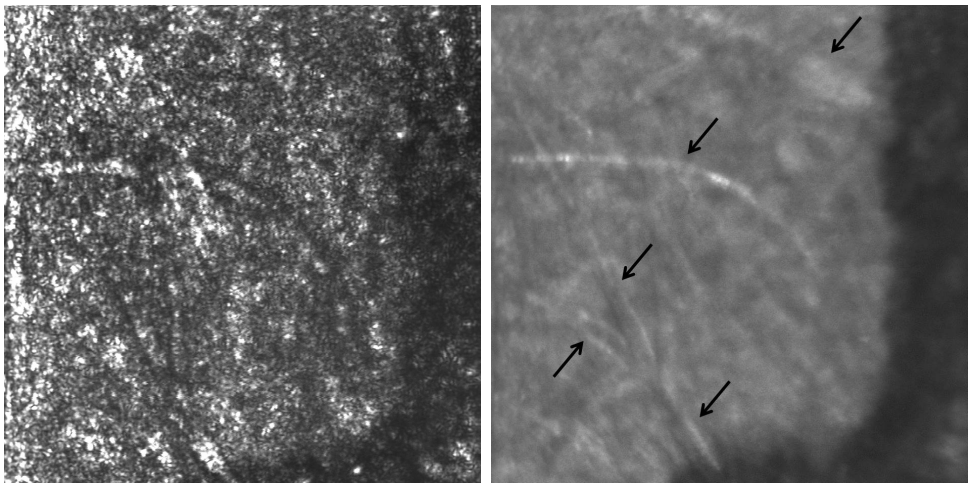

(a) (b)

Figure 5.7: Images of the model-eye recorded with (a) No tilting of the fiber and (b) Tilting of the fiber by 0.12°.

Different amounts of tilt allowed collection of multiple scattered light from deeper layers and rejection of direct backscattered light. This allows the visualization of different structures (indicated by the black arrows), which would be otherwise masked in the traditional confocal approach.

Although very promising, the tilting of the multimode fiber did not yield the expected results in the *in vivo* experiments carried out. For the experiments the focal plane was not set to the photoreceptor layer but to the anterior layers that contain the vessels structures. The tilting mainly resulted in a strong reduction of the light intensity being detected in the APD, without any

noticeable improvement in the visualization of the vascular structure .

One problem during these experiments was the low signal intensity, which resulted in a failure of the image registration algorithm and prevented a meaningful frame averaging. Therefore a different concept needs to be applied which measures both, the direct backscattered light (for image registration) and the multiple scattered light (using a multimode fiber) simultaneously.

5.3 Test of the AO-SLO system performance for in vivo measurements

The arguments behind the ambition to improve the AO-cSLO performance mentioned in this thesis are immense, from which one can highlight a few. For instance, the analysis of the regularity and spacing of the cones and rods mosaic, as well as the photoreceptors density, plays an important role in the diagnosis and progression of some diseases, such as diabetic retinopathy (DR) or age-related macular degeneration (AMD). In addition, *in vivo* studies of small retinal vessels may also provide valuable information about early vascular changes in DR [3, 60].

In this section the results obtained by imaging of different targeted regions of the human retina with the improved AO-SLO instrument are going to be analysed. Several images of the photoreceptors mosaic are here presented and the system's capability of imaging the retinal vessels is investigated.

It is worth mention that no drugs for pupil dilation were used in the measurements presented in this thesis, despite being a usual procedure in AO-assisted imaging. However, even without dilation the pupil of subject_1 reached the maximum size that is supported by the instrument.

In order to determine distances on the retina the axial eye lengths have to be known. The axial lengths of the eyes imaged were measured by a commercial device (IOL-master, Carl Zeiss Meditec), and are provided in Table 5.6 , along with other relevant information.

Table 5.6: Summary of the subjects that were imaged.

Subject	Gender	Eye[1]	Axial Length (mm)	Anterior Segment Depth (mm)
1	Male	OS	23.32	3.89
2	Male	OS	22.3	3.32

With the overview image provided by the LSLO, whose field of view accounts for 7.2°×5.2°, the identification of the retinal location which is imaged with the AO-SLO is straightforward.

[1]OS stands for left eye

The AO-cSLO measurements presented here were acquired using a single-mode-fiber as confocal pinhole, since it provides images with the best resolution. Each image consists of 2569×1096 pixels. For a convenient display in this thesis the images were resampled to a size of 1024×1024 pixels and cover an area of $\sim 1° \times 1°$ on the retina. In order to convert the scanning angle into distances on the retina, the distance from the lens surface to the retina must be known. This distance can be calculated as the difference between eye length and anterior segment depth (assuming that the pivot point of the scanner is imaged onto the surface of the lens).

Considering that the AO-cSLO image size is 2569×1096 the following table 5.7 was constructed, which shows the field of view for each subject. The data provided in table 5.7 was used to convert the measured distance in pixel units to a distance in μm.

Table 5.7: Distances on the retina for the different subjects (scanning angle was kept constant at $\sim 1°$).

Subject	$FOV_x(\mu m)$	$FOV_y(\mu m)$	$Pixel_x(\mu m)$	$Pixel_y(\mu m)$
1	331	330	0.13	0.30
2	339	336	0.13	0.30

Due to the regular arrangement of the photoreceptors, it is possible to quantify their spacing (i.e. next neighbour distance (NND)) by performing a Fast Fourier Transform (FFT). The NND can then be used to calculate the cone density. The dominant spatial frequencies resulting from the photoreceptor's regular arrangement of the photoreceptor appear as rings on the FFT, the so called Yellott rings. Outside the fovea one can find both rods and cones, and in that case, two circles should be visible in the FFT. The radius of the rings will then correspond to the row to row spacing of the individual photorecptor type.

The visibility of the Yellott's rings can be regarded as a good indicator for the capability of an AO-equipped instrument to resolve individual cells such as rods and cones. Only if the resolution of the system is sufficient to resolve these structures Yellott's rings will be visible.

Image processing was all done in LabView, as described elsewhere in this thesis. After frame averaging, the images were converted to a format that can be imported with ImageJ, an open source Java-based image processing pro-

gram. ImageJ was used to perform further analysis of the images, such as the above mentioned 2D FFT calculation.

5.3.1 Wavefront correction

All images were recorded after correction of the wavefront aberrations, that can be monitored with the aceguiWFSOptocraft.vi Labview program.

Figure 5.8 shows the evolution of the wavefront correction, after closing the AO-loop, prior to the recording of image data which is presented later in this section. In this specific case a smaller mask for the wavefront reconstruction was implemented.

As can be seen, with every iteration the RMS value decreases until it reaches a stable value of around 0.04 μm, which is already considered below the diffraction limit value of $\frac{\lambda}{14} = 0.06$ for a wavelength λ=0.840 μm.

The ability to record images of wavefront maps for every measurement enables a better understanding of the relation between the wavefront correction and the image quality.

It is important to mention that even in the case when the residual wavefront error indicates diffraction limited performance the resolution might be lower because not all aberrations might be detected by the HS-sensor. Therefore, the ability of the system to resolve rods and foveal cones was used to determine the achievable resolution on the retina.

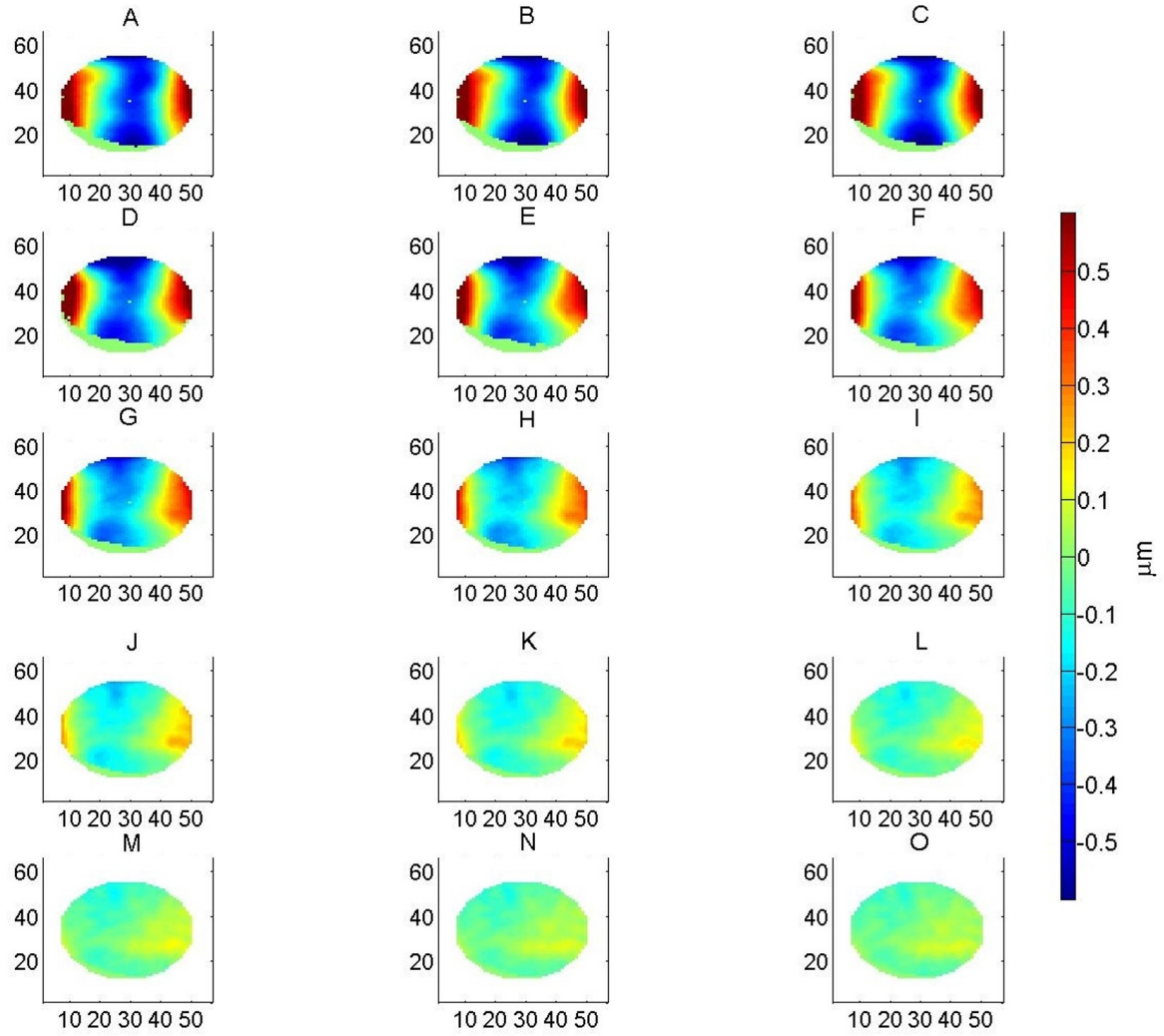

Figure 5.8: Evolution of the wavefront correction (zonal reconstruction) after closing the AO-loop in subject$_1$. The RMS values for each image are: Before AO correction: A - 0.336 μm; 1 iteration: B - 0.354 μm; 2 iterations: C - 0.350 μm; 3 iterations: D - 0.348 μm; 4 iterations: E - 0.305 μm; 5 iterations: F - 0.267 μm; 6 iterations: G - 0.232 μm; 7 iterations: H - 0.185 μm; 8 iterations: I - 0.147 μm; 9 iterations: J - 0.117 μm; 10 iterations: K - 0.095 μm; 11 iterations: L - 0.076 μm; 12 iterations: M - 0.062 μm; 13 iterations: N - 0.051 μm; 14 iterations: O - 0.046 μm.

5.3.2 Imaging of foveal cones

In this subsection images of the fovea from two different healthy volunteers are presented.

Cone photoreceptors act like tiny waveguides. As such, light that enters them is preferentially redirected back through the pupil, producing a high

contrast mosaic of bright spots in the retinal image. Therefore they have been one of the favourite targets in AO-cSLO imaging [61].

The eye pupil of the first subject has a larger diameter, which enables to resolve the cones in the central fovea, which is not possible for the second subject because the pupil size is considerably smaller.

In Figure 5.9 the individual foveal cone photoreceptors can be clearly resolved almost throughout the whole image, with exception of the central part of the fovea (lower left corner, marked with an arrow). Due to the large variation of the reflectance of each photoreceptor it has been previously proposed to display these images in a logarithmic scale [35].

The dark lines visible in the images are shadows of vessels, whose location is anterior to the confocal image plane.

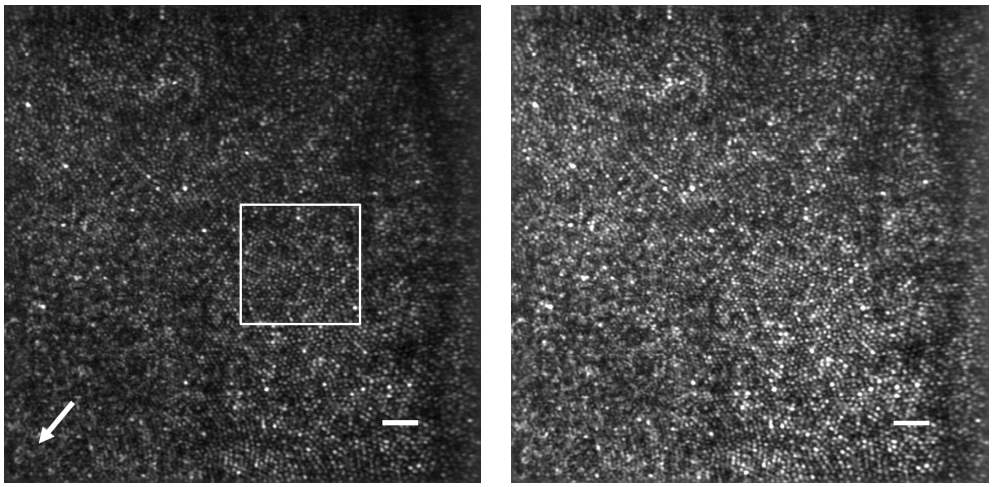

(a) (b)

Figure 5.9: Reflectance images of the human cone mosaic near the central fovea from the subject$_1$, collected using 840 nm light and single-mode fiber in the detection unit. The same image is shown with linear (a) and logarithmic (b) grayscales, to facilitate visualization of the cone mosaic. The arrow points to the fovea centralis. The scale bars are 20 μm. The white square indicates the region of interest for further analysis.

A 2D FFT was calculated for the selected region assigned with a white square (cf. Fig. 5.10a). Yellott's ring can be clearly observed in the FFT of the image (cf. Fig.5.10b), indicating the regular arrangement of the cones in this region and confirming the high lateral resolution of the AO-cSLO instrument.

Assuming an hexagonal packing of the cones, with the radius of the Yellott's ring, which corresponds to the spatial frequency of cone rows, one can obtain the closest neighbour cone spacing.

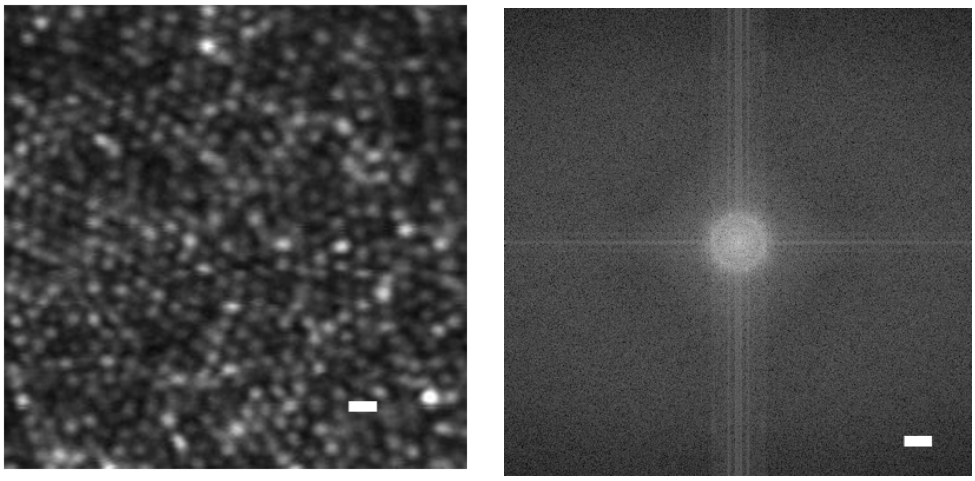

(a) (b)

Figure 5.10: (a) Enlarged view of the ROI marked in 5.9a where the scale bar is 5 μm. (b) Power spectra obtained by 2D FFT of (a), where Yellott's ring is clearly visible. The scale bar is 0.3 cycles/μm.

To have a more accurate estimate of the radius size the radial average of 5.10b can be performed, using the plugin "*Radial Profile Angle*", available in the Plugins menu of ImageJ. The resulting average is depicted in 5.11.

The radius can be identified as the first pronounced peak that appears. The closest neighbour spacing is then calculated by a straightforward multiplication of the obtained value for the radius by a factor of $(1/\cos 30°)$. This factor arises from geometric considerations on the cone mosaic arrangement [62].

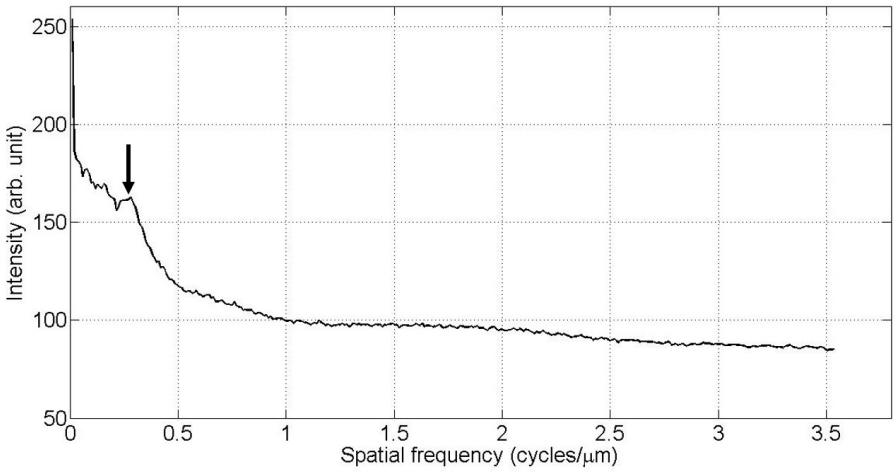

Figure 5.11: Radial average computed over the FFT image 5.10b. The arrow indicates the peak that corresponds the local peak that most likely corresponds to the spatial frequency of cone rows (0.308 cycles/μm).

The calculated closest neighbour spacing of $\frac{3.24}{cos(30°)} = 3.74$ μm is in good agreement with recently reported results [63] and data from histology.

Figure 5.12 shows the AO-cSLO retinal image of subject$_2$ and different 80 μm$\times$80 μm patches of the cone mosaic that were further analysed. A FFT was calculated for each of these regions, starting with the square on the upper left side where the cones are too small to be resolved. The respective FFT's are depicted in Figure 5.13.

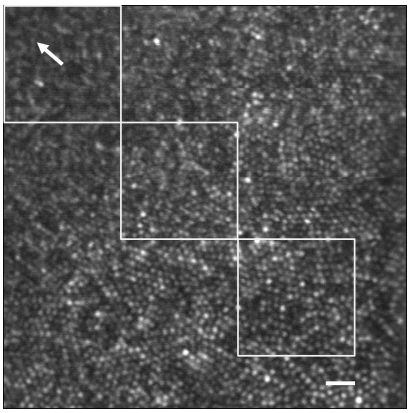

Figure 5.12: AO-cSLO image recorded near the central fovea from volunteer 2. The squares mark the regions of interest where the 2D FFT's were performed. The scale bar is 20 μm. The arrow points to the fovea.

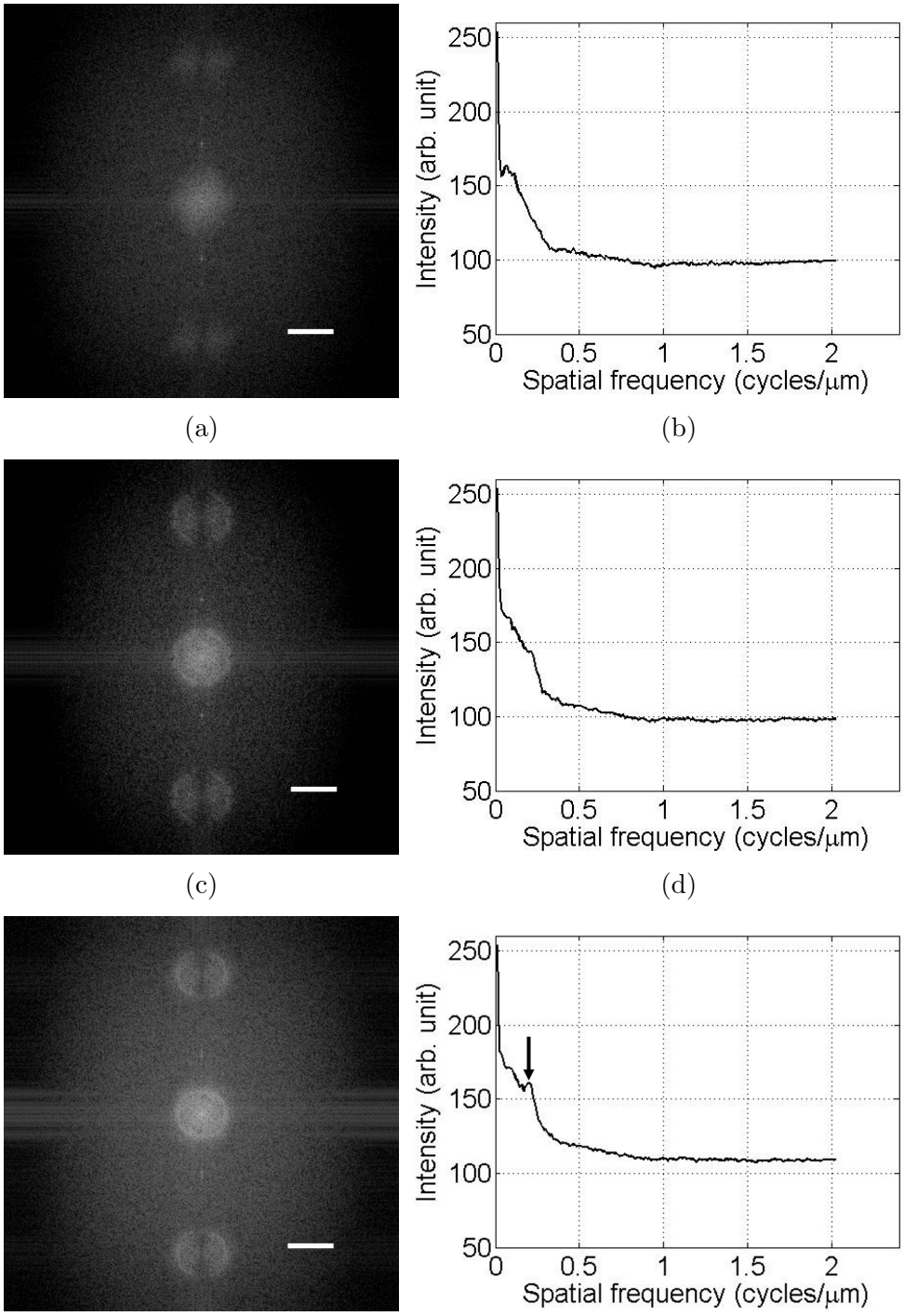

(a) (b)

(c) (d)

(e) (f)

Figure 5.13: 2D FFT of (a) ROI 1, (c) ROI 2 and (e) ROI 3. (b), (d) and (f) are the corresponding radial averages, where the arrow on graph (f) marks the peak correspondant to the ring frequency. The scale bars are 0,2 cycles/μm across

It can be clearly seen in Figure 5.13 that the more further away from the

fovea the ring becomes more pronounced. At the lower right side of figure 5.12 the individual cone photoreceptors can be clearly resolved (indicated by the sharp ring in Figure 5.13(e)). These can not be resolved in the fovea centralis (upper left region in Figure 5.13). This is evident from figure 5.13(a) which shows a blurred ring.

In the radial average of the FFTs (cf. figures 5.13(b),(d) and (e)) the loss of ring visibility can be better observed. As Yellott's ring becomes more pronounced an intense peak can be seen which indictes the spatial frequency of the cones.

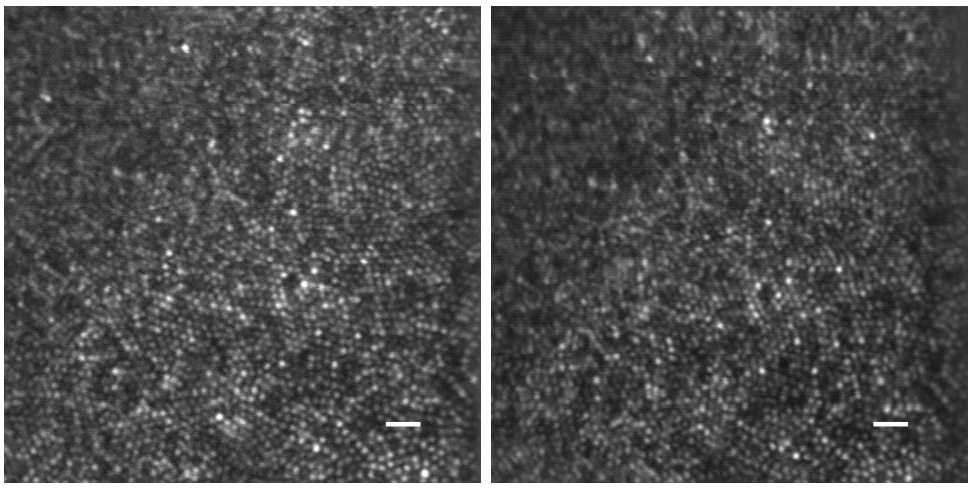

(a) (b)

Figure 5.14: Cone mosaic near the central fovea, measured from subject$_2$. Two different masks were used for wavefront reconstruction, (a) full mask and (b) small mask size. The scale bars are 20 μm.

Figure 5.14 compares the quality of the images of the cone mosaic recorded from subject$_2$, using different mask sizes for the wavefront reconstruction. As it can be seen there is not much difference between the image acquired using a full mask for the wavefront reconstruction and the image acquired using an adjusted size mask (the smaller mask mentioned in section 4.1) , apart from a slight difference in the SNR. The SNR of the left image is 10 dB whereas for the right image is 9 dB.

The calculated ACF of the images proved to be very similar (cf. Table 5.8), being just of one pixel unit the difference between the FWHM in both x and y directions. Nevertheless, the image obtained with the full mask size implementation was the one whose ACF had the narrowest peak.

Table 5.8: Comparison of the FWHM of the ACF of the images in figure 5.14.

	FWHM$_x$ (pixel)	FWHM$_y$ (pixel)	FWHM$_x$ (μm)	FWHM$_y$ (μm)
Fig.5.14a	28	11	3.6	3.3
Fig.5.14b	29	12	3.7	3.6

5.3.3 Rod imaging

Rod dysfunction is associated with a number of retinal diseases, such as retinitis pigmentosa or age-related macular degeneration. It is therefore important to develop tools that allow routinely assessment of the rod structure in the living retina.

The size of the rods is in the order of the diffraction limited resolution ($\sim$2 μm) that is supported by the optics of the eye. In order to visualize these structures perfect wavefront correction has to be ensured. With the purpose of testing the ability of the AO-SLO instrument to resolve rod photoreceptors the temporal region of the eye was imaged. Figure 5.15 shows first imaging results of the photoreceptor mosaic that were recorded at about 7° eccentricity temporal from the fovea.

The left image was recorded during wavefront correction that was based by calculating the wavefront within the full available mask size, whereas the right image shows imaging results obtained using a mask size that was reduced to match the pupil size. Both images show sparsely packed bright large spots (corresponding to cones) that are surrounded by smaller and densely packed spots (corresponding to rods). Comparing both images, the presence of the smaller rods appears to be more pronounced on the left image.

Further analysis of both images revealed a slightly higher SNR of 14 dB for the left image compared to 13 dB for the right image.

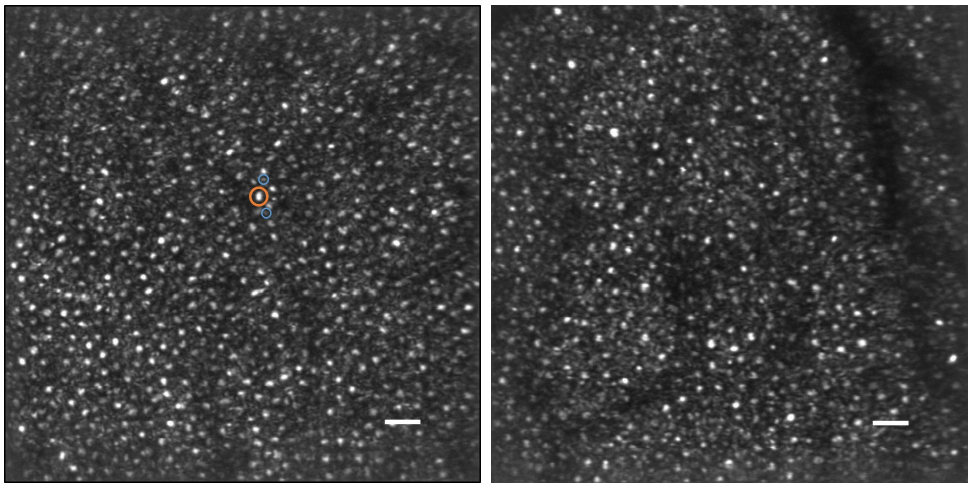

(a) (b)

Figure 5.15: Images of the photoreceptor mosaic showing rods and cones recorded in the temporal region (subject$_1$). (a) Wavefront reconstruction for AO control was performed within the full mask size. The orange circle marks a cone photoreceptor and the blue circles rod photoreceptors. (b) Wavefront reconstruction for AO control was performed within an adjusted smaller mask size. The scale bars are 20 μm.

Further analysis is focused on the better image (cf. Fig.5.15a).

In order to test the capability of the system to resolve the regular structure of the rods a 2D FFT of the whole image that is presented in Figure 5.15a is calculated and displayed in Figure 5.16. Roughly two rings can be observed. The interior ring (cf. orange arrow) corresponds to a low spatial frequency caused by the regular arrangement of the cones. Note that at this eccentricity from the fovea the cone spacing is much lower which results in a lower spatial frequency in comparison with images recorded closer to the fovea (cf. Fig.5.10). The second ring (cf. blue arrow in Fig.5.16), although very faintly visible, corresponds to the spatial frequency of the rod mosaic.

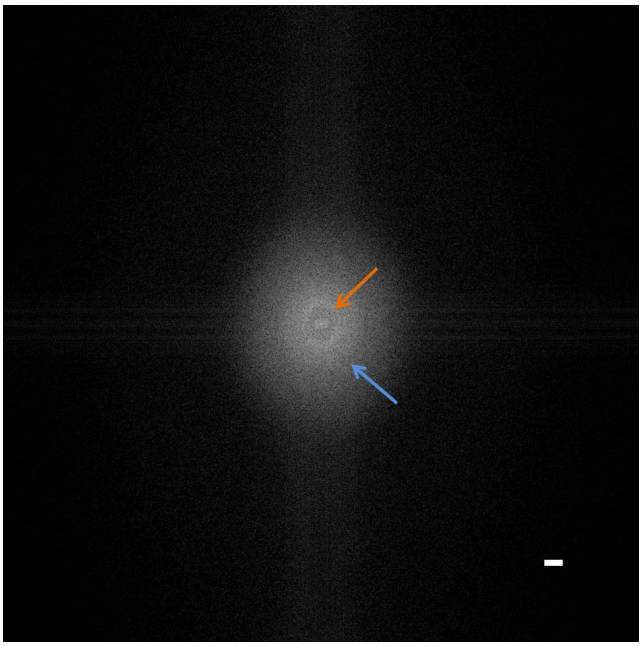

Figure 5.16: 2D FFT of the entire image shown in Fig.5.15a. The scale bar is 0.1 cycles/μm.

However, when performing a radial average (similar to the previous chapter), only one peak which corresponds to the spatial frequency of the cones can be observed (cf. Fig. 5.17). The peak in the graph (cf. arrow in Fig. 5.17) can be observed at a location that corresponds to 0.112 cycles/μm which is equivalent to a cone row to row spacing of $\sim$8.93 μm.

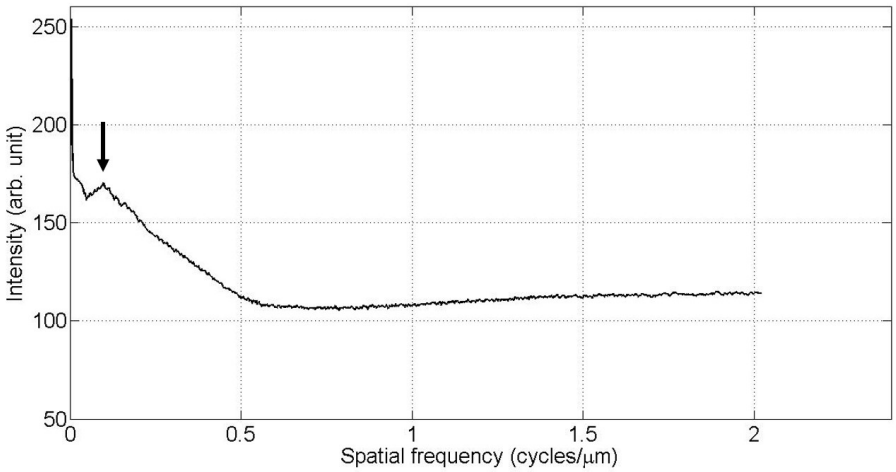

Figure 5.17: Radial average computed over the 2D FFT image shown in 5.16. The arrow indicates the peak that corresponds to the pronounced spatial frequency of the cone rows.

Despite being very promising, the above analysis indicates that so far the

AO-cSLO system is not able to completely resolve the rods at this eccentricity. This might be caused by the relatively low sampling density in y-direction or residual wavefront aberrations that are not measured and corrected for.

In order to compare the imaging results for the different mask sizes the 2D FFT and the FWHM of the 2D autocorrelation function was calculated for both images that are shown in Fig. 5.15. Looking at the 2D FFTs shown in Fig. 5.18, it is possible to conclude that not only Yellott's ring that corresponds to the spatial frequency of the cones is less pronounced (cf. Fig.5.16) but also no evidence of a second ring (that corresponds to the spatial frequency of the rods) can be observed. Table 5.9 summarizes the results obtained via the FWHM of the autocorrelation function that was calculated for each image.

Overall, a wavefront reconstruction that is performed over the entire full mask seems to yield the best image quality, regardless of the subject's pupil size.

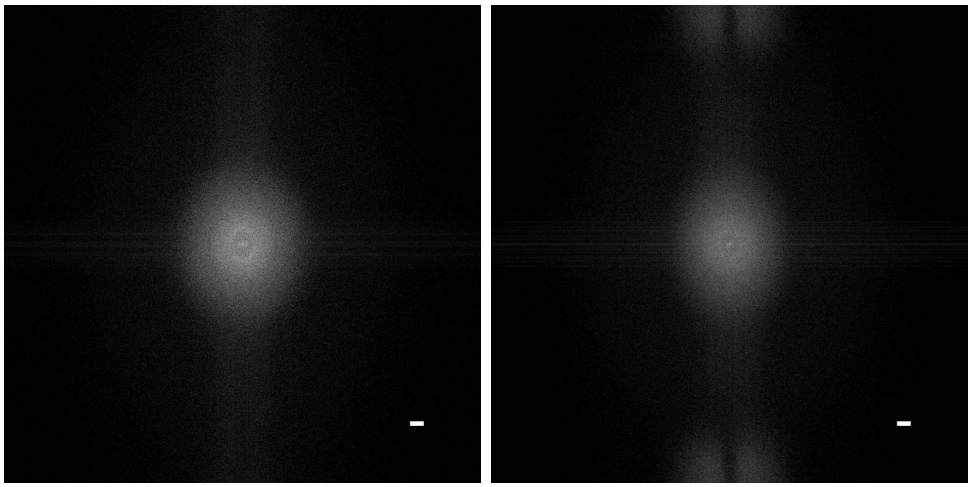

(a) (b)

Figure 5.18: 2D FFT performed over the entire images shown in Fig. 5.15. (a)2D FFT of Fig. 5.15a. (b)2D FFT of Fig. 5.15b. The scale bar is 0.1 cycles/μm.

Table 5.9: Comparison of the FWHM of the ACF of the images displayed in Fig.5.15.

	FWHM$_x$ (pixel)	FWHM$_y$ (pixel)	FWHM$_x$ (μm)	FWHM$_y$ (μm)
Fig.5.15a (full mask)	36	14	4.6	4.2
Fig.5.15b (reduced mask)	41	16	5.3	5.2

In comparison with previously published images [9] the following differences have to be emphasized. In [9] a wavelength of 680 nm was used for imaging while in this thesis the instrument was operated at 840 nm. Due to the longer wavelength a 24% loss of resolution is expected which degrades the rod visibility. In addition, no drugs for preventing accommodation were applied. Therefore adaptive optics correction in the measurements shown above might be degraded by residual accommodation influences.

5.3.4 Imaging of retinal vasculature

Anterior layers of the retina show high level of perfusion and are of specific interest for various diseases. Imaging of retinal vasculature on a cellular level might therefore be a promising tool for investigating these diseases including diabetic retinopathy or Glaucoma. In this section the AO-SLO instrument is tested on the ability of assessing retinal vasculature.

A key feature that simplifies the examination of the vessel structure is the combination of the AO-cSLO With the overview LSLO. Subject alignment can be done very fast and the specific regions of interest for AO-cSLO imaging can be rapidly found. All images presented in the following were recorded from subject_1 (eye length of 23.32 mm). With the corresponding eye length the LSLO covers an area of 2.44 mm×1.76 mm on the retina. In previous work the LSLO had already proved to be a suitable tool to image the retinal vessels [11]. However, this thesis work enabled for the first time the simultaneously measurement of LSLO and AO-cSLO. Figure 5.19 shows an example of an overview LSLO image during a measurement.

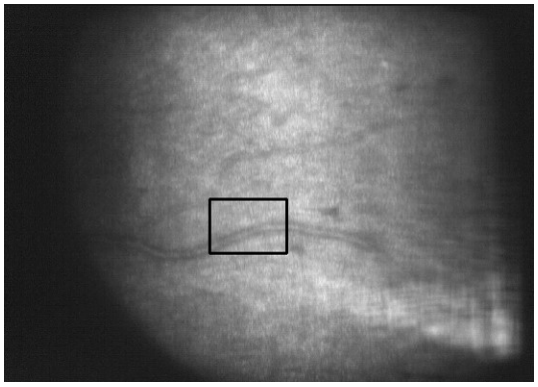

Figure 5.19: Overview LSLO image of the retina showing the field of view covered by the AO-cSLO with a black rectangle. Field of view of 2.44 mm×1.76 mm.

Because of its confocality, the AO-cSLO is able to axially section different regions of the retina. Although the depth resolution is lower than that provided by optical coherence tomography a clear separation between photoreceptor layer and vasculature layers can be achieved. The possibility to change the focal plane within the retina can be achieved by applying a certain amount of defocus on the deformable mirror. However, this function is only supported by the AO-software when the modal reconstruction algorithm

is used.

Figure 5.20 shows an example of an image recorded from the retina with the focal plane of the AO-SLO located at the anterior layers. The blood vessel appears as a continuous bright line with neighbouring dark areas. However, the central part of the vessel is much narrower in the AO-SLO image than in the SLO image (cf. Fig. 5.19). This can be explained by the fact that only the central part of the vessel scatters sufficient light back to the confocal aperture. Outside of this central part the light is mainly scattered into different directions. Therefore these areas appear dark in the AO-SLO image while equivalent areas are broadened in the LSLO because the confocality of this imaging modality is rather poor. The surrounding structure of the vessel can mainly be attributed to the retinal nerve fiber layer which shows strong backscattering compared to other anterior retinal layers.

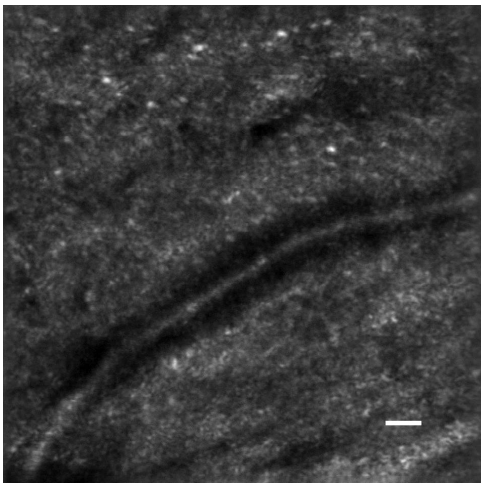

Figure 5.20: Adaptive Optics SLO image with the focal plane set to the anterior layers of the retina. The scale bar is 20 μm.

To demonstrate the ability of the system to set the focal plane at different depths within the retina, Figure 5.21 shows images of approximately the same location but with the focal plane set to the photoreceptor layer. The photoreceptor mosaic and shadows caused by light absorption within the vessels can be can be clearly observed.

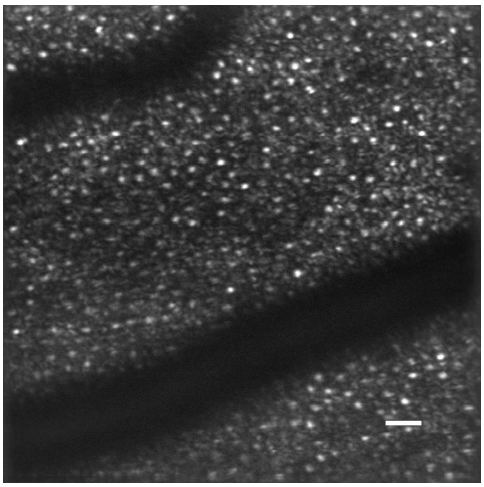

Figure 5.21: Adaptive Optics SLO image with the focal plane set to the photoreceptor layer of the retina. (The scale bar is 20 μm).

5.3.5 Confocal pinhole

In all the previous measurements a single mode fiber was used for confocal detection. This section shows *in vivo* images recorded from subject$_1$ using a conventional pinhole. The pinhole configuration uses a 30 μm pinhole together with a 50 mm focal length lens (configuration B as explained in section 3.3).

In order to provide a quantitative assessment of the differences the same image metrics as previously mentioned are used (SNR and ACF).

The used configuration yielded only a poor transverse resolution therefore a location outside the fovea ($\sim$7° temporal) was chosen for imaging.

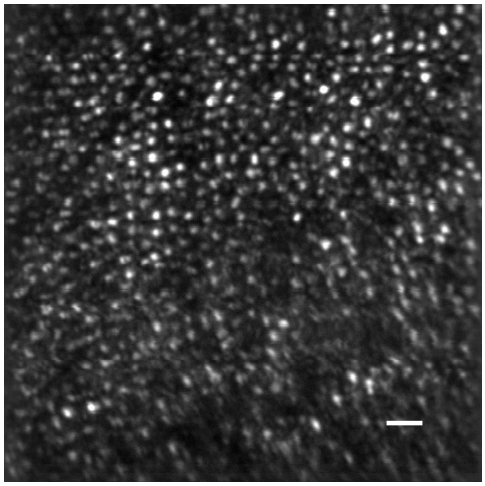

Figure 5.22: Image of the cone mosaic of subject$_1$ at $\sim$ 7° temporal to the fovea recorded with the pinhole configuration B. The scale bar is 20 μm.

The SNR value found for Figure 5.22) was 14 dB. This value is in the same range as values obtained from images acquired using the single-mode fiber configuration (cf. Sec. 5.3.3). Table 5.10 sumarizes the calculated FWHM of the autocorrelation function of the image.

Table 5.10: FWHM of the ACF of the image displayed in Fig. 5.22

FWHM$_x$ (pixel)	FWHM$_y$ (pixel)	FWHM$_x$ (μm)	FWHM$_y$ (μm)
45	19	5.8	6.2

Although the SNR is similar the resolution is clearly degraded compared to the single mode fiber configuration (cf. Tab.5.9). However, it should be noted that not the optimum pinhole configuration could be used in this thesis. In

order to achieve similar confocality as in the single mode fiber case, a different pinhole size or different focusing lens has to be used.

Chapter 6

Conclusions and Future Work

6.1 Conclusions

Within this thesis, an adaptive optics scanning laser ophthalmoscope (AOSLO) was optimized and its performance was evaluated. One key feature of the system is the simultaneous recording of line scanning laser ophthalmoscopy (LSLO) images which greatly simplifies subject alignment and the determination of the location that is imaged with the AO-SLO. After implementation of the improvements the LSLO and AO-SLO can now be operated simultaneously and the adaptive optics loop runs stable even in the case of in vivo measurements. The imaging capability of the system is demonstrated by in vivo imaging of the human cone and rod mosaic as well as the visualization of retinal capillaries.

The best performance of the system was achieved with a zonal reconstruction of the wavefront which is recommended to use when high resolution is required. However, the processing time is increased compared to the modal approach which might limit the applicability in patients.

Improved visualization of retinal vasculature using a tilted multimode fiber in the detection arm could not be achieved within this thesis. Although measurements in the model eye were promising, the translation to the in vivo situation did not show improved contrast of these structures. Probably the tilt angle has to be further increased. However, this will further reduce the amount of light from the retina that can be detected with the multimode fiber. In order to provide sufficient SNR in the images, frame averaging has to be employed. However, this requires a different configuration where the confocal light is not lost and can be used for imaging and for motion correction.

The possible next steps proposed for this instrument are outlined below.

6.2 Future Work

As future developments, the adaptive optics loop time has to be decreased. Currently, 3 seconds are needed for one iteration step, which is not acceptable for patient measurements. One reason for this relatively slow computational time is that the used frame grabber for the SH-sensor can only be operated in a 32 bit computer environment. Modern and fast computers are using a 64 bit operating system which would accelerate the process. However, this requires hardware changes such as replacing the SH sensor.

In addition, the exposure time currently required for the SH-sensor may be reduced. Currently the SH sensor samples the wavefront by a factor of $\sim$20 more accurate than it is possible to change the wavefront (which is determined by the number of elements of the deformable mirror). By reducing the number of lenslets more photons will contribute to each centroid which enables to reduce the exposure time of the SH-sensor and an improvement of the AO loop speed.

Another limiting factor of the current system is the rather slow AO-SLO imaging speed. The imaging speed is mainly determined by the frequency of the used resonant scanner which is operated at 4kHz. Other research groups use faster resonant scanner (e.g. 8kHz or 16kHz) which would improve the imaging speed by more than a factor of 2.

Regarding the post-processing software there is also room for improvement. Recent studies explored alternative techniques for motion correction [64, 65] that might be translated to the AO-SLO images acquired with this instrument. The techniques are based on B-spline elastic image registration, which might be easily adapted through the use of public domain software such as ImageJ.

Finally, it would be interesting to perform measurements in patients with known diseases, in order to attest for the device robustness and validate its clinical potential. Patient measurements require the implementation of a fixation target and the inclusion of an additional anterior segment monitor. This monitor will be essential to facilitate the alignment of the patient's eye in respect to the AO-SLO instrument.

These are just few steps that would certainly enrich this work and take it to a next level.

Bibliography

[1] Nicholas Wade and Michael Swanston. *Visual Perception: An Introduction*. Psychology Press, 2001.

[2] Al Lens, Sheila Coyne Nemeth, and Janice K Ledford. *Ocular anatomy and physiology*. Slack Incorporated, 2008.

[3] David R Williams. Imaging single cells in the living retina. *Vision research*, 51(13):1379–1396, 2011.

[4] F.C. Donders. Beiträge zur pathologischen anatomie des auges. *Archiv für Ophthalmologie*, 3(1):139–165, 1857. ISSN 0721-8494. doi: 10.1007/BF02720685. URL `http://dx.doi.org/10.1007/BF02720685`.

[5] Donald T Miller, David R Williams, G Michael Morris, and Junzhong Liang. Images of cone photoreceptors in the living human eye. *Vision research*, 36(8):1067–1079, 1996.

[6] Robert H Webb, George W Hughes, and O Pomerantzeff. Flying spot tv ophthalmoscope. *Applied Optics*, 19(17):2991–2997, 1980.

[7] Robert H Webb, George W Hughes, and Francois C Delori. Confocal scanning laser ophthalmoscope. *Applied Optics*, 26(8):1492–1499, 1987.

[8] Austin Roorda, Fernando Romero-Borja, William Donnelly III, Hope Queener, Thomas Hebert, Melanie Campbell, et al. Adaptive optics scanning laser ophthalmoscopy. *Optics Express*, 10(9):405–412, 2002.

[9] Alfredo Dubra, Yusufu Sulai, Jennifer L Norris, Robert F Cooper, Adam M Dubis, David R Williams, and Joseph Carroll. Noninvasive imaging of the human rod photoreceptor mosaic using a confocal adaptive optics scanning ophthalmoscope. *Biomedical optics express*, 2(7):1864–1876, 2011.

[10] Joseph Carroll, David B Kay, Drew Scoles, Alfredo Dubra, and Marco Lombardo. Adaptive optics retinal imaging-clinical opportunities and challenges. *Current eye research*, 38(7):709–721, 2013.

[11] Paul Vetschera. Implementation of a line-scanning laser ophthalmoscope into an adaptive optics system. Master's thesis, Techische Universität Wien, 2014.

[12] Gerold Christian Aschinger. Adaptive optics scanning laser ophthalmoscope. Master's thesis, Techische Universität Wien, 2012.

[13] Franz Felberer, Julia-Sophie Kroisamer, Christoph K Hitzenberger, and Michael Pircher. Lens based adaptive optics scanning laser ophthalmoscope. *Optics express*, 20(16):17297–17310, 2012.

[14] Toco YP Chui, Dean A VanNasdale, and Stephen A Burns. The use of forward scatter to improve retinal vascular imaging with an adaptive optics scanning laser ophthalmoscope. *Biomedical optics express*, 3(10): 2537–2549, 2012.

[15] Dale Purves, editor. *Neuroscience*. Sinauer Associates, 3rd edition, 2004.

[16] Wikimedia Commons. Three internal chambers of the eye, 2013. URL `http://commons.wikimedia.org/wiki/File:Three_Internal_chambers_of_the_Eye.png`.

[17] Herbert Gross, Wolfgang Singer, Michael Totzeck, Fritz Blechinger, and Bertram Achtner. *Handbook of Optical Systems*, volume 4: Survey of Optical Instruments. Wiley-VCH, 2008.

[18] Wikimedia Commons. Distribution of rods and cones along a line passing through the fovea and the blind spot of a human eye, 2013. URL `http://commons.wikimedia.org/wiki/File:Human_photoreceptor_distribution.svg`.

[19] Susana Martinez-Conde, Stephen L Macknik, Xoana G Troncoso, and David H Hubel. Microsaccades: a neurophysiological analysis. *Trends in neurosciences*, 32(9):463–475, 2009.

[20] Scott B Stevenson and Austin Roorda. Correcting for miniature eye movements in high resolution scanning laser ophthalmoscopy. In *Biomedical*

Optics 2005, pages 145–151. International Society for Optics and Photonics, 2005.

[21] Marco Lombardo and Giuseppe Lombardo. Wave aberration of human eyes and new descriptors of image optical quality and visual performance. *Journal of Cataract & Refractive Surgery*, 36(2):313–331, 2010.

[22] Michael Kaschke, Karl-Heinz Donnerhacke, and Michael Stefan Rill. Optics of the human eye. *Optical Devices in Ophthalmology and Optometry: Technology, Design Principles, and Clinical Applications*, pages 15–48, 2013.

[23] Orin Packer and David R Williams. Light, the retinal image, and photoreceptors. *The Science of Color, 2nd ed SK. Shevall, ed. Optical Society of America, Elsevier (Oxford, UK)*, pages 41–102, 2003.

[24] JASON Porter, H Queener, J Lin, KAREN Thorn, and ABDUL Awwal. Adaptive optics for vision science, 2006.

[25] Ann Elsner, Masahiro Miura, Stephen Burns, E Beausencourt, C Kunze, L Kelley, J Walker, G Wing, P Raskauskas, D Fletcher, et al. Multiply scattered light tomography and confocal imaging: detecting neovascularization in age-related macular degeneration. *Optics express*, 7(2):95–106, 2000.

[26] Betul Sahin, Barbara Lamory, Xavier Levecq, Fabrice Harms, and Chris Dainty. Adaptive optics with pupil tracking for high resolution retinal imaging. *Biomedical optics express*, 3(2):225–239, 2012.

[27] Larry N Thibos and Xin Hong. Clinical applications of the shack-hartmann aberrometer. *Optometry & Vision Science*, 76(12):817–825, 1999.

[28] Wikimedia Commons. Various closely related characterizations of an optical system exhibiting coma, a typical aberration that occurs off-axis., 2013. URL `http://commons.wikimedia.org/wiki/File:Definitions_PSF_OTF_MTF_PhTF.svg`.

[29] David Huang, Eric A Swanson, Charles P Lin, Joel S Schuman, William G Stinson, Warren Chang, Michael R Hee, Thomas Flotte, Kenton Gregory,

Carmen A Puliafito, et al. Optical coherence tomography. *Science*, 254 (5035):1178–1181, 1991.

[30] Michael Pircher, Erich Götzinger, Rainer Leitgeb, Harald Sattmann, Oliver Findl, and Christoph Hitzenberger. Imaging of polarization properties of human retina in vivo with phase resolved transversal ps-oct. *Optics Express*, 12(24):5940–5951, 2004.

[31] Michael Pircher, Wolfgang Geitzenauer, Christian Ahlers, Bernhard Baumann, Stephan Michels, Ursula Schmidt-Erfurth, Christoph K Hitzenberger, et al. Retinal pigment epithelium segmentation by polarization sensitive optical coherence tomography. *Optics express*, 16(21):16410–16422, 2008.

[32] Robert Tyson. *Principles of adaptive optics*. CRC Press, 3rd edition, 2011.

[33] Horace W Babcock. The possibility of compensating astronomical seeing. *Publications of the Astronomical Society of the Pacific*, pages 229–236, 1953.

[34] Joseph Carroll, Adam M Dubis, Pooja Godara, Alfredo Dubra, and Kimberly E Stepien. Clinical applications of retinal imaging with adaptive optics. 2011.

[35] Alfredo Dubra and Yusufu Sulai. Reflective afocal broadband adaptive optics scanning ophthalmoscope. *Biomedical optics express*, 2(6):1757–1768, 2011.

[36] Wikimedia Commons. Shack-hartmann sensor ray diagram, 2010. URL `http://commons.wikimedia.org/wiki/File:Shack_hartmann.jpg`.

[37] OPTOCRAFT: Optical Metrology. *SHSLab - Dokumentation*, 2011.

[38] Guang-ming Dai. *Wavefront optics for vision correction*, volume 179. SPIE press Bellingham, WA, 2008.

[39] William H Southwell. Wave-front estimation from wave-front slope measurements. *JOSA*, 70(8):998–1006, 1980.

[40] Alpao. *ALPAO CORE ENGINE rev 1.3*, 2012.

[41] Sophia I Panagopoulou and Daniel R Neal. Zernike vs. zonal matrix iterative wavefront reconstructor.

[42] John W Hardy. *Adaptive optics for astronomical telescopes*. Oxford University Press, 1998.

[43] Jin U Kang. *Fiber Optic Sensing and Imaging*. Springer, 2013.

[44] Francesco LaRocca, Al-Hafeez Dhalla, Michael P Kelly, Sina Farsiu, and Joseph A Izatt. Optimization of confocal scanning laser ophthalmoscope design. *Journal of biomedical optics*, 18(7):076015–076015, 2013.

[45] Austin Roorda. Applications of adaptive optics scanning laser ophthalmoscopy. *Optometry and vision science: official publication of the American Academy of Optometry*, 87(4):260, 2010.

[46] Yuhua Zhang and Austin Roorda. Evaluating the lateral resolution of the adaptive optics scanning laser ophthalmoscope. *Journal of biomedical optics*, 11(1):014002–014002, 2006.

[47] Shigeharu Kimura and Tony Wilson. Confocal scanning optical microscope using single-mode fiber for signal detection. *Applied optics*, 30(16): 2143–2150, 1991.

[48] Tim Dabbs and Monty Glass. Single-mode fibers used as confocal microscope pinholes. *Applied optics*, 31(6):705–706, 1992.

[49] Toco YP Chui, Michael Dubow, Alexander Pinhas, Nishit Shah, Alexander Gan, Rishard Weitz, Yusufu N Sulai, Alfredo Dubra, and Richard B Rosen. Comparison of adaptive optics scanning light ophthalmoscopic fluorescein angiography and offset pinhole imaging. *Biomedical optics express*, 5(4):1173–1189, 2014.

[50] Zhangyi Zhong, Hongxin Song, Toco Yuen Ping Chui, Benno L Petrig, and Stephen A Burns. Noninvasive measurements and analysis of blood velocity profiles in human retinal vessels. *Investigative ophthalmology & visual science*, 52(7):4151–4157, 2011.

[51] Stephen A Burns, Ann E Elsner, Toco Y Chui, Dean A VanNasdale, Christopher A Clark, Thomas J Gast, Victor E Malinovsky, and Anh-Danh T Phan. In vivo adaptive optics microvascular imaging in diabetic

patients without clinically severe diabetic retinopathy. *Biomedical optics express*, 5(3):961–974, 2014.

[52] R Daniel Ferguson, Zhangyi Zhong, Daniel X Hammer, Mircea Mujat, Ankit H Patel, Cong Deng, Weiyao Zou, and Stephen A Burns. Adaptive optics scanning laser ophthalmoscope with integrated wide-field retinal imaging and tracking. *JOSA A*, 27(11):A265–A277, 2010.

[53] Heidi Hofer, Pablo Artal, Ben Singer, Juan Luis Aragón, and David R Williams. Dynamics of the eye's wave aberration. *JOSA A*, 18(3):497–506, 2001.

[54] Hamamatsu Photonics. *APD Module C10508*, 2010.

[55] Laser Components. *APD Module LCSA/LCIA-Series*, 2012.

[56] Patrick Martinez. *A practical guide to CCD astronomy*, volume 8. Cambridge University Press, 1998.

[57] Claire Robertson and Steven C George. Theory and practical recommendations for autocorrelation-based image correlation spectroscopy. *Journal of biomedical optics*, 17(8):0808011–0808017, 2012.

[58] Geoff Dougherty. *Digital image processing for medical applications*. Cambridge University Press, 2009.

[59] Virendra N Mahajan. Strehl ratio for primary aberrations in terms of their aberration variance. *JOSA*, 73(6):860–861, 1983.

[60] Igor Kozak. Retinal imaging using adaptive optics technology. *Saudi Journal of Ophthalmology*, 28(2):117–122, 2014.

[61] Pooja Godara, Adam M Dubis, Austin Roorda, Jacque L Duncan, and Joseph Carroll. Adaptive optics retinal imaging: emerging clinical applications. *Optometry and vision science: official publication of the American Academy of Optometry*, 87(12):930, 2010.

[62] M Pircher, RJ Zawadzki, JW Evans, JS Werner, and CK Hitzenberger. Simultaneous imaging of human cone mosaic with adaptive optics enhanced scanning laser ophthalmoscopy and high-speed transversal scanning optical coherence tomography. *Optics letters*, 33(1):22–24, 2008.

[63] Franz Felberer, Julia-Sophie Kroisamer, Bernhard Baumann, Stefan Zotter, Ursula Schmidt-Erfurth, Christoph K Hitzenberger, and Michael Pircher. Adaptive optics slo/oct for 3d imaging of human photoreceptors in vivo. *Biomedical optics express*, 5(2):439–456, 2014.

[64] Akihito Uji, Sotaro Ooto, Masanori Hangai, Shigeta Arichika, and Nagahisa Yoshimura. Image quality improvement in adaptive optics scanning laser ophthalmoscopy assisted capillary visualization using b-spline-based elastic image registration. *PloS one*, 8(11):e80106, 2013.

[65] Johnny Tam, Joy A Martin, and Austin Roorda. Noninvasive visualization and analysis of parafoveal capillaries in humans. *Investigative ophthalmology & visual science*, 51(3):1691–1698, 2010.

Appendix A

Matlab Scripts

A.1 User Startup

This script initializes and defines the settings for all the elements comprising the adaptive optics loop: Shack-Hartmann wavefront sensor, wavefront reconstructor and deformable mirror.

```
% ALPAO CORE ENGINE example specialized class
% This code was written based on the example from ALPAO
% Last modification on June 2014
% Master Student: Ana Rita Carvalho

%% Deformable mirror
%wfs = aceoptocraft150SHS();
wfs = aceMY_WFSref();

% To change the mask change the size of the meshgrid

% MEDIUM MASK
% Use Command-matrix-22-04-2014-87zonalsmallpupil2.mat

% [X,Y] = meshgrid(linspace(-1, 1, 47));
% smask1 = (sqrt(X.^2+Y.^2)≤0.95);
% mask1 = zeros(66, 57);
% mask1(10:56,5:51) = smask1;

% SMALLER MASK
% Use Command-matrix-17-04-2014-87zonalsmallpupil.mat

% [X,Y] = meshgrid(linspace(-1, 1, 37));
```

```
% smask2 = (sqrt(X.^2+Y.^2)≤0.95);
% mask2 = zeros(66, 57);
% mask2(15:51,10:46) = smask2;

% DEFAULT MASK (FULL MASK)
%Use Command-matrix-08-04-2014-87zonal.mat

[X,Y] = meshgrid(linspace(-1, 1, 57));
smaskd = (sqrt(X.^2+Y.^2)≤0.95);
maskd = zeros(66, 57);
maskd(5:61, :) = smaskd;

%% Set mask

%mask1 = acewfsMASK(mask1);
% mask2 = acewfsMASK(mask2);
maskd = acewfsMASK(maskd);

wfs.set('sMask', maskd);

wfs.serialFile = '0111101064_840nm_1248x1082pixel.par';
acegui.wfs = wfs;

%% Deformable Mirror
disp('Build Deformable Mirror...');
dm=acewfcMAG_DM97('alpaoHSDM97-15-043');

% Set DM in online mode
%% LOOP
disp('Build Loop...');
loop = aceloopLOOP();
acegui.wfs = wfs;
acegui.dm = dm;
acegui.loop = loop;

% Attach devices to the loop object
loop.set('sWfc', dm);
loop.set('sWfs', wfs);
loop.Online
loop.closeLoopThread.sleepTime = 50;

% Define type of reconstruction
wfs.sReconstructor.type = 'zonal';
```

```
% Define error tolerance for the iterative reconstruction
wfs.sReconstructor.sZonalR.tol = 0.5;

% Initialize vector bias as zeros
b = zeros(97,1);

% Load previously saved bias vector
load bias.mat;
loop.sWfc.set('biasVector', bias);

%wfs.sCogEstimator.set('threshold', 0.1);
disp('userStartup finished');
%%

aceoptocraft150Mex(12, 'bSFAutoThreshold', 0);
% aceoptocraft150Mex(12, 'bSFAutoOffset', 0);
% aceoptocraft150Mex(12, 'bSFAutoSpotSize', 0);
% aceoptocraft150Mex(12, 'bSFDynamicAdaption', 1);
% aceoptocraft150Mex(12, 'bSFDynamicAdaptionOffset', 1);
```

A.2 Wavefront Sensor Class

This script overwrites the class defining the wavefront sensor.

```
% ALPAO CORE ENGINE example specialized class
% This code was written based on the example from ALPAO
% Last modification on March 2014
% Master Student: Ana Rita Carvalho

classdef aceMY_WFSref < aceoptocraft150SHS

%% Add new tip/tilt filtering properties
    properties
        filterTip = 0;
        filterTilt = 0;
        nImages = 1;
        myRef=zeros(1248,1082);

        gaincog = 2.5;
        minThresh=0.08;
```

```
    end

%% Define methods
    methods
        function obj = aceMY_WFSref()
            %% Constructor
        end % End Constructor

        function set(obj, varargin) %#ok<MANU>
            acecsSetScript;
        end



function [slopeX, slopeY] = GetSlope(obj)
%% Overload GetSlopes methods to add tipt/tilt filtering

  %% subract the reference
  im = obj.GetImage-obj.myRef;
  %% step made by the producer
  for k=1:obj.nImages
        %for k=1:10
     im = im+obj.GetImage-obj.myRef;
  end

 %% set image to zero if under minTresh
     im(im<obj.minThresh)=0;

 %% normalize image (step made by the producer)
     im=im/max(im(:));

 %% perform gain multiplication and removal of tip and tilt

     im = obj.gaincog*im; % This gain reduces the number of ...
        bad spots in the WFS


 % Acquire standard slopes
     [sx, sy] = GetSlope@aceoptocraft150SHS(obj, im);

            if obj.filterTip
                obj.slopeX = sx-mean(sx); % Removed Tip
            else
```

```
                obj.slopeX = sx;
            end

            if obj.filterTilt
                obj.slopeY = sy-mean(sy); % Removed Tilt
            else
                obj.slopeY = sy;
            end

            slopeX = obj.slopeX;
            slopeY = obj.slopeY;

        end
    end
end
```

A.3 Automatic Mask Adjustment

This script automatically computes a mask based on the illuminated area of the lenslet array in the wavefront sensor.

```
% This code was written by the Master student Ana Rita Carvalho
% Last modified: June 2014


function AdjustMask( wfs )
%computeAndApplyMask compute new mask value and apply it to ...
   wfs object

wfs.GetCog();

% See which one works and change this
try
   mask = computeMask( wfs.alight );  % Using Optocraft SH
catch %#ok<CTCH>
   mask = computeMask( wfs.sMask.alightMatrix ); % Using Alpao SH
end

wfs.Off; % Turn the wfs off to enable the change in the mask
wfs.sMask.sMatrix = mask; % Apply the new Mask
wfs.Online; % Turn on the wfs again
```

```
function mask = computeMask( alightMatrix )
%computeMask compute circular mask using alight matrix

mask = logical( size(alightMatrix) );

l = sum( alightMatrix ≠ 0, 1 );
c = sum( alightMatrix ≠ 0, 2 );

% Search pupil
lx = find(l, 1, 'first');
rx = find(l, 1, 'last');

uy = find(c, 1, 'first');
ly = find(c, 1, 'last');

if isempty(lx) || isempty(uy) || isempty(rx) || isempty(ly)
   return; % No pupil found
end

% Compute pupil parameters
width  = rx - lx +1; % Pupil width
height = ly - uy +1; % Pupil height

sx = size(alightMatrix,1); % Mask width
sy = size(alightMatrix,2); % Mask height
sz = min(width, height);   % Pupil diameter

sz = sz - 2; % /!\ Subtract one lens on each side of the pupil

bx = round((rx+lx-sz)/2)-1; % Pupil centre in X
by = round((uy+ly-sz)/2)-1; % Pupil centre in Y

% Mask (compute circle)

mask  = false(sx, sy);  % creates matrix of logical zeros .
[X,Y] = meshgrid(linspace(-1, 1, sz));
smask = sqrt(X.^2+Y.^2) ≤ 1.005;

mask( by+(1:sz), bx+(1:sz) ) = smask;
```